GEORG-AUGUST-UNIVERSITÄT
GÖTTINGEN

Quantifying topological transformation in lipid self-assemblies

Free Energy Calculations in Complex Systems

Dissertation for the award of the degree

Doctor rerum naturalium

of the Georg-August Universität Göttingen

within the doctoral program

Physics of Biological and Complex Systems

of the Georg-August-University School of Science (GAUSS)

submitted by

Laura Josefine Endter

born in Schmalkalden

Göttingen 2021

Thesis Committee

Dr. Herre Jelger Risselada
Institut für Theoretische Physik, Georg-August-Universität

Prof. Dr. Claudia Steinem
Institut für Organische und Biomolekulare Chemie, Georg-August-Universität Göttingen, Max-Planck-Institut für Dynamik und Selbstorganisation, Göttingen

Prof. Dr. Stefan Klumpp
Institut für Dynamik komplexer Systeme, Georg-August-Universität Göttingen

Members of the Examination Board

Dr. Herre Jelger Risselada (1st Referee)
Institut für Theoretische Physik, Georg-August-Universität

Prof. Dr. Claudia Steinem (2nd Referee)
Institut für Organische und Biomolekulare Chemie, Georg-August-Universität Göttingen, Max-Planck-Institut für Dynamik und Selbstorganisation, Göttingen

Further members of the Examination Board

Prof. Dr. Stefan Klumpp
Institut für Dynamik komplexer Systeme Georg-August-Universität Göttingen

Prof. Dr. Anette Zippelius
Institut für Theoretische Physik, Georg-August-Universität

Prof. Dr. Sarah Köster
Institut für Röntgenphysik, Georg-August-Universität Göttingen

Dr. Aljaz Godec
Max Planck Institut für Biophysikalische Chemie, Göttingen, Abteilung Theoretische und computergestützte Biophysik

Date of oral examination: 21.05.2021

List of Papers

Paper 1

Endter, L. J., Smirnova, Y. and Risselada, H. J. “Density Field Thermodynamic Integration (DFTI): A "Soft" Approach to Calculate the Free Energy of Surfactant Self-Assemblies”. In: *The Journal of Physical Chemistry B*. Vol. 124, no. 31 (2020), pp. 6775–6785. DOI: 10.1021/acs.jpcb.0c03982.

Author contribution: The author was responsible for the implementation and testing of the DFTI method including data analysis. All example calculations including the minimum free energy path calculations (string method) were performed by LJE. YS contributed the input structures for the DFTI calculations of the hemi-fusion stalk formation and guidance regarding the MFEP calculations. The manuscript was written by LJE and HJR and proofread and refined by YS.

Paper 2

Endter, L. J., and Risselada, H. J.. “Where are those lipid nano rings?”. In: *Journal of Colloid and Interface Science*. Vol. 587, April 2021, Pages , (2021), pp. 789–796. DOI: 10.1016/j.jcis.2020.11.038.

Author contribution: The author performed all presented free-energy calculations (DFTI, string method) and SANS-spectra predictions. Parts of the results presented were obtained during the authors master thesis (T-REM DryMartini model) or resumed (T-REM explicit solvent Martini). The manuscript was written in co-authorship of HJR and LJE.

Paper 3

Zoni, V., Nieto, V., Endter, L. J., Risselada, H. J., Monticelli, L., and Vanni, S.. “To Bud or Not to Bud: A Perspective on Molecular Simulations of Lipid Droplet Budding”. In: *Frontiers in molecular biosciences*. Vol. 6, (2019), pp. 124. DOI: 10.3389/fmolb.2019.00124.

Author contribution: This article was published in a special edition of Frontiers in molecular biosciences dedicated to the CECAM workshop **Multiscale Modeling from Macromolecules to Cell: Opportunities and Challenges of Biomolecular Simulations** (2019) and reflects opinions and discussions of the authors. The manuscript was mainly written by VZ and SV.

Paper 4

D'Agostino, M., Risselada, H. J., Endter, L. J., Comte-Miserez, V. and Mayer, A. "SNARE-mediated membrane fusion arrests at pore expansion to regulate the volume of an organelle". In: *The EMBO journal*. Vol. 37, no. 19 (2018), pp. e99193. DOI: 10.15252/embj.201899193.

Author contribution: The author parametrized the fluorescent dye 5-carboxy-2',7'-dichlorofluorescein which was used in the molecular dynamics simulations of HJR. The manuscript was written by MDA, HJR and AM.

Paper 5

(in preparation)
Mehner-Breitfeld, D., Ringel, M., Tichy, D. A., Hegermann, J., Endter, L. J., Stroh, K. S., Lünsdorf, H., Risselada, H. J., and Brüser, T. "Evidence for a functionally important membrane-thinning by linear TatA assemblies in *Escherichia coli*".

Author contribution: Supervision of DAT in colloboration with KSS during the preparation of his bachelor thesis. LJE and KSS were responsible for the conception of performed molecular dynamics simulations and data analysis protocols. The author further contributed by generating the used TatA-mutations using Modeller.

Contents

Chapter 1

Introduction

"Imagine that we had some way to look directly at the molecules in a living organism. ... Many of the questions puzzling the current cadre of scientists would be answered at a glance. But the nanoscale world of molecules is separated from our everyday world of the experience by a daunting million-fold difference in size, so the world of molecules is completely invisible."

Figure 1.1: Formation and budding of lipid droplets in the membrane of the endoplasmic reticulum. Illustration by David S. Goodsell (RCSB Protein Data Bank, see Ref. [1]).

These words from the preface of David S. Goodsells Book *The Machinery of Life* [2] sum up the challenge and likewise the motivation of everyone trying to understand biological processes and thus life itself [3]. In his colorful paintings, such as the one shown in Fig. 1.1, he depicts life at a cellular or sub-cellular level

revealing its beauty and complexity. The knowledge needed for these illustrations is based on experiments and models developed to overcome the difference in length and timescale that separates us from the molecular world.

The biological key players, amongst proteins and DNA, are lipids. Lipids are the main building block for membranes which compartmentalize organisms into cells and cells into cell organelles, e.g. the nucleus, the endoplasmic reticulum (ER) or lipid droplets (LDs, Fig. 1.1). This separation is driven by the amphiphilic nature of lipids, i.e. having a hydrophilic headgroup and a hydrophobic tail. The hydrophobic effect causes the lipids to spontaneously assemble into supra-molecular aggregates, such as micelles, vesicles or bilayers [4]. Sheet-like assemblies, i.e. monolayers and bilayers, are a durable yet flexible material, perfect for integration into dynamic processes. As membranes they serve as barriers while still allowing active and passive transport and energy transduction [5]. This is possible since individual lipids are not stationary, as in a crystal, but indeed very mobile. Their ability to diffuse laterally in the membrane is integral for accommodation and trafficking of proteins and enables the membrane to quickly adapt to topological changes.

With the recognition of membranes and their fluid nature as active players in cellular mechanisms, such as vesicle fusion [6] or formation of targeting sites due to curvature [7], the interest in a detailed understanding and quantification of these collective transformations has grown. Many techniques, *in vivo*, *in vitro* and *in silico*, have been devised to investigate these phenomena. While *in vivo* studies will naturally describe a process in its full complexity, *in vitro* experiments using model systems, such as giant unilamelar vesicles (GUV) or pore-spanning membranes (PSM) [8] enable researchers to single out important factors influencing a process. Modern techniques such as single-atom cryo electron microscopy provide the means to resolve structures of proteins in membranes in atomistic detail [9]. Even important fusion intermediates have been identified using fluorescence labelling of lipids in GUVs [6, 10]. Despite the former providing the possibility to capture an exact (down to ≈ 1.5 Å [11]) image of biologically relevant structures and the latter easily capturing the timescale of complex transformations in membranes, there remains a gap that computer-aided modelling seeks to fill.

Molecular dynamics (MD) simulations offer a glimpse at the *invisible* world described in the quote at the beginning. While continuum models based on the Helfrich elastic model [12], focus properties of lipid assemblies as a material at the mesoscale, particle-based simulations allow us to follow the dynamics of individual molecules in the system. With the technical advances in the last decades and broad access to computational resources, simulations have become a

widely used tool to visualize and uncover mechanistic information not available through experiment [13].

Most notably, free-energy methods have added substantial value to the field. With an abundance of techniques [14] they have provided the opportunity to quantify processes at the molecular level and thus, complement experiments and pave the way to mechanistic understanding. The free energy F contains information about the stability of a given configuration. Thus, comparison of the free energy makes it possible to determine whether a process happens spontaneously, i.e. the transition of the system to a more stable state. Unfortunately, the calculation of the free energy is at best challenging if not impossible for large systems, since it requires knowledge of all possible configurations, i.e. phase space. The stability of a state is directly linked to the number of microstates/configurations associated. The difference in free energy between two states can be determined without the knowledge of the *absolute* free energy by measuring the changes along the transition route. However, two distinct phases are often separated by barriers, i.e. configurations of low stability and thus low sampling probability. This often renders (sufficient) sampling of the transition impossible to achieve in simulations. For successful calculation of the free-energy difference it is thus indispensable to find ways to sample states along a path, physical or non-physical, connecting them. A common way to achieve this, is the usage of external potentials to *guide* the process, e.g. gradually changing the position of a particle or its interaction with other particles while monitoring the changes in the potential [15].

However, the fluid nature of membranes poses a challenge to find a suitable reaction coordinate, i.e. a parameter that describes the change along a transformation path. Topological changes often involve a large number of lipid molecules (*collective* transformation) that need to be considered. Furthermore, lipids of the same type are basically indistinguishable when exchanged, that is every microstate has a high degeneracy. In a simulation, however, the particles/molecules are labeled individually. Collective rearrangements require that the diffusive nature be retained, implying that the lipids need to be indistinguishable. Applying an external potential on the individual molecules compromises that condition. A permutation reduction, as used by Bubnis et al. [16] or using, e.g. local densities as a guiding parameter (Müller et al. [17–19]) offer mitigation.

Nevertheless, the application of these methods is still limited to only a few studies. However, with the increasing prevalence of computer simulations in life science, there is a demand for methods that are easy to use and applicable to a broad spectrum of systems.

The aim of this project was to develop and apply a versatile free-energy calculation

protocol to enable the estimation of free-energy differences between meta-stable states of lipid assemblies. Building on the work by Müller et al. [17–19] the method is meant to provide high accessibility in order to make this type of free energy methods more suitable for a broader usage in the community of bio-molecular modellers. Combining thermodynamic integration, one of the most established free-energy methods with a density-based external potential, offers the possibility to outline morphologies along a reversible path connecting two meta-stable states.

In addition, lipid droplets, as an example for membranes as active players in biological processes (see Fig. 1.1), are investigated with a focus on their emergence and the role of the related protein seipin.

This thesis is organized as follows. In the following, a very brief introduction into the underlying principles of the methods used in this thesis (Sec. 1.2 and 1.1) is given.

Chap. 2 represents the greatest share of this work: the implementation and testing of the so called density field thermodynamic integration (DFTI). The method was tested for three cases, breaking of a worm-like and a toroidal micelle and the formation of a hemifusion stalk (the results for the toroidal micelle can be found in the appendix of Chapter 3). Comparison with results obtained via another free-energy method, the so called string method [17, 20], demonstrates that the DFTI indeed could serve as a faster alternative, if knowledge about the exact physical pathway is not required.

In Chap. 3 a special case of lipid self-assembly is explored: the formation of nano-sized toroidal micelles from single-chain bola amphiphiles. This study plays with the idea of lipids as smart materials. Driven by curiosity and backed by free-energy calculations, we predict the existence of these structures that have not yet been observed experimentally.

Chap. 4 presents the results obtained, up to the current point, in modelling lipid droplet budding. Insights into the modelling process as well as a discussion of obstacles and limitations of the methods at hand are provided.

Each Chapter features an introduction to the respective topic and a thorough discussion of the presented results. Chapter 2 and 3, at the same time, present publications compiling results obtained during this work (see List of Papers for author contribution). The thesis is concluded by a summary and outlook in Chapter 5.

1.1 Molecular Simulations

With increasing computational power, simulation techniques have become a very resourceful tool in all fields for testing and verification of hypotheses. In soft matter sciences molecular dynamics (MD) helps to study thermodynamic properties and the dynamics of molecules.

MD is based on the principles of classical mechanics, namely Newton's second law of motion:

$$F = ma. \tag{1.1}$$

In MD, applying the Born-Oppenheimer approximation (i.e. separation of the electronic motion from the motion of the core), only the motion of the nuclei as rigid bodies is described. The particles thereby move in a conservative potential. This potential includes all interactions relevant to the system, meaning intra- (bonded) and intermolecular (non-bonded) interactions. Integration of Newton's law yields the evolution of the system in time. This classical description is essential to enable simulations on the timescale of nano- or microseconds. Quantum chemical approaches, despite being more detailed and theoretically more accurate, are not feasible for large molecules or systems nor is the additional information required for many questions posed in biophysics or material science.

In the following paragraphs the principles of molecular dynamics simulations relevant for this thesis are shortly described. For a more detailed description, textbooks such as Ref. [21] and Ref. [22], are referred to.

Numerical Integration Eq. 1.1 describes the force $\boldsymbol{F}_i = -\nabla_i V(\boldsymbol{r})$ exerted on each particle i in the system.

$$\boldsymbol{F}_i = -\nabla_i V(\boldsymbol{r}) = m_i \frac{d^2 \boldsymbol{r}_i(t)}{dt^2} = m_i \boldsymbol{a}_i. \tag{1.2}$$

The forces are calculated as the negative gradient of the potential $V(\mathbf{r})$ in which the particles move, where $\boldsymbol{r_i}(t)$ are the coordinates of particle i with mass m_i at a specific point in time and $\boldsymbol{r}$ the coordinates of all particles. The integration can be carried out by the leap-frog algorithm (Eq. 1.3 and 1.4) [23], which is the standard integrator for the Gromacs molecular dynamics software package [24–26].

$$\boldsymbol{r}(t + \Delta t) = \boldsymbol{r}(t) + \boldsymbol{v}\left(t + \frac{1}{2}\Delta t\right)\Delta t \tag{1.3}$$

$$\boldsymbol{v}\left(t+\frac{1}{2}\Delta t\right)=\boldsymbol{v}\left(t-\frac{1}{2}\Delta t\right)+\frac{\boldsymbol{F}_i(t)}{m_i}\Delta t \tag{1.4}$$

This simple and efficient algorithm evaluates positions $\boldsymbol{r}$ and velocities $\boldsymbol{v}$ at interleaving half-steps. Time reversibility of the leapfrog algorithm ensures energy conservation. The time for one full step depends on the fastest motion occurring in the system. Choosing a too large time step will not capture them correctly and lead to instabilities in the integration [27].

Force Field The force $\boldsymbol{F}$ (Eq. 1.2), is the negative gradient of the potential $V(\boldsymbol{r})$ of the system. This potential is comprised of all interactions in the system. The interactions can be separated in bonded and non-bonded interactions. While bonded interactions describe all the bonds that exist between particles forming molecules, the non-bonded interactions determine the relation of different particles to each other. A set of functions describing each part of the potential, or more often, the associated parameters of these functions is referred to as force field or model. The functional form as well as the respective parameters depend on the specific problem, but a common choice, also used in the GROMACS MD-implementation, is shown in Eq. 1.5.

$$\begin{aligned}
V(\boldsymbol{r}) = &\sum_{bonds}\frac{1}{2}k_b(b-b_0)^2 \\
&+\sum_{\text{angles}}\frac{1}{2}k_\theta(\cos\theta - cos\theta_0)^2 \\
&+\sum_{\text{dihedral}}k_\phi(1+\cos(n\phi-\phi_S)) \\
&+\sum_{\text{improper}}\frac{1}{2}k_\zeta(\zeta-\zeta_0)^2 \\
&+\sum_{\text{coulomb}}f\frac{q_iq_j}{\epsilon_r\boldsymbol{r}_{i,j}} \\
&+\sum_{\text{LJ}}4\epsilon_{i,j}\left(\left(\frac{\sigma_{i,j}}{\boldsymbol{r}_{i,j}}\right)^{12}-\left(\frac{\sigma_{i,j}}{\boldsymbol{r}_{i,j}}\right)^{6}\right)
\end{aligned} \tag{1.5}$$

Bonded interactions are treated as simple harmonic oscillators with force constants k and equilibrium bond lenghts b_0, angles θ_0 and out-of-plane angles ϕ_0. The non-bonded interactions are separated into electrostatic interactions of (partially) charged particles and the dispersion forces. Electrostatic interactions are described by Coulomb's law and dispersion by a 6-12-Lennard-Jones

Potential [28]. This potential mimics the attractive Van-der-Waals (VdW) forces between particles at a distance and the short-range Pauli repulsion at very short inter-particle distances. The parameters constituting a force field are often derived empirically by fitting to experimental or computed parameters, e.g. from quantum mechanical or *ab initio* calculations. Since the calculation of all possible pairwise interactions ($O(N^2)$) would take up a significant amount of the simulation time, it is necessary/common to focus on the interactions with highest relevance by applying cut-offs. Since both the Lennard-Jones and Coulomb Potential decay to zero for growing distance, the interactions of particles that are far apart have a minor impact and can be neglected/cut.

Coarse Graining The calculation of the forces acting on individual particles is what takes up most of the time in a simulation. In order to yield longer simulation time optimizations are necessary. One strategy to reduce the time spent for the calculation of forces is coarse graining (CG): by combining groups of atoms into larger particles, and thus omitting molecular details, the number of degrees of freedom is reduced and less interactions need to be calculated. Having larger particles, i.e. not considering the fast motion of individual atoms, also allows for the use of larger time steps without causing instabilities, yielding an additional speedup. These reduced models have a smoother energy landscape facilitating efficient sampling, because small barriers are easier and thus more likely to overcome. It is important to find a suitable model for the question asked. A coarser model may not be sufficient to study, for instance, a conformational change of a protein binding pocket upon reactant binding, but it can help to understand the motion of proteins on a membrane, which would not be feasible to simulate in all-atom detail.

The MARTINI model [30] is a coarse grained force field specifically designed for simulations of bio-membranes and related species, such as proteins and other small molecules. Being parametrized to mimic the phase behaviour of lipids, it is well suited to study the collective behaviour, i.e. aggregation and dynamic transformation, of lipid assemblies. Allowing a time step of up to 40 fs (compare all-atom ≈ 2 fs) it is possible to tackle phenomena at timescales far beyond the capabilities of more detailed models. Yet it provides enough chemical detail to even identify protein binding sites [31].

The general approach of the MARTINI model is mapping about four heavy atoms (i.e. carbon, oxygen, nitrogen, etc.) into particles of same size and mass (with exceptions for special cases, such as aromatic rings). These particles are assigned a type defining their nature, such as charged, hydrophilic/phobic, neutral. This building block approach allows for using one's *chemical intuition*, for easy modifications or creation of molecule parametrizations.

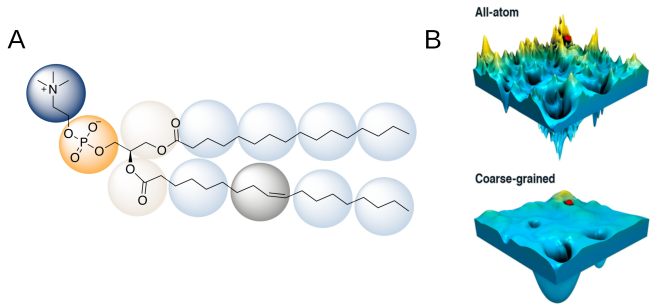

Figure 1.2: A) Example of the MARTINI mapping scheme applied to a POPC molecule (1-palmitoyl-2-oleoyl-sn-glycero-3-phosphocholine). B) Comparison of the energy landscape for an all-atom desciption vs. coarse grained. Smoothening of the energy landscape enables more efficient sampling (Figure adapted from Ref. [29]. The original source can be found here. For further permission please contact ACS.)

1.2 Free-Energy Calculations

When trying to understand our world we ask *why* something happens the way it does. This question is synonymous to the search for the driving forces powering processes. In biophysics, processes are governed by thermodynamics. A system will try to adopt a phase of lower free energy F. Differences in the free energy of different states of a system tell something about the spontaneity of a transition from one thermodynamic state to another and determines the direction. The occurrence of a process, however, may be hampered by energetic barriers, i.e energetically unfavorable configurations that need to be surpassed to get to a more stable state.

The free energy of a system can be understood as a thermodynamic equivalent of the potential energy in mechanics. It provides a measure of how much energy is stored in a thermodynamic state to do work on the system. The absolute free energy is given by

$$F = -\frac{1}{\beta} \ln Q \tag{1.6}$$

where β is the inverse temperature ($\frac{1}{k_B T}$) and Q is the partition function of the system.

The partition function of a thermodynamic state A is given by

$$Q_A = \frac{1}{h^{3N} N!} \int_{\Gamma_A} \exp(-\beta H(\boldsymbol{x}, \boldsymbol{p})) \mathrm{d}\boldsymbol{x} \mathrm{d}\boldsymbol{p} \tag{1.7}$$

Γ_A is the phase space accessible to state A. The relation to the total phase space Γ (meaning all possible configurations) is the probability p_A to find the system in state A.

The connection to the total partition function Q, containing information about all accessible states, is a challenging problem when trying to calculate this valuable quantity. Only for the simplest systems we can obtain an analytical function for Q and thus calculate the *absolute* free energy at all. However, for most systems, especially all realistic ones, the calculation of the integral over phase space is far beyond our capabilities. Hence, we need to find ways to retrieve the free energy by other, more accessible means.

In general the quantity containing the information we seek is not the absolute free energy but the relative free energy, i.e. the difference ΔF between two states.

$$\Delta F_{AB} = F_B - F_A = -\frac{1}{\beta} \ln \frac{p_B}{p_A} = -\frac{1}{\beta} \ln \frac{Q_B}{Q_A} \tag{1.8}$$

Free energy differences can in principle be evaluated from single trajectories of equilibrium simulations covering all possible states, as it is done in Zwanzig's approach (also known as Free Energy Perturbation) [32]. However, in practice this is difficult to realize. Most systems will not have a sufficient phase space overlap between two states, making sufficient sampling unattainable. Stable low energy states are often separated by energy barriers, i.e. states of very low probability, that will not be overcome in a feasible amount of time considering simulation time scales (though this can also be true for experiments).

A way to bypass lack in overlap is the introduction of intermediate states [33, 34]. These intermediate configurations building a path between two states do not necessarily have to correspond to any physical states. The transformation is often described by a coupling parameter λ, with $\lambda \equiv 0$ or $\lambda \equiv 1$ for the metastable physical states A and B, respectively, and adopting values $0 < \lambda < 1$ for intermediates. This principle is used, e.g. to determine binding or solvation free energies. Interactions of involved particles can successively be altered in their interactions shifting them from one particle type to another or from existence to non-existence. But also for less *alchemical* [35] transformations, such as conformational changes by backbone rotation in proteins or morphological changes in lipid assemblies, this principle can be used. Often external potentials are harnessed to drive the system over barriers by stabilizing unfavourable states (see Fig. 1.3). Commonly, the external biasing potential takes the form of a harmonic potential where the respective force constant penalizes deviations from a reference value for a chosen reaction coordinate.

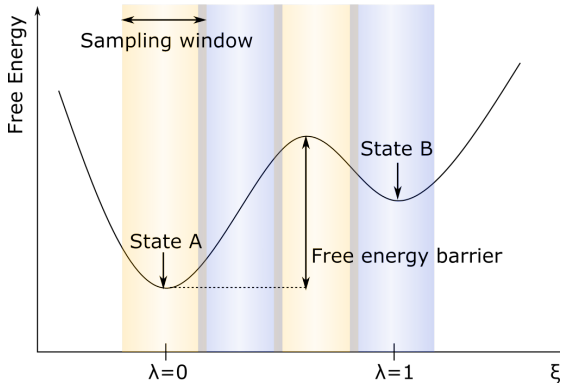

Figure 1.3: Windowed sampling. Biasing potentials (indicated by colored blocks) can be used to sample unstable states along a transformation path. (adapted from Ref. [36])

Many methods, such as the Bennett Acceptance Ratio (BAR) method, Multistate Bennett Acceptance Ratio (MBAR) or the Weighted Histogram Analysis Method (WHAM) [37], to calculate the free energy differences from the sampled states have been developed. For an in-depth review and overview of Free energy calculations and possible approaches, Refs. [22, 32, 37] are referred to.

Thermodynamic Integration Free-energy calculations are still an active field of research and new methods and applications arise with new technological advances and new use cases. Thermodynamic integration (TI) is a common way to estimate the free energy difference. As described above, a dependence on a coupling parameter λ can be introduced to the Hamiltonian H of a system linking two different states A and B. With the Hamiltonian, or mostly the potential energy term $V(\boldsymbol{q})$, being a function of λ, the free energy will also be such.

Instead of estimating the probabilities to adopt a certain state the derivative of the free energy (cf. Eq. 1.6) with respect to λ is calculated:

$$\frac{\mathrm{d}F}{\mathrm{d}\lambda} = -\beta^{-1}\frac{\mathrm{d}}{\mathrm{d}\lambda}\ln\int e^{-\beta V(\lambda,\boldsymbol{q})}\mathrm{d}\boldsymbol{q} = -\beta^{-1}\frac{\frac{\mathrm{d}}{\mathrm{d}\lambda}\int e^{-\beta V(\lambda,\boldsymbol{q})}\mathrm{d}\boldsymbol{q}}{Q} \tag{1.9}$$

This is equivalent to the canonical ensemble average of $\frac{\delta V}{\delta\lambda}$

$$\frac{\mathrm{d}F}{\mathrm{d}\lambda} = -\beta^{-1}\frac{-\beta\int\frac{\mathrm{d}V(\lambda,\boldsymbol{q})}{\mathrm{d}\lambda}e^{-\beta V(\lambda,\boldsymbol{q})}d\boldsymbol{q}}{Q} = \left\langle\frac{\delta V(\lambda,\boldsymbol{q})}{\delta\lambda}\right\rangle_{\lambda} \tag{1.10}$$

If the transition pathway is chosen properly, the drift in the free energies given by 1.6 can be calculated via numerical integration over all intermediate states λ_i,

$$\Delta F = \int_0^1 \left\langle \frac{\mathrm{d}V(\lambda_i, \boldsymbol{q})}{\mathrm{d}\lambda_i} \right\rangle_{\lambda_i} \mathrm{d}\lambda. \tag{1.11}$$

The integration can be performed using simple integration schemes like the trapezoidal or simpson's rule or cubic splines. Also here the the intermediate states do not have to have physical meaning. The only constraints are that $V(\lambda)$ be a continuous function and that the averages at the intermediate states be taken over a proper equilibrium ensemble. Therefore, sufficient sampling of the equilibrium distribution needs to be ensured. In section 2.2 a working definition of equilibrium used in our simulations can be found.

I

Chapter 2

Density Field Thermodynamic Integration (DFTI): A "Soft" Approach to Calculate the Free Energy of Surfactant Self-Assemblies

Laura Josefine Endter, Yuliya Smirnova, Herre Jelger Risselada

Published in *The Journal of Physical Chemistry B*, July 2020, volume 124, issue 31, pp. 6775–6785. DOI: 10.1021/acs.jpcb.0c03982.

Abstract

Thermodynamic integration is one of the most established methods to quantify excess free energies between different meta-stable states. Excess intermolecular interactions in surfactant assemblies are on the scale of the energy of thermal fluctuations. Therefore, these materials can be deformed and topologically altered via relatively small mechanical stresses. It is thus intuitive to design reaction paths and associated order parameters which exploit the 'soft' nature of these materials to mechanically rather than alchemically morph surfactant assemblies from state to state. Here, we propose a novel method coined 'Density Field Thermodynamic Integration' (DFTI) which adopts the universality and transferability of alchemical methods while simultaneously exploiting the soft excess interactions between surfactant molecules. DFTI is designed for a rapid quantification

of the free energy differences between different metastable structures in soft, fluid materials. The DFTI method uses an external field coupled to the local density to mechanically morph the system between meta-stable states of interest. Here, we explored the capability of the DFTI method to swiftly and accurately calculate free energy differences between states. To this aim, we studied two different coarse-grained lipidic surfactant systems: (i) a fusion stalk, and (ii) worm-like micelle. Our results illustrate that DFTI can provide an efficient, versatile and rather reliable method to calculate the free energy differences between surfactant assemblies.

Contents

2.1 Introduction

Surfactant assemblies are characterized by soft intermolecular interactions and can be deformed or topologically altered by thermal or mechanical stress of the magnitude of thermal fluctuations. In biology, the protein mediated remodeling of the lipid membrane is essential for many cellular processes [1] such as, for example, membrane fission [2], fusion [3, 4], formation of lipid droplets [5–7] or cell lysis [8, 9]. Quantifying the free-energy differences between end states of formed intermediates can provide valuable insights into the potential roles and mechanisms of cellular remodeling proteins. In particular, since free energies of lipidic reaction intermediates are typically eluded from direct experimental determination (e.g., the stalk structure in membrane fusion [10]). In material sciences, the rheological properties of worm-like micelle solutions under shear stresses relate to the micelle's likelihood to undergo scission and/or form branches [11–14]. Within these fields, the ability to theoretically predict the thermodynamic stability and likelihood of occurrence of different formed topologies via quantification of their relative free-energy difference would therefore aid to the rational design of novel synthetic surfactants.

Free-energy differences between states cannot be calculated directly because the free energy of a system is not simply a function of the phase space coordinates of the system, but rather a function of the Boltzmann-weighted integral over

phase space (the partition function). In particular, quantifying relative free-energy differences between different surfactant assemblies is challenging because of the highly diffusive nature of these materials [15–18]. Ideally, a free-energy calculation method is (i) accurate, (ii) computationally inexpensive, and (iii) applicable for different systems of interest (multi-purpose).

Thermodynamic integration is one of the most established methods for quantifying excess free energy between different (meta-stable) states. In thermodynamic integration, the free-energy difference ΔF is calculated by defining a thermodynamic path between the states and integrating over ensemble-averaged enthalpy changes $\left\langle \frac{\delta U(\lambda)}{\delta \lambda} \right\rangle$ along the path:

$$\Delta F_{0\to 1} = \int_0^1 \left\langle \frac{\delta U(\lambda)}{\delta \lambda} \right\rangle \mathrm{d}\lambda \tag{2.1}$$

The intermediate states connecting the end states do not necessarily have to be realistic or likely states. The only prerequisite of the path and its concomitant thermodynamic field, which is conjugated to the order parameter (density), is that the path is thermodynamically reversible, $\Delta F_{0\to 1} = -\Delta F_{1\to 0}$, and produces a smooth, integrable curve when plotting $\left\langle \frac{\delta U(\lambda)}{\delta \lambda} \right\rangle$ against the reaction coordinate λ, i.e., there is no hysteresis along the chosen path. Optimally, to enhance accuracy as well as computational (sampling) efficiency $\left\langle \frac{\delta U(\lambda)}{\delta \lambda} \right\rangle$ is minimized along the reaction coordinate λ since fluctuations in $\frac{\delta U(\lambda)}{\delta \lambda}$ are substantial. In other words, the thermodynamically reversible work performed to morph the system to the mutual reference state is optimally of a similar order of magnitude as the free energy difference between the two states of interests.

In 1984 Frenkel and Ladd proposed the "Einstein crystal method" to compute the free energy of solids [19]. The unique advantage of the Einstein crystal is that the N interaction sites in the system are converted to a set of N independent, non-interacting, restrained harmonic oscillators whose *absolute* free energy can be analytically derived. Variations on this universal approach have been successfully exploited in calculating the *relative* free energy differences in self-assembled, diffusive systems using soft density field based coarse-grained models [15, 20]. In more fine-grained molecular models, the ΔG associated with switching off Lennard-Jones based inter-molecular non-bonded interactions becomes large when studying surfactant assemblies of relevant sizes of hundreds of surfactant molecules or more [21–23]. As a consequence, the estimation of the free energy vastly becomes inaccurate with increasing system size because the free energy difference of interest between the two end states is now constituted by the difference between two extremely large numbers.

It is seemingly intuitive to think of a 'softer' alchemical scheme which avoids completely switching off the non-bonded interactions. For example, an alternative pathway would be to switch off bonded interaction and morph both end states into a mutual Lennard-Jones fluid or gas. However, switching off bonded interactions within surfactant molecules will (i) result in fast divergent values in $\left\langle \frac{\delta U(\lambda)}{\delta \lambda} \right\rangle$ because of sudden free diffusion, and (ii) will lead to heterogeneous fluid behavior because of the neighbor exclusion criteria implemented in most molecular force-fields (previously bonded interaction pairs are excluded from Lennard-Jones interactions).

Intermolecular interactions in soft materials are on the scale of the energy of thermal fluctuations. Therefore, these materials can be deformed and topologically altered via relatively small mechanical stresses. It is thus intuitive to design reaction paths and associated order parameters which exploit the 'soft' nature of these materials by *mechanically* rather than *alchemically* morphing the system between the two end states, ie. finding a preferably universal description of topological changes. Different pioneering mechanical reaction paths have been proposed for self-assembled systems to calculate the free energy differences between membrane fusion intermediates [15, 24–26], the fluid- to gel phase transition in lipid membranes [27], the end cap free energies of worm-like micelles [28], or membrane pore formation [29–32]. These reaction coordinates, however, were tailored to study a particular system (or mechanism) of interest – different tools for different jobs. In contrast, alchemical methods like the Einstein Crystal method are universal and transferable, but are in turn not practical for large diffusive Lennard-Jones systems.

Here, we propose a novel method coined "Density Field Thermodynamic Integration (DFTI)" which adopts the universality and transferability of the Einstein Crystal method while simultaneously exploiting the soft excess interactions between surfactant molecules. The DFTI method uses an external field based on the local density [10, 16, 33] to mechanically morph the system between meta-stable states of interest. DFTI is designed for a rapid quantification of the free-energy differences between different metastable structures in soft materials. In this work, we will explore the capability of the DFTI method to swiftly and accurately calculate free-energy differences between states. With this aim, we will study two different coarse-grained lipidic surfactant systems: (i) A fusion stalk, (ii) a worm-like micelle.

2.2 Methods

2.2.1 Density Field Description

Structural transformations in surfactant self-assemblies are collective and involve a large amount of highly diffusive molecules. Local densities provide an effective high dimensional reaction coordinate to delineate complex self-assembled structures, because density is (i) indiscriminate for the individual labels which molecular species carry within molecular simulations, but (ii) does discriminate between subtle differences in adopted structure. The local densities of a chosen group of atoms or molecules are defined on a discrete three dimensional collocation lattice spanning the simulation box. Particles contribute to the lattice points according to a weighting function. Here, we used the density of the hydrophobic lipid tails together with a linear assignment function $W(\mathbf{r}_i, \mathbf{c})$, where $\mathbf{r}_i$ are coordinates of particle i and $\mathbf{c}$ denotes a position on the collocation grid. The instantaneous number density per grid point, $\hat{m}(\mathbf{c})$, is determined by calculating the contribution to the nearest grid points forming a grid cell with volume ΔL^3 by integration over the system volume V.

$$\hat{m}(\mathbf{c}) = \int_V \frac{\mathrm{d}r}{\Delta L^3} W(\mathbf{r}, \mathbf{c}) \hat{m}(\mathbf{r}) = \frac{1}{\Delta L^3} \sum_i W(\mathbf{r}_i, \mathbf{c}) \tag{2.2}$$

where $\hat{m}(\mathbf{r}) = \sum_i \delta(\mathbf{r}_i - \mathbf{r})$ and the summation is over all particles of interest, for a more detailed description see [33].

In a simulation the density of a configuration is used as an order parameter for the morphology under investigation. Changes in the configuration are traced locally at each grid point and can be used to guide the simulation. The difference between reference and instantaneous local densities are used to calculate restoring forces due to a harmonic potential. The forces are redistributed to each particle according to the weighting function. The contribution of this external potential, V_{up}, is added to the system's Hamiltonian:

$$\begin{aligned} \frac{H_{\text{umbrella}}(\{\mathbf{r}\}, m(\mathbf{r}))}{k_{\mathrm{B}}T} &= \frac{H(\{\mathbf{r}\})}{k_{\mathrm{B}}T} + V_{\text{up}} \\ V_{up} &= \frac{k}{2} \int_V \mathrm{d}^3\mathbf{r} [m(\mathbf{r}) - \hat{m}(\mathbf{r}, \{\mathbf{r}\})]^2, \end{aligned} \tag{2.3}$$

where $m(\mathbf{r})$ are the local reference densities computed from averaging over the coordinates of a reference structure and $\hat{m}(\mathbf{r}, \{\mathbf{r}\})$ are the instantaneous local densities calculated from the coordinates $\{\mathbf{r}\}$ of the particles configurations. The factor k denotes the force constant of the harmonic potential. The choice of the

density as the order parameter allows to account for the indistinguishability of diffusing lipids, while restraining the overall morphology. Finally, it is important to note that simulations were performed in the *NVT* ensemble to ensure a conserved box size and thus allow the direct comparison (mapping) of the density profiles across all morphologies. Simulation within the *NPT* ensemble would require an adaptive density grid which is currently not implemented. Such simulations would require calculation of pressure which is not trivial since usual way to calculate virial is not applicable in lattice (or grid) systems. The free energy contribution associated with translation to the *NPT* ensemble can be alternatively obtained from the corresponding ($P\Delta V$) term when switching ensemble. In our simulations we equilibrated one of the end states in the *NPT* ensemble before switching to *NVT* and thus such a contribution is small (in the range of $k_\mathrm{B}T$) .

2.2.2 Thermodynamic Integration

To determine the free-energy difference $\Delta F_{a,b}$ between two (meta-)stable states, a thermodynamic cycle can be constructed which avoids first order transitions and allows a reversible transformation from one state to another.

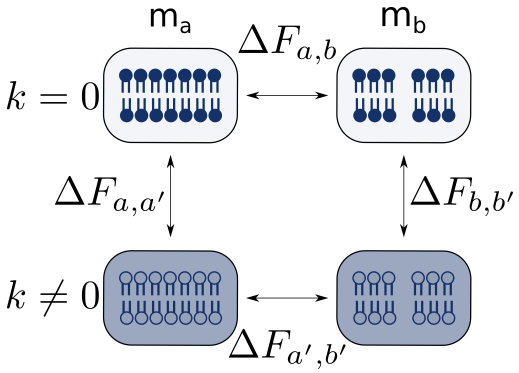

Figure 2.1: Thermodynamic cycle connecting two reference states a and b with reference densities m_a and m_b via states a' and b' where the morphologies are restrained by an umbrella potential V_up.

All states along the chosen path can be expressed by a combination of the end states which are described by their individual Hamiltonian. Here we use the added umbrella potential V_up to guide the transformation by introducing a dependence of the densities $m(\mathbf{r})$ and magnitude k on a coupling parameter λ.

$$\begin{aligned} m(\mathbf{r},\lambda) &= f(\lambda)m_b(\mathbf{r}) + (1-f(\lambda))m_a(\mathbf{r}) \\ k(\lambda) &= f(\lambda)k_b + (1-f(\lambda))k_a, \end{aligned} \tag{2.4}$$

where $f(\lambda)$ determines the functional form of this coupling. In the most simple case this corresponds to a linear coupling ($f(\lambda) = \lambda$). The free-energy difference is yielded by integration over the ensemble average of the changes in the potential

$$V_{\mathrm{up}}(\lambda) = \frac{k(\lambda)}{2}\int_V \mathrm{d}^3\mathbf{r}[m(\mathbf{r},\lambda) - \hat{m}(\mathbf{r},\{\mathbf{r}\})]^2 \tag{2.5}$$

with respect to a coupling parameter λ.

$$\Delta F_{a\to b} = \int_0^1 \left\langle \frac{\delta V_{\mathrm{up}}(\lambda)}{\delta\lambda} \right\rangle_\lambda \mathrm{d}\lambda \tag{2.6}$$

with

$$\begin{aligned} \frac{\delta V_{\mathrm{up}}(\lambda)}{\delta\lambda} =& \frac{k'(\lambda)}{2}\int_V \mathrm{d}^3\mathbf{r}[m(\mathbf{r},\lambda) - \hat{m}(\mathbf{r},\{\mathbf{r}\})]^2 \\ &+ k(\lambda)\int_V \mathrm{d}^3\mathbf{r}[m(\mathbf{r},\lambda) - \hat{m}(\mathbf{r},\{\mathbf{r}\})]\frac{\delta m(\mathbf{r},\lambda)}{\delta\lambda} \end{aligned} \tag{2.7}$$

The DFTI uses the discretized density field as an order parameter to construct an integrable but unphysical transition path. This is performed in a set of simulations (windows) where every individual window is subject to a reference state that is defined by a density field $m(\mathbf{r},\lambda)$ and the force constant $k(\lambda)$.

The thermodynamic cycle used in this work consists of three separate calculation steps. The free energy difference of interest – morphing between two structures in the absence of an umbrella field – is obtained by completion of the full thermodynamic cycle (adding and subtracting of the three obtained free energy contributions). When calculating the free energy contribution of the umbrella field itself, it is important to emphasize that $\lambda = 0$ defines the biased state where the the umbrella field is coupled to force constant $k_{\lambda=0} > 0$, whereas $\lambda = 1$ defines the unbiased state ($k_{\lambda=1} = 0$), i.e. the absence of the umbrella field. This is an arbitrary choice due to the reversibility of the process.

To calculate the free energy *gain* associated with 'releasing' each end state toward its physical state, the external potential is switched off ($k_{\lambda=1} = 0$) according to the coupling function $f(\lambda)$ over a set of simulation windows where the reference density field $m(\mathbf{r},\lambda) = m_a$ is kept constant. The gradual decrease of the external potential eventually enables free translation/rotation as well as large scale thermal fluctuations of the structure. In the second part, the morphology is transformed from the reference state m_a to the reference state m_b at a constant

field strength. The reference density profiles of the intermediate states do not have any physical meaning and are constructed according to the Eq. 2.4. For the complete thermodynamic cycle a simulation similar to the first part is performed using the morphologies of the meta-stable target state b. Initial reference densities of the end states are obtained as averages of the densities over the course of 200 ns simulations in the external field using an instantaneous snapshot density of the equilibrated structure as reference.

2.2.3 Minimum free-energy path calculation

As validation of our results we applied the improved string method by Weinan et al. [34] to our systems. This method has been successfully used by Smirnova et al. [10] to calculate the free energy barriers of inter-membrane stalk formation. A detailed description can be found in Ref. [16].

Analogous to our thermodynamic integration scheme, an external field acting on the density description of a system is used to describe both the end states and the intermediate structures (windows). In contrast to TI methods, however, the string method allows for the reconstruction of a physical path, i.e. the path of the minimum free energy (MFEP), between the two end-states. This path represents the most likely reaction pathway for the transition between the reference states. This is achieved by an iterative two step procedure. First, the free energy of the morphologies along the path (string) are minimized due to the gradient of the free energy in density space, which is described by the local chemical potential

$$\mu_{\mathrm{up}}(\mathbf{r}) = \frac{\delta F_{up}(m(\mathbf{r}))}{\delta m(\mathbf{r})} = k\, k_{\mathrm{B}} T [m(\mathbf{r}) - \langle \hat{m}(\mathbf{r}, \{\mathbf{r}\})\rangle] \tag{2.8}$$

The chemical potential is computed by short restrained simulations of all configurations along the string using the umbrella field described above. μ results from the difference of the reference density field and the average density distribution during the simulation. The reference densities of the successive iteration are re-evaluated by

$$m(\mathbf{c})_n = m(\mathbf{c})_{n-1} - \frac{\mu(\mathbf{c})}{k_{\mathrm{B}} T}\epsilon, \tag{2.9}$$

where ϵ is a constant defining the "speed" of this evolution, $m(\mathbf{c})$ and $\mu(\mathbf{c})$ are the local density and chemical potential at a given grid point $\mathbf{c}$. This leads to a minimization of the free energy of the system, which effectively means a quenching of fluctuations around the meta-stable state.

In a second step the string is reparametrized such that all morphologies are positioned equidistantly along the path. This is done using cubic splines.

The free-energy differences along the MFEP can be obtained by integration over the chemical potential along the path, given by the contour parameter s.

$$\begin{aligned} \Delta F(s) &= \int_0^s \mathrm{d}s' \frac{\mathrm{d}F}{\mathrm{d}s'}, \\ \frac{\mathrm{d}F}{\mathrm{d}s} &= \int \mathrm{d}^3\mathbf{r} \frac{\delta F[m_s]}{\delta m_s} \frac{\mathrm{d}m_s}{\mathrm{d}s} \\ &= \int \mathrm{d}^3\mathbf{r} \mu_s(\mathbf{r}) \frac{\mathrm{d}m_s(\mathbf{r})}{\mathrm{d}s} \end{aligned} \tag{2.10}$$

This integration is a volumetric, multidimensional equivalent of integrating the force along the arclength to obtain the performed equilibrium work.

2.2.4 Error analysis

The protocol of Schiferl and Wallace [35] was used to ensure correct sampling (sampling from an equilibrium distribution) and to calculate the corresponding errors for the ensemble averages. A system is considered to be in equilibrium with respect to an observable X if mean and variance of the timeseries $X(t)$ are independent of time. The data set is split in n bins and individual bins were tested for normality using the Shapiro-Wilk shape test. Averages X_k and variances s_k of the bins were tested for trends using the Mann-Kendall Trend test. The ensemble average was then calculated as the mean of all X_k. Errors are provided as standard deviation s calculated from the sample variance $s^2 = \frac{1}{n-1}\sum_{k=1}^{n}(X_k - \bar{X})^2$. The free energy differences were obtained by integration of the obtained curve using Simpson's rule. Errors were propagated accordingly.

2.2.5 Simulations setup

All simulations were performed using the coarse grained Martini force field (version 2.2) and the Gromacs molecular dynamics simulation suite. The external density umbrella potential and the calculation of the potential derivative with respect to the coupling parameter λ were implemented in Gromacs version 4.6.4. All simulations were performed in the *NVT* ensemble which ensures a conserved box size and thus allows the comparison (mapping) of the density profiles across all morphologies. The box size was determined from an equilibrium simulation at a pressure of 1 bar within the *NPT* ensemble of one of the end states. The velocity re-scaling scheme was used to couple the temperature in the simulations

to a constant-temperature bath [36]. The cut-off radius for coulomb and Van-der-Waals interactions and the neighborlist cut-off were set to 1.2 nm in compliance with the recommended parameters for the used Martini force field (version 2.2).

Fusion stalk The simulation contained two lipid bilayers each formed by 128 POPC (1-palmitoyl-2-oleoyl-sn-glycero-3-phosphocholine) molecules separated by a layer of 220 water beads corresponding to an inter-membrane distance of 1.2 nm. All simulations were performed at 300 K.

The thermodynamic cycle as described above proceeds in two steps. First, the strength of the external field is switched on for both of the end states: $\lambda = 0$ corresponds to the restrained morphology with a field strength constant of k. $\lambda = 1$ accordingly corresponds to the free simulation with no external field acting ($k = 0$). The values for $k\Delta L^3$ chosen in Gromacs units were 20, 50, 100 and 200 $\mathrm{kJmol^{-1}nm^3}$. Second, the switched-on external field, which restrains the system to a preset local density, is exploited to morph between the two end states via superposition of the reference densities of both end states. State **a** (bilayers without stalk) is set at $\lambda = 0$ and state **b** (bilayers connected by hemifusion stalk) at $\lambda = 1$. For this superpostition a linear ($f(\lambda) = \lambda$) coupling scheme was used (see Eq. 2.4).

For each step of the thermodynamic cycle the spacing of λ was chosen as 0.01, which corresponds to 101 intermediate states. All morphologies along the reaction coordinate were equilibrated in the corresponding external field for 4 ns followed by a 1.2 µs simulation. The initial structures of the end states were obtained from Ref. [10].

Worm-like micelle. The worm-like micelle (WM) is formed from 100 coarse grained dotriacontane-1,32-diyl-bis[2-(trimethylammonio)ethylphosphate] (PC-32-PC) lipids and solvated in water in a 9x9x13 nm simulation box. The simulation temperature was set to 350 K, for which the PC-32-PC is expected to form small micellar aggregates.

The free-energy difference between the state of the bilayers and the metastable hemifusion stalk connecting the two sheets is calculated using the same approach as for the bola micelle using a linear ($f(\lambda) = \lambda$) as well as a quadratic ($f(\lambda) = (1 - \lambda)^2$) coupling scheme.

The transformation was split in 51 consecutive simulation windows for each part along the scission reaction coordinate using a linear coupling scheme ($f(\lambda) = \lambda$). Each window was adapted to its corresponding umbrella field for 400 ps followed by a 400 ns production run. For the field strengths of $k\Delta L^3 = 50, 200\,\mathrm{kJmol^{-1}nm^3}$ a simulation time of 1.2 µs was used. The continues worm-like micelle was

constructed by spontaneous aggregation within the *NPT* ensemble. The broken worm-like micelle was constructed by exerting tension on the obtained continues worm-like micelle until rupture occurred. The size of the box was subsequently adopted such that the two free ends of the worm-like micelle were brought in close apposition. The corresponding box dimensions were imposed on the continues worm-like micelle to conserve volume between both end states. The continues micelle is therefore under a small excess tension/force of about $1\,k_\mathrm{B}T\mathrm{nm}^{-1}$ to enable relaxation of excess length when the two free end caps are formed. This is not expected to significantly ($< 1\,k_\mathrm{B}T$) affect the free energy difference between the end states.

Endpoint Minimization All simulations were performed under similar conditions as described above. Only short simulations of 50 ns are performed for each iteration. Reference densities were updated using a step width $\epsilon = 0.01$ according to Eq. 2.9. Linear coupling was used for the thermodynamic integration part. Thermodynamic integration was carried out at various force constants as test for consistency of the obtained results.

2.3 Results and Discussion

2.3.1 Formation of a hemifusion stalk

In this work we present and compare our results of the free-energy calculation performed for the systems described in the method section. As a first example, we studied the formation of a hemifusion stalk formed between two apposed membranes (Fig. 2.2).

Smirnova et al. [10] recently used the string method to study the dependence of the barrier in this reaction pathway on the inter-membrane distance. It was demonstrated that the here-used hydrophobic density based reaction coordinate enables a fully thermodynamically reversible pathway, as being evident from committer analysis of the resolved free energy barrier (hysteresis was absent). Moverover, the non-distinctive, soft and coarse nature of this restraining field still enables free diffusion of molecules over the density grid, quite in contrast to the Einstein crystal method which localizes individual atoms to a crystal lattice [22]. In this example, we used a linear coupling scheme and field strengths of $k\Delta L^3 = 20, 50, 100$ and $200\,\mathrm{kJmol}^{-1}\mathrm{nm}^3$ to estimate the free-energy difference between (a) two free apposed membranes, (b) a hemifusion stalk connecting them. Fig. 2.3 shows all individual steps of the thermodynamic integration. It is evident that the calculation of the first step within the thermodynamic cycle, i.e. switching off the external density field, yields a well-behaved curve in case of

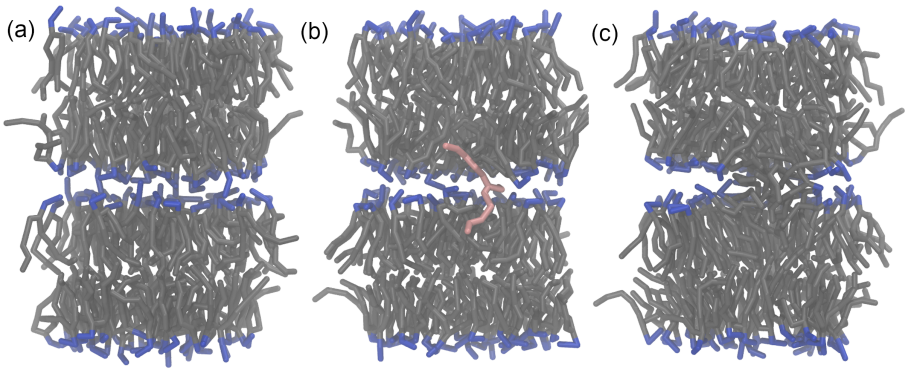

Figure 2.2: Snapshots of the DFTI for the formation of a hemifusion stalk between two bilayers. (a) start configuration A: two bilayers separated by an inter-membrane spacing of 1.2 nm or 220 water beads, (b) intermediate state (morphology 50/101) created by linear coupling. (c) start configuration B: two bilayers connected by a hemifusion stalk.

the two bilayers without a stalk. In contrast, for the target morphology, i.e. two bilayers connected by stalk, one can see a diverging behaviour when switching off the external field. This is explained by the sudden free lateral diffusion of the stalk structure when the field vanishes: An entropic effect. This entropic effect can be intuitively explained from a minimalistic model of a single particle in a box whose position is restrained by a vanishing umbrella potential (see Sec. 2.A.4). Nevertheless, a good estimate of the free-energy difference can be obtained by linear extrapolation of the last values close to $\lambda = 1$ (no external field).

The second step in the thermodynamic cycle involves morphing between the two free apposed membranes and a formed hemifusion stalk. For weak external fields ($k\Delta L^3 < 20\,\mathrm{kJmol^{-1}nm^3}$), instabilities occur for some λ values whose corresponding morphologies resemble the state of the physical transition barrier (a single or few lipids which bridge the two membranes [10]), because of barrier crossing against the external potential. This indicates that the external field is unable to sufficiently control the system close to the physical transition barrier. Such an observed instability implies that certain phase-space regions in that particular window are not easily thermally accessible and which challenges complete sampling of its biased equilibrium ensemble. These instabilities are prevented by increasing the strength of the external field. However, large force constants suppress the diffusion of individual lipids, result in 'freezing' of the overall structure, and therefore yield a slower sampling [33]. The reduced sampling at high k values especially affects the region near the physical transition

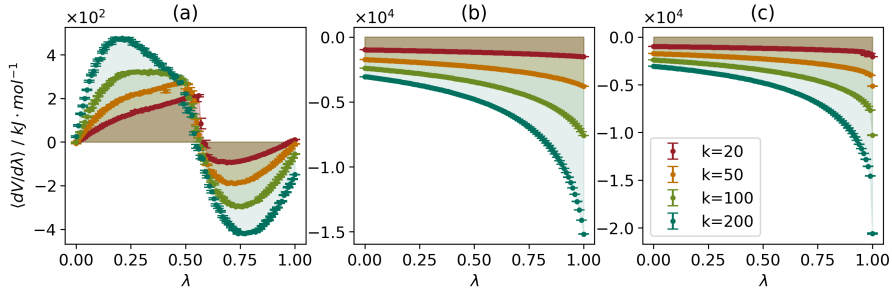

Figure 2.3: The free energy of stalk formation between two membranes as calculated via DFTI for different force constants of the density field. (a) Morphing the system between the two end states: A double membrane system without a stalk ($\lambda = 0$) and with a stalk ($\lambda = 1$), (b) Switching off the restraining field for two unconnected bilayers (c) As in b but for bilayers where a stalk is present. Note the diverging behavior at $\lambda = 1$ which is because of free diffusion of the center of mass of the stalk.

state ($\lambda = 0.5$) which features a single lipid connecting two membranes (see Fig. 2.2). The choice of parameters such as the field strength of the discretization of density is a matter of balance and demands good knowledge of the systems properties and particularities. The physical transition state of the here-studied example systems are all of a single molecular nature, i.e. a single or few lipids connecting the two apposed leaflets/micelles. Therefore, the discretization of the density field must be sufficiently fine to enforce the obedience of the structure towards the imposed local reference densities. A finer discretization of the density field would allow for the usage of smaller force constants k (since the total number of restraints on the system increases).

Table 2.1 summarizes the estimated free energy contributions for all of the different steps within the thermodynamic cycle. The grey colored region Table 2.1, illustrates the repetition of the exact same procedure but with the two end states being defined by a slightly different reference density (coined '# up 30'). In this example, the reference density '#up 30' represent a more minimized density field. This subject will be discussed in detail in the final section of this manuscript.

To this end, the outcome of the full thermodynamic cycle is presented in Table 2.1, column E. Notably, the full thermodynamic cycle is (and must be) invariant of (i) the choice of the reference density of the two end states, and (ii) the choice of field strength k. However, the individual values obtained for the different steps within the cycle are not invariant of these choices. For example, the free-energy gain due to switching off the field increases with increasing field strength k.

Table 2.1: Results of the DFTI calculations for the formation of a stalk for two bilayers at a distance of 1.2 nm for various force constants k. (A) Switching off the restraining field for two unconnected bilayers. (B) Switching off the restraining field but for two bilayers with a stalk. (C) Morphing from two unconnected bilayers to two bilayers with stalk. (D) As in C but now calculated from the chemical potential along reaction coordinate. (E) Free energy difference calculated along the full thermodynamic cycle. The grey colored region in Table 2.1, illustrates the repetition of the same procedure but with the two end states being defined by a slightly different reference density (coined '#up 30').

#up	$k\Delta L^3$ [kJmol^{-1}nm^3]	A [k_BT]	B [k_BT]	C [k_BT]	D [k_BT]	E [k_BT]
0	20	-476.81 ±0.15	-486.49 ±1.52	20.66±1.60	20.6	10.98±2.21
	50	-967.48 ±0.31	-975.20 ±1.22	20.84±1.23	20.9	13.12±1.75
	100	-1539.15 ±0.45	-1546.88±2.92	21.10±1.54	21.1	13.37±3.33
	200	-2295.40 ±0.70	-2305.84±4.43	24.57±1.62	24.5	14.13±4.76
30	20	-476.73 ±0.14	-483.60 ±1.18	19.58±1.35	19.6	12.71±1.79
	50	-968.29 ±0.25	-973.51 ±0.64	19.41±1.54	19.5	14.20±1.68
	100	-1540.68 ±0.32	-1545.15±0.77	19.39±1.56	19.5	14.92±1.76
	200	-2297.33 ±0.50	-2302.34±1.16	19.58±1.87	19.9	14.57±2.25

Finally, the free-energy differences of the morphing step can be alternatively calculated from direct integration over the local chemical potential along the path rather than integrating over $\langle \frac{dV_{up}}{d\lambda} \rangle$ (see Eq. 2.8). Generally, the values obtained via integration over the chemical potential are in good correspondence with the values obtained by thermodynamic integration (see Table 2.1, column D) as well as the string method [10]. In this example, all obtained values are within the range of 10-15 k_BT. Experimental quantification of the corresponding value of the stalks free energy remains ambiguous and its actual value has been debated for decades [37].

2.3.2 Endcap Energy of a Wormlike Micelle

As a second example, we studied a wormlike micelle (WM) formed by a coarse-grained model of the lipidic surfactant PC-32-PC. These type of surfactants exhibit a complex temperature induced phase behaviour and are thus an interesting candidate for detailed study of the underlying free-energy landscape [38]. Here, we investigate the scission of a continuous wormlike micelle as shown in Fig. 2.4. The free-energy cost of this transformation corresponds to the free-energy cost associated with forming the two free endcaps of the broken micelle.

Fig. 2.5b shows the obtained averages $\langle \frac{dV_{up}}{d\lambda} \rangle$ for the first step of the thermodynamic cycle (i.e., switching off the density field) for the continuous wormlike micelle. In a very weak or non existing external field ($\lambda = 1$) the structure is

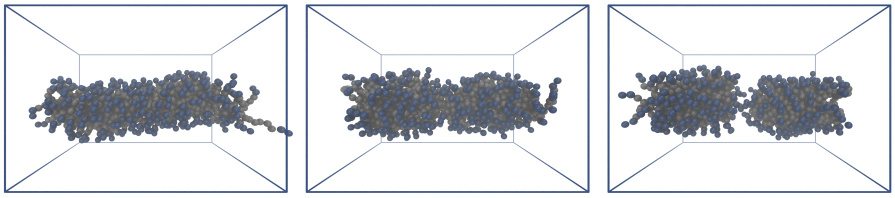

Figure 2.4: Depiction of the scission of a wormlike micelle formed of bola lipids (PC-32-PC) as a continuous micelle in periodic boundary conditions, at an intermediate state along the reaction coordinate λ and the broken WM with two endcaps formed.

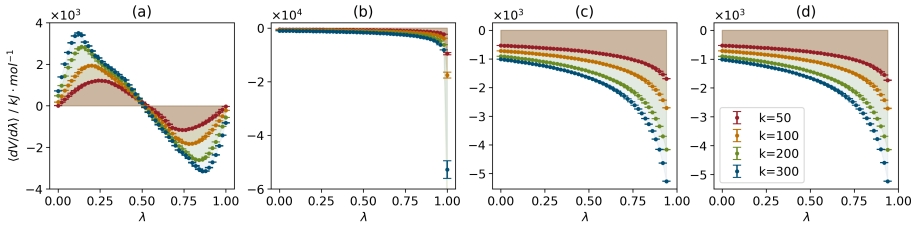

Figure 2.5: Curves for the DFTI of the breaking of a worm-like micelle (WM). (a) Switching of the density field from continuous WM to broken WM. (b) The free energy contribution associated with switching off the restraining field. Notice the strong diverging behaviour close to $\lambda = 1$. (c) Curve for continuous WM omitting the last points along the reaction coordinate that cannot be fully sampled. (d) As in panel c but for a broken WM. Values of the field strength k are in units of $\mathrm{kJmol^{-1}nm^3}$

free for translation across the simulation box and will deform due to thermal fluctuations of the morphology. This can be observed from the divergence in the values of $\langle \frac{\mathrm{d}V_{\mathrm{up}}}{\mathrm{d}\lambda} \rangle$ when λ approaches the value of 1. This divergence is most pronounced in the broken worm-like micelle, i.e. after scission occurred, because the micelle picks up additional fluctuation, translation and rotational modes (see *SI*). Since thermally accessible modes are weak, they are effectively retained until the restraining field nearly vanishes. However, all of these modes are simultaneously released when approaching $\lambda = 1$ giving rise to a strong divergence in the free energy because there exist a large multiple of them and each of these individual modes enters with a thermal free energy contribution. The resulting divergence challenges integration of the free energy since the obtained values in this regime become less reliable (increasing error) while substantially contributing to the

total integral. These final states cannot be sufficiently sampled to obtain a reliable ensemble average, since no true equilibrium for the measured observable $\langle \frac{\delta V}{\delta \lambda} \rangle$ is reached. As a consequence, the points close to $\lambda = 1$ can only be approximated either by linear extrapolation or by fitting an analytical function that models the behaviour of the unrestrained morphology.

The second step of the thermodynamic cycle involves morphing between the two end states while suppressing large scale thermal fluctuations. In contrast to the previous step where the field was switched off, this step of the cycle again yields a well defined, integratable curve. The results of the calculation for different field strengths are shown in Table 2.2. We obtain a value of $\approx 22.4 \pm 2.7\, k_\mathrm{B}T$ ($k\Delta L^3 = 50\,\mathrm{kJmol^{-1}nm^3}$) for the free energy difference between the continuous and the broken wormlike micelle within the external umbrella field. For the alternative route, i.e. integration over the local chemical potential along the path (see Eq. 2.8 and Sec.2.9), we obtained a value of $22.2\, k_\mathrm{B}T$. This value is in good agreement with the value of $\approx 22.4\, k_\mathrm{B}T$ obtained by integration over $\langle \frac{\mathrm{d}V_\mathrm{up}}{\mathrm{d}\lambda} \rangle$, again illustrating that both of these routes are equivalent. Moreover, an end cap free energy of about $20\, k_\mathrm{B}T$ is in excellent correspondence with the value determined by both experiments [39] and simulations of similar worm-like micelles [28].

The evaluation of the full thermodynamic cycle, however, is rendered difficult by the difficulties associated with sampling of morphologies in a vanishing umbrella field and thus do not allow for a reliable estimate. A worm-like micelle thus represents a worst-case scenario for free energy calculations due to the free energy associated with its large translational and rotational degrees of freedom. Interestingly, even for settings where the error in the free-energy average becomes large, the average value itself remains surprisingly similar (within $3\, k_\mathrm{B}T$) for both the broken and continuous worm-like micelle (see Table 2.2). This is likely explained by an effective cancellation of errors because we use a similar simulation protocol (e.g., the same simulation length) in both cases. The magnitude of the overall error generally increases for increasing field strength (see Table 2.2) due to the linear dependence of k on $\frac{\mathrm{d}V_\mathrm{up}}{\mathrm{d}\lambda}$. Decreasing the strength of the field therefore improves accuracy. However, the field must remain sufficiently strong to keep the overall structure and enforce reversible morphing between the two end states. Decreasing field strength thus only provides a limited solution to improve The ability of improving integration accuracy via a decrease in field strength is thus rather limited.

2.3.2.1 Nonlinear Coupling

A common approach to overcome diverging behaviour near endpoints in thermodynamic integration schemes is the choice of a nonlinear coupling

Table 2.2: Results of the DFTI calculations of the free energies of the scission of a worm-like bola lipid micelle (WM) for various force constants k, linear coupling scheme ($f(\lambda) = \lambda$), and quadratic coupling scheme $f(\lambda) = (1 - \lambda)^2$ (colored in grey). Free energy contribution associated with switching off the restraining field (A) the continuous WM and (B) the broken WM. (C) Free energy contribution associated with morphing from a continuous to a broken WM. (D) As in C but now calculated from the chemical potential along the reaction coordinate.(E) Free energy difference calculated along the full thermodynamic cycle. The grey colored region corresponds to the same system using a quadratic coupling scheme (see Fig. 2.10).

$k\Delta L^3$[kJmol^{-1}nm^3]	A [k_BT]	B [k_BT]	C [k_BT]	D [k_BT]	E [k_BT]
50	-305 ± 7	-306 ± 24	22.37 ± 2.69	22.4	22.1±24.8
100	-448 ± 17	-445± 40	20.82 ± 2.35	20.7	23.0±43.8
200	-629 ± 108	-626 ± 57	21.04 ± 2.27	21.0	24.4±122.9
300	-752 ± 53	-749 ± 120	21.91 ± 4.49	22.1	24.9±131.4
50	-315.06 ± 0.8	-316.21 ± 2.62	20.88 ± 2.13	20.8	19.6±3.5

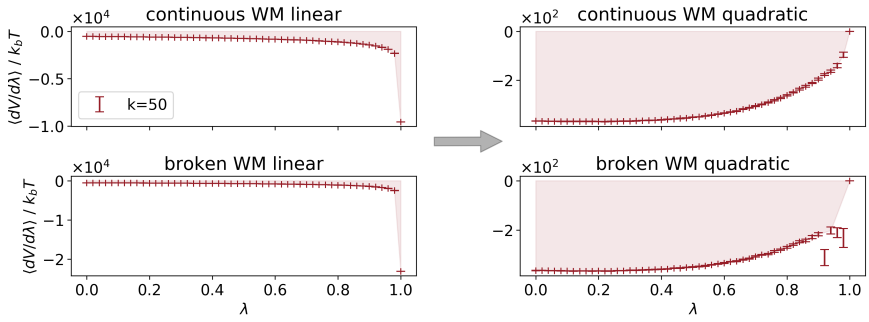

Figure 2.6: Comparison of the curves for switching off the external potential for a worm-like micelle (WM) for linear and quadratic coupling scheme. The total integral (the free energy) is the same for both schemes (the scale differs in the two panels). The large advantage of using a quadratic scheme is that it transfers the divergence to points least contributing to the total integral because $\langle \frac{dV_{up}}{d\lambda} \rangle$ is in such a scheme designed to vanish at $\lambda = 1$. For the full thermodynamic cycle see Fig. 2.10

scheme [40]. This can help to overcome instabilities and find an alternative functional form with a well defined integral. Here, we employed a quadratic coupling scheme, $f(\lambda) = (1 - \lambda)^2$, to improve the integration step involved with switching on/off the external umbrella field. The derivation of this scheme can be found in the *SI* (Sec.2.A). It is noteworthy that this alternative quadratic coupling scheme conserves the value of the total integral and only reshapes the form of the $\langle \frac{\mathrm{d}V_{\mathrm{up}}}{\mathrm{d}\lambda} \rangle$ curve. Indeed, this altered functional form $\langle \frac{\mathrm{d}V_{\mathrm{up}}}{\mathrm{d}\lambda} \rangle$ significantly improves integration and now yields acceptable errors within the estimated free energy difference (i.e., within the order of $k_{\mathrm{B}}T$) since the contribution of the windows with a very weak external potential are down-scaled (see Fig. 2.6 and Fig. 2.10), see Table 2.2. The here-obtained values illustrate that the free energy contribution associated with switching off the field is rather similar for both a continues and broken worm-like micelle, namely $-315.1 \pm 0.8\, k_{\mathrm{B}}T$ versus $-316.2 \pm 2.6\, k_{\mathrm{B}}T$ respectively. This illustrates that most of the free-energy cost is because of translational entropy whereas differences in large scale thermal fluctuations and rational degrees of freedom only marginally contribute to the total entropic cost (a few $k_{\mathrm{B}}T$). Furthermore, the result of the second part of the thermodynamic cycle – the morphing of a continues to a broken worm-like micelle (WM) – yields a free energy difference of $20.88 \pm 2.13\, k_{\mathrm{B}}T$, which compares very well to the value obtained using the linear coupling scheme or the string method. Fig. 2.6 compares the curves obtained for switching off the external umbrella potential for both of the end states of the WM. In case of the broken WM a few data points do not follow the expected smooth curve of the transition. These outliers result from 'lack of obedience' to the applied external potential. The large advantage of using a quadratic scheme is that it transfers the divergence of these windows to points least contributing to the total integral (i.e., the free energy) because $\langle \frac{\mathrm{d}V_{\mathrm{up}}}{\mathrm{d}\lambda} \rangle$ is designed to vanish at $\lambda = 1$. This substantially eases approximation of these values via, for example, linear interpolation (our example). Although the obtained accuracy is already rather satisfactory for our purpose, accuracy may be further improved via the effective removal of rigid-body translation and rotation of the WM due to escaping the vanishing restraining field (e.g., minimizing $\langle \frac{\mathrm{d}V_{\mathrm{up}}}{\mathrm{d}\lambda} \rangle$ for each frame within the trajectory by post processing) or simply by manually discarding 'escape events' (nucleation) from the sampling. We emphasize, however, that for many applications in periodic membrane systems problems with divergence because of 'escape events' are expected to be far less frequent.

Importantly, calculation of the full thermodynamic cycle allows for an unbiased calculation of the actual free energy difference between the continuous and broken WM. It is noteworthy that the linear and quadratic coupling schemes can in principle also be used in a mixed fashion given that the force constant is

conserved. For example, the morphing step can be calculated using the linear scheme, whereas the on/off switching of the field are calculated via the quadratic scheme.

2.3.3 Thermal fluctuations and the free energy estimate

Thus far, our focus was on calculating the full unbiased thermodynamic cycle. Alternatively, the contribution of the external umbrella field can be minimized within the biased umbrella ensemble rather than being subtracted via the full thermodynamic cycle. For such a procedure, the two end states of interest must correspond to local minima within the free energy landscape. Similar to the evolution of the density profiles in the string method (see Sec. 2.2.3), the free energy of the morphologies within the biased ensemble can be minimized using the local chemical potential. The reference densities are iteratively adapted by following the gradient (the excess chemical potential) of the underlying free energy landscape (see Eq. 2.9).

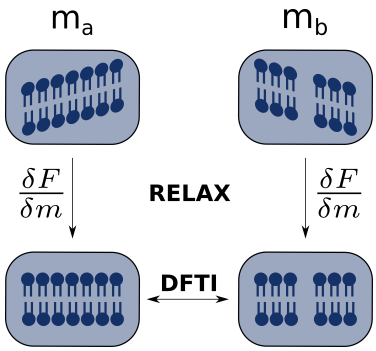

Figure 2.7: Schematic for the thermodynamic Integration with preceding endpoint free energy minimization (density field optimization).

This procedure quenches large thermal fluctuations and yields the structures of lowest free energy. It relies on the approximation that large thermal fluctuations are similarly quenched out for both of the end states thereby conserving the native free energy difference (This approximation is common in polymer field theoretical methods). The density field minimization procedure was tested for the scission of the wormlike micelles (WM) formed by the PC-32-PC bola lipids as well as for the stalk formation. Table 2.3 illustrates the outcome of the thermodynamic integration as a function of field minimization (the number of updates). Since the excess free energy exerted by the external umbrella field is being minimized, the estimated free energy between the end states is expected to decrease in the course

of the minimization procedure until a lower bound is reached. After minimization, the umbrella field is in its ground state and therefore the estimated free energy difference between the two end states becomes independent of the force constant (the mean force exerted against the field vanishes for both end states). This field minimization procedure can be alternatively exploited to both validate and proof meta-stability of the end states since the excess chemical potential must vanish in the course of the minimization if the end state represents a free energy minimum. This vanishing excess chemical potential is indicated by a plateau (convergence) in the free energy in Fig. 2.8.

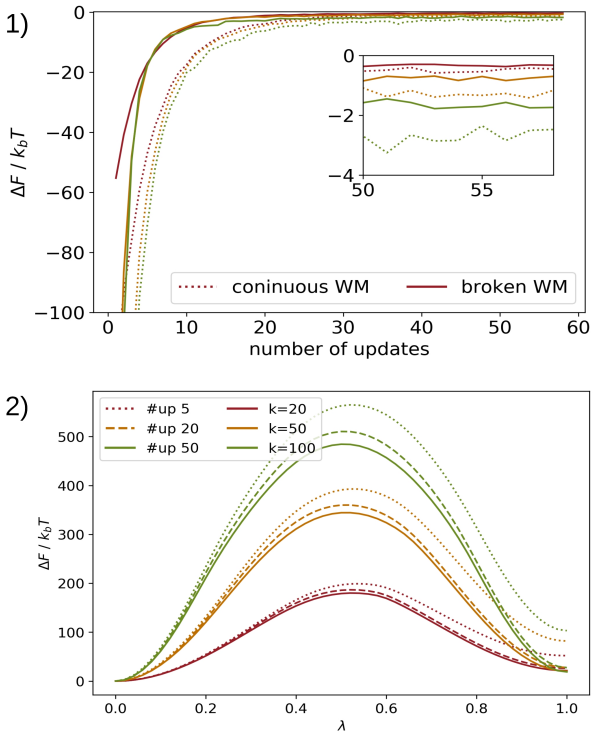

Figure 2.8: Minimization of the external density field. (1) Free-energy differences between updates over a course of 59 minimization steps. After 50 updates the differences level out to order of k_BT indicating that the reference field is close to the local minimum. (2) Calculations of the free-energy differences between the restrained end states via the changes in the density field along the reaction coordinate λ after 5, 20 and 50 minimization steps. Initial deviations because of a difference in field strength k vanish over the course of the minimization.

The alternative 'density field minimization step' followed by direct thermody-

namic integration between the two end states is capable of yielding fast and reliable estimate of the native free energy difference. This method relies on the approximation that the free energy bias introduced by the presence of the field (albeit minimized) is small with respect to the free energy difference of interest. Indeed, even for the highly flexible worm-like micelle system, only a small bias into the native free energy difference between the two end states (being a few k_BT only) is introduced by the minimized field, as evident by comparison with the full thermodynamic cycle. The advantage of the 'density field optimization step' is that the two most involved and computational demanding steps within the full thermodynamic cycle, i.e. switching off the umbrella field for both of the end states, are replaced by two single simulations of the ends states where the reference density and its concomitant umbrella fields are iteratively minimized (this can be done in a single run).

Table 2.3: Results of the DFTI calculations for the scission of a bola WM at different stages of minimization of the endstates (#up). (A) altering of field strength for a continuous WM and (B) the broken WM. (C) switching of the reference density field continuous to broken WM. (D) ΔF calculated from chemical potential along reaction coordinate.

#up	$k\Delta L^3$ [kJmol^{-1}nm^3]	A [k_BT]	B [k_BT]	C [k_BT]	D [k_BT]	E [k_BT]
5	20	-184.89 ±5.89	-217.86 ±10.52	51.90 ±1.88	52.00	19.01
	50	-323.91 ±20.93	-384.49 ±13.73	81.94 ±1.92	81.86	21.44
	100	-468.11 ±73.85	-544.86 ±44.36	103.10 ±3.13	103.13	26.31
20	20	-175.66 ±12.68	-181.54 ±7.87	26.35 ±2.00	26.27	20.36
	50	-308.28 ±43.97	-314.41 ±18.25	27.73 ±2.32	27.72	21.53
	100	-448.69 ±33.50	-452.92 ±40.47	27.75 ±3.91	27.56	23.46
50	20	-172.48 ±10.18	-173.75 ±9.15	21.53 ±1.89	21.42	20.19
	50	-304.23 ±25.49	-302.84 ±24.75	20.09 ±2.02	20.21	21.55
	100	-444.17 ±54.44	-440.48 ±42.99	18.57 ±4.34	18.80	22.52

Furthermore, the clear advantage over other related methods such as the string method is its lesser computational demand. For the string method all structures along the path need to be simulated and updated in every iteration and convergence towards the MFEP is often very slow, therefore demanding many updates (often in the order of 10^2). It is noteworthy that the string does not have to converge to the MFEP to obtain the free-energy difference between the two end states given that these end states have already converged to the local minimum. Hence, such a scenario would be analogous to the chemical potential along some nonphysical path connecting two free energy minima (see Table 2.3, column D). In case of density field thermodynamic integration, only the end states need to be updated, and which can be done very quickly since no communication between the morphologies is required (they are independent), which yields

the lesser computational demand compared to the string method. After field minimization subsequent thermodynamic integration is performed via a single additional simulation step that can easily be automatised and run in parallel. Of course, in contrast to the string method, the obtained pathway remains nonphysical and does not allow the calculation of barriers which are naturally calculated using the string method.

2.3.4 Conclusion

The thermodynamic integration scheme, coined 'Density Field Thermodynamic Integration' (DFTI), outlined above was used to compute the free-energy differences between two meta-stable states in the example of (i) the formation of a hemifusion stalk between two lipid bilayers and (ii) the scission of a worm-like micelle. The calculation of free energy differences in lipidic systems is a challenging task because of the fluid nature of self-assembled systems, especially when including the contribution of thermal fluctuations. General purpose methods aimed to calculate free energies of self-assembled surfactant structures in Lennard-Jones based molecular dynamics simulations are still limited to pioneering studies. Bubnis et al. previously proposed umbrella sampling of collective Eigen modes (Principle Component Analysis) in conjunction with a permutation reduction algorithm to correct for the diffusivity of surfactant molecules [17]. This method is highly effective when structural changes are characterized by a dominant collective mode such as, for example, bending of a membrane sheet [17]. Large collective modes can be alternatively modeled by explicitly using membrane curvature as a collective reaction coordinate [41]. However, smoothly enforcing the structure through a transition state of single molecular nature (our two example systems) is hard to achieve by coupling to only a single or even a few collective modes. Consequently, ensuring thermodynamic reversibility may thus be rather challenging.

Our results illustrate that DFTI can provide a fast, versatile and rather reliable general purpose method for free energy calculations in surfactant assemblies. Local hydrophobic density enables a high dimensional thermodynamically reversible reaction coordinate that is able to capture structural intermediates even of a single molecular nature (high resolution). The additional computational cost associated with the density assignment and concomitant force calculation is very low (single 'for' loops) and scales linearly with system size. Usage of a quadratic coupling scheme offers a marked improvement in the accuracy of the obtained thermodynamic cycle, especially in systems that possess large translational and rotational degrees of freedom. Integration accuracy may be even further improved by post processing of the obtained trajectory. For example, rigid-body translation

and rotation of a lipid assembly due to escaping the vanishing restraining field could be effectively removed via a fitting procedure which minimizes $\langle \frac{\mathrm{d}V_{\mathrm{up}}}{\mathrm{d}\lambda} \rangle$ for each frame within the trajectory. Furthermore, the alternative 'density field minimization' path allows for comparatively quick calculations of free energy differences by quenching thermal fluctuations in a minimization step, followed by a subsequent thermodynamic integration step. Notably, the here-obtained results compare well to the values obtained with the computationally more demanding string method which in contrast yields a likely, physical free energy pathway [10]. Thus, given that the end states are of minimum free energy (i.e., the retraining field is in its ground state), accurate calculation of their free energy difference does not require a physical path. Although not yielding a physical pathway, we conclude that DFTI methods provides a valuable tool to both efficiently and rapidly quantify the free energy difference between meta-stable states. Furthermore, our finding that the free energy bias due to the presence of the minimized field is rather small (a few $k_{\mathrm{B}}T$ only), as evident by our calculation of the full thermodynamic cycle, advocates the potential of density field based string methods in resolving likely reaction pathways in soft, diffusive materials.

Acknowledgements. We thank M. Müller for sharing his expertise in many fruitful discussions. We thank J. Orozco for useful disscussions and support. This research was supported by the SFB-803 project B03 financed by the DFG and the Life at the Nanoscale project (life@nano) funded by the state of Lower Saxony (Germany). Computational resources where provided by HLRN and NIC Jülich.

References

[1] Bassereau, P. et al. "The 2018 biomembrane curvature and remodeling roadmap". In: *J. Phys. D: Appl. Phys.* Vol. 51, no. 34 (July 2018), p. 343001.

[2] Mattila, J.-P. et al. "A hemi-fission intermediate links two mechanistically distinct stages of membrane fission". In: *Nature* vol. 524, no. 7563 (2015), pp. 109–113.

[3] D'Agostino, M. et al. "A tethering complex drives the terminal stage of SNARE-dependent membrane fusion". In: *Nature* vol. 551, no. 7682 (2017), pp. 634–638.

[4] Risselada, H. J. and Mayer, A. "SNAREs, tethers and SM proteins: how to overcome the final barriers to membrane fusion?" In: *Biochem. J.* Vol. 477, no. 1 (Jan. 2020), pp. 243–258.

[5] Schuldiner, M. and Bohnert, M. “A different kind of love–lipid droplet contact sites”. In: *Biochim. Biophys. Acta* vol. 1862, no. 10 (2017), pp. 1188–1196.

[6] Olzmann, J. A. and Carvalho, P. “Dynamics and functions of lipid droplets”. In: *Nat. Rev. Mol. Cell. Biol.* Vol. 20, no. 3 (2019), pp. 137–155.

[7] Zoni, V. et al. “To Bud or Not to Bud: A Perspective on Molecular Simulations of Lipid Droplet Budding”. In: *Front. Mol. Biosci.* Vol. 6 (Nov. 2019).

[8] Wong, F. and Amir, A. “Bacterial cell lysis: geometry, elasticity, and implications”. In: (June 2018).

[9] Allolio, C. et al. “Arginine-rich cell-penetrating peptides induce membrane multilamellarity and subsequently enter via formation of a fusion pore”. In: *Proc. Natl. Acad. Sci. U.S.A* vol. 115, no. 47 (Nov. 2018), pp. 11923–11928.

[10] Smirnova, Y. G., Risselada, H. J., and Müller, M. “Thermodynamically reversible paths of the first fusion intermediate reveal an important role for membrane anchors of fusion proteins”. In: *Proc. Natl. Acad. Sci. U.S.A* vol. 116, no. 7 (2019), pp. 2571–2576.

[11] Cates, M. E. and Candau, S. J. “Statics and dynamics of worm-like surfactant micelles”. In: *J. Phys. Condens. Matter* vol. 2, no. 33 (Aug. 1990), 6869–6892.

[12] Yang, J. “Viscoelastic wormlike micelles and their applications”. In: *Curr. Opin. Colloid Interface Sci.* Vol. 7, no. 5-6 (Nov. 2002), pp. 276–281.

[13] Larson, R. G. “The lengths of thread-like micelles inferred from rheology”. In: *J. Rheol.* Vol. 56, no. 6 (2012), pp. 1363–1374.

[14] Rogers, S. A., Calabrese, M. A., and Wagner, N. J. “Rheology of branched wormlike micelles”. In: *Curr. Opin. Colloid Interface Sci.* Vol. 19, no. 6 (2014), pp. 530–535.

[15] Norizoe, Y., Daoulas, K. C., and Müller, M. “Measuring excess free energies of self-assembled membrane structures”. In: *Faraday Discuss.* Vol. 144 (2010), pp. 369–391.

[16] Müller, M. et al. “Transition Path from Two Apposed Membranes to a Stalk Obtained by a Combination of Particle Simulations and String Method”. In: *Phys. Rev. Lett.* Vol. 108 (22 May 2012), p. 228103.

[17] Bubnis, G., Risselada, H., and Grubmueller, H. “Free Energy Landscapes of Vesicle Fusion by Umbrella Sampling MD Simulations”. In: *Biophys. J.* Vol. 104, no. 2 (2013), 92a.

[18] Smirnova, Y. G. et al. “Free-energy calculation methods for collective phenomena in membranes”. In: *J. Phys. D: Appl. Phys.* Vol. 48, no. 34 (2015), p. 343001.

[19] Frenkel, D. and Ladd, A. J. “New Monte Carlo method to compute the free energy of arbitrary solids. Application to the fcc and hcp phases of hard spheres”. In: *J. Chem. Phys.* Vol. 81, no. 7 (1984), pp. 3188–3193.

[20] Müller, M., Daoulas, K. C., and Norizoe, Y. “Computing free energies of interfaces in self-assembling systems”. In: *Phys. Chem. Chem. Phys.* Vol. 11, no. 12 (2009), p. 2087.

[21] Almarza, N. G. “Computation of the free energy of solids”. In: *J. Chem. Phys.* Vol. 126, no. 21 (June 2007), p. 211103.

[22] Vega, C. and Noya, E. G. “Revisiting the Frenkel-Ladd method to compute the free energy of solids: The Einstein molecule approach”. In: *J. Chem. Phys.* Vol. 127, no. 15 (Oct. 2007), p. 154113.

[23] Sellers, M. S., Lísal, M., and Brennan, J. K. “Free-energy calculations using classical molecular simulation: application to the determination of the melting point and chemical potential of a flexible RDX model”. In: *Phys. Chem. Chem. Phys.* Vol. 18, no. 11 (2016), pp. 7841–7850.

[24] Smirnova, Y. G. et al. “Solvent-exposed tails as prestalk transition states for membrane fusion at low hydration”. In: *J. Am. Chem. Soc.* Vol. 132, no. 19 (2010), pp. 6710–6718.

[25] Kawamoto, S. and Shinoda, W. “Free energy analysis along the stalk mechanism of membrane fusion”. In: *Soft Matter* vol. 10, no. 17 (2014), pp. 3048–3054.

[26] Risselada, H. J., Bubnis, G., and Grubmuller, H. “Expansion of the fusion stalk and its implication for biological membrane fusion”. In: *Proc. Natl. Acad. Sci. U.S.A* vol. 111, no. 30 (July 2014), pp. 11043–11048.

[27] Hömberg, M. and Müller, M. “Main phase transition in lipid bilayers: Phase coexistence and line tension in a soft, solvent-free, coarse-grained model”. In: *J. Chem. Phys.* Vol. 132, no. 15 (2010), 04B609.

[28] Wang, H. et al. “Scission free energies for wormlike surfactant micelles: development of a simulation protocol, application, and validation for personal care formulations”. In: *Langmuir* vol. 34, no. 4 (2018), pp. 1564–1573.

[29] Otter, W. K. den. “Free energies of stable and metastable pores in lipid membranes under tension”. In: *J. Chem. Phys.* Vol. 131, no. 20 (2009), 11B614.

[30] Wohlert, J. et al. “Free energy of a trans-membrane pore calculated from atomistic molecular dynamics simulations”. In: *J. Chem. Phys.* Vol. 124, no. 15 (2006), p. 154905.

[31] Ting, C. L. et al. “Metastable prepores in tension-free lipid bilayers”. In: *Phys. Rev. Lett.* Vol. 120, no. 12 (2018), p. 128103.

[32] Blokhuis, E. M. et al. “Fusion Pores Live on the Edge”. In: *J. Phys. Chem. Lett.* Vol. 11, no. 4 (Jan. 2020), pp. 1204–1208.

[33] Smirnova, Y. and Müller, M. “Calculation of membrane bending rigidity using field-theoretic umbrella sampling”. In: *J. Chem. Phys.* Vol. 143, no. 24 (2015), p. 243155.

[34] Weinan, E, Ren, W., and Vanden-Eijnden, E. “Simplified and improved string method for computing the minimum energy paths in barrier-crossing events”. In: *J. Chem. Phys.* Vol. 126, no. 16 (2007), p. 164103.

[35] Schiferl, S. K. and Wallace, D. C. “Statistical errors in molecular dynamics averages”. In: *J. Chem. Phys.* Vol. 83, no. 10 (1985), pp. 5203–5209.

[36] Bussi, G., Donadio, D., and Parrinello, M. “Canonical sampling through velocity rescaling”. In: *J. Chem. Phys.* Vol. 126, no. 1 (2007), p. 014101.

[37] Kozlovsky, Y. and Kozlov, M. M. “Stalk Model of Membrane Fusion: Solution of Energy Crisis”. In: *Biophysical Journal* vol. 82, no. 2 (Feb. 2002), pp. 882–895.

[38] Blume, A. et al. “Self-assembly of different single-chain bolaphospholipids and their miscibility with phospholipids or classical amphiphiles”. In: *Adv. Colloid Interface Sci.* Vol. 208 (2014), pp. 264–278.

[39] Danov, K. D. et al. “Growth of wormlike micelles in nonionic surfactant solutions: Quantitative theory vs. experiment”. In: *Adv. Colloid Interface Sci* vol. 256 (June 2018), pp. 1–22.

[40] Steinbrecher, T., Mobley, D. L., and Case, D. A. “Nonlinear scaling schemes for Lennard-Jones interactions in free energy calculations”. In: *J. Chem. Phys.* Vol. 127, no. 21 (2007), p. 214108.

[41] Bouvier, B. “Curvature as a Collective Coordinate in Enhanced Sampling Membrane Simulations”. In: *J. Chem. Theory Comput.* Vol. 15, no. 12 (Oct. 2019), pp. 6551–6561.

Appendix 2.A Supporting Information

2.A.1 Derivation of the Functional Form of $\frac{\mathrm{d}V_{up}}{\mathrm{d}\lambda}$

The umbrella potential acting on a given morphology is given by,

$$V_{\mathrm{up}}(\mathbf{r},\lambda) = \frac{k(\lambda)}{2}\int_V \mathrm{d}^3\mathbf{r}[m(\mathbf{r},\lambda) - \hat{m}(\mathbf{r},\{\mathbf{r}\})]^2$$

where the reference density $m(\mathbf{r})$ and the coupling strength k are functions of the coupling parameter λ. $m_{a,b}$ and $k_{a,b}$ are the density and force constant corresponding to end states a and b respectively.

$$m(\mathbf{r},\lambda) = f(\lambda)m_b(\mathbf{r}) + [1 - f(\lambda)]m_a(\mathbf{r})$$

$$k(\lambda) = f(\lambda)k_b + [1 - f(\lambda)]k_a$$

The derivative with respect to the coupling parameter is calculated by

$$\begin{aligned}\frac{\mathrm{d}V_{\mathrm{up}}(\lambda)}{\mathrm{d}\lambda} =& \frac{1}{2}\frac{\mathrm{d}k(\lambda)}{\mathrm{d}\lambda}\int_V \mathrm{d}^3\mathbf{r}[m(\mathbf{r},\lambda) - \hat{m}(\mathbf{r},\{\mathbf{r}\})]^2 \\ &+k(\lambda)\int_V \mathrm{d}^3\mathbf{r}[m(\mathbf{r},\lambda) - \hat{m}(\mathbf{r},\{\mathbf{r}\})]\frac{\mathrm{d}m(\mathbf{r},\lambda)}{\mathrm{d}\lambda}\end{aligned} \tag{2.11}$$

Using the discretized collocation lattice for calculation of the local densities the integration over the box volume becomes a summation over all lattice points.

$$\begin{aligned}\frac{\mathrm{d}V_{\mathrm{up}}(\lambda)}{\mathrm{d}\lambda} =& \frac{1}{2}\frac{\mathrm{d}k(\lambda)}{\mathrm{d}\lambda}\sum_{\mathbf{c}}[m(\mathbf{c},\lambda) - \hat{m}(\mathbf{c},\{\mathbf{r}\})]^2 \\ &+k(\lambda)\sum_{\mathbf{c}}[m(\mathbf{c},\lambda) - \hat{m}(\mathbf{c},\{\mathbf{r}\})]\frac{\mathrm{d}m(\mathbf{c},\lambda)}{\mathrm{d}\lambda}\end{aligned} \tag{2.12}$$

The calculations in Eq. 2.12 take into account the contribution of each grid point in every molecular dynamics step. Here, $m(\mathbf{c}), \hat{m}(\mathbf{c})$ denote the local reference density and the local instantaneous density respectively.

2.A.1.1 Linear Coupling $f(\lambda) = \lambda$

Part 1: The field strength is changed with λ ($k_a = 0,\ k_b = k$). The reference field is kept constant ($m_a = m_b = m$):

$$\frac{\mathrm{d}V_{\mathrm{up},\mathbf{c}}}{\mathrm{d}\lambda} = \frac{k}{2}[m(\mathbf{c}) - \hat{m}(\mathbf{c})]^2$$

Part2 The reference density is changed over the course of λ and the field strength is kept constant ($k_a = k_b = k$):

$$\frac{\mathrm{d}V_{\mathrm{up},\mathbf{c}}}{\mathrm{d}\lambda} = k\left[\lambda m_b(\mathbf{c}) + (1-\lambda)m_a(\mathbf{c}) - \hat{m}(\mathbf{c})\right]\left[m_b(\mathbf{c}) - m_a(\mathbf{c})\right]$$

2.A.1.2 Quadratic Coupling $f(\lambda) = (1-\lambda)^2$

Part 1: The field strength is changed with λ ($k_a = 0,\ k_b = k$). The reference field is kept constant ($m_a = m_b = m$):

$$\frac{\mathrm{d}V_{\mathrm{up},\mathbf{c}}}{\mathrm{d}\lambda} = k(\lambda - 1)[m(\mathbf{c}) - \hat{m}(\mathbf{c})]^2$$

Part2 The reference density is changed over the course of λ and the field strength is kept constant ($k_a = k_b = k$):

$$\frac{\mathrm{d}V_{\mathrm{up},\mathbf{c}}}{\mathrm{d}\lambda} = 2k(1-\lambda)[m_a(\mathbf{c}) + (1-\lambda)^2(m_b(\mathbf{c}) - m_a(\mathbf{c})) - \hat{m}(\mathbf{c})](m_a(\mathbf{c}) - m_b(\mathbf{c}))$$

2.A.2 Scission of a Wormlike Micelle

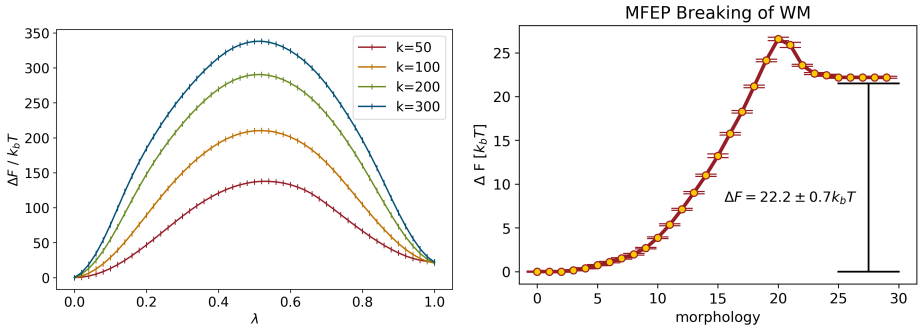

Figure 2.9: *left:* Scission of WM in external potential: Cumulative change of free energy along reaction coordinate calculated from the chemical potential. The obtained free energy difference between the end states is independent of the used force constant. *right:* Corresponding minimum free energy path (MFEP) calculated using the string method.

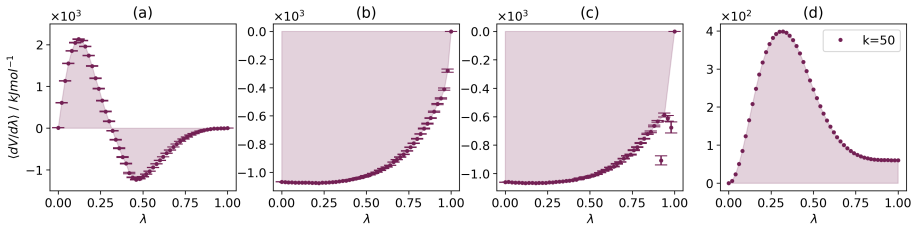

Figure 2.10: Curves for the DFTI of the breaking of a WM using the quadratic coupling scheme ($f(\lambda) = (1-\lambda)^2$. (a) Morphing between a continuous WM to broken WM. (b) Curve for a continuous WM (c) like (b) but for broken WM. The deviation close to $\lambda = 0$ are because the structure 'escapes' the vanishing restraining field in the course of the simulation. However, the effect on the area of total integral remains limited. Accuracy may be further improved by manually omitting these 'escape events' from the averaging. (d) Change of free energy along the reaction coordinate λ calculated from the changes in the density field along the transition path (compare Eq. 6)

2.A.3 Formation of a Hemifusion Stalk

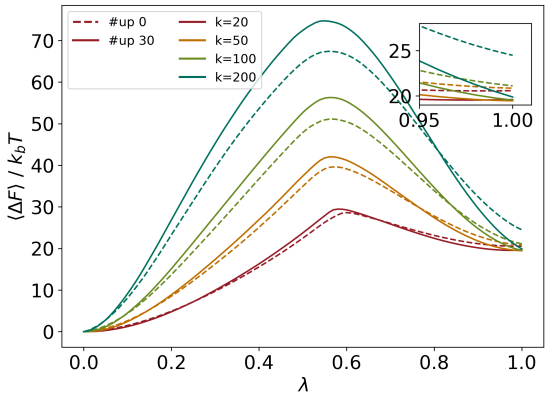

Figure 2.11: Cumulative change of free energy along reaction coordinate calculated from the chemical potential for different k for stalk formation at a inter-membrane distance of 1.2 nm (≡ 220 water beads). Calculations were performed for initial reference densities (# up 0) and after 30 minimization steps. Minimization quenches fluctuations responsible for for the dependence of the free energy difference on the field strength in the initial states.

2.A.4 How entropy causes strong divergence in $\langle \frac{\mathrm{d}V}{\mathrm{d}\lambda} \rangle$: a 2D toy model

In the following section we illustrate from a statistical mechanical principle how $\langle \frac{\mathrm{d}V}{\mathrm{d}\lambda} \rangle$ diverges when a system is subject to a vanishing umbrella potential. Our simplified toy model is comprised of one particle in a discretized 2D box subject to an external umbrella potential. For this system we know the partition function and are able to analytically determine the derivative of the potential with respect to the reaction coordinate λ. In a weak external potential the particle is free to explore the space outside of the reference field thus leading to a diverging curve for $\langle \frac{\mathrm{d}V}{\mathrm{d}\lambda} \rangle$.

We imagine a Box with N^2 cells (c) of volume ΔL^2=1. **A** is defined as reference state for a particle located somewhere in this box. This particle serves as analogy for a molecular conformation used in our simulations. The particles location is described by its density, therefore the 'instantaneous density' $\hat{\rho}$ in a cell is 1 if the particle is located in this particular cell. In all other cells $\hat{\rho} = 0$. The reference density is uniformely distributed over all cells in **A**. Therefore, every cell has a density $\rho_r = \frac{1}{n^2}$ since the overall number density is normalized to 1. Outside

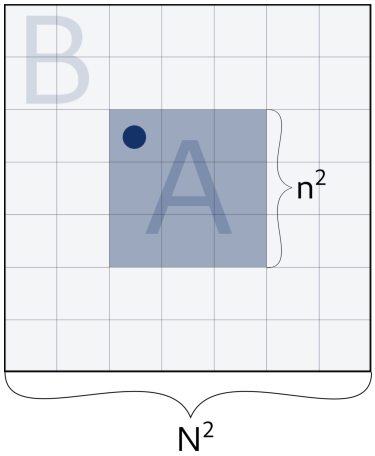

Figure 2.12: Particle in a discretized box. An external harmonic potential V is acting on the particle according to a reference density. The reference density is $\frac{1}{n^2}$ in A and 0 in B.

of this area (**B**) the reference density is $\rho_r = 0$. The particle is subjected to an external harmonic potential of the form:

$$V(\lambda) = \frac{k(\lambda)}{2} \sum_c (\hat{\rho} - \rho_r)^2 \tag{2.13}$$

We chose our force constant according to our simulation procedure, which means switching the straight of the potential from k to 0 along the reaction coordinate λ. for $k(\lambda) = \lambda k_1 + (1 - \lambda)k_0$, $k_0 = k$ and $k_1 = 0$ the potential reads

$$V(\lambda) = \frac{(1 - \lambda)k}{2} \sum_c (\hat{\rho} - \rho_r)^2 \tag{2.14}$$

We can define the partition function Z and the derivative of the free energy as,

$$Z = \int e^{\left(-\frac{H}{k_B T}\right)} \mathrm{d}\Gamma \approx \sum_c e^{(-\frac{V}{k_B T})} \Delta L^2 \tag{2.15}$$

and

$$\begin{aligned} \frac{\mathrm{d}F}{\mathrm{d}\lambda} &= \frac{\mathrm{d}}{\mathrm{d}\lambda}[-k_B T \ln Z] = \frac{-k_B T}{Z} \frac{\mathrm{d}Z}{\mathrm{d}\lambda} \\ &= \frac{-k_B T}{Z} \frac{\mathrm{d}}{\mathrm{d}\lambda} \sum_c \exp\left(-\frac{(1 - \lambda)k}{2k_B T} \sum_c (\hat{\rho} - \rho_r)^2\right) \\ &= \left\langle \frac{\mathrm{d}V}{\mathrm{d}\lambda} \right\rangle = -\frac{k}{2} \left\langle \sum_c (\hat{\rho} - \rho_r)^2 \right\rangle \end{aligned} \tag{2.16}$$

We can distinguish two cases:

- particle in reference field **A** ($\rho_r = \frac{1}{n^2}$)
- particle outside reference field $\rightarrow$ in **B** ($\rho_r = 0$)

The sum over the cells in the potential can be split accordingly:

$$V(\lambda) = \frac{k(\lambda)}{2}\Big(\sum_A (\hat{\rho} - \frac{1}{n^2})^2 + \sum_B (\hat{\rho} - 0)^2\Big) \tag{2.17}$$

If the particle is in one cell of **A** $\hat{\rho}$ is 1 in one cell and 0 in all $n^2 - 1$ remaining cells in **A** and in **B**. The potential takes the form:

$$V_A(\lambda) = \left[-\frac{(1-\lambda)k}{2k_\mathrm{B}T}\left(1 - \frac{1}{n^2}\right)\right] \tag{2.18}$$

If the particle is located in **B** the potential reads:

$$V_B(\lambda) = \left[-\frac{(1-\lambda)k}{2k_\mathrm{B}T}\left(1 + \frac{1}{n^2}\right)\right] \tag{2.19}$$

There are n^2 equal states where the particle is in one of the cells of **A** and $N^2 - n^2$ equal states for the particle outside this area (**B**). Therefore we can calculate the partition function as

$$\begin{aligned} Z =& n^2 \exp\left[-\frac{(1-\lambda)k}{2k_\mathrm{B}T}\left(1 - \frac{1}{n^2}\right)\right] \\ &+ (N^2 - n^2)\exp\left[-\frac{(1-\lambda)k}{2k_\mathrm{B}T}\left(1 + \frac{1}{n^2}\right)\right] \end{aligned} \tag{2.20}$$

The ensemble average over the derivative of the potential with respect to the coupling parameter λ can be calculated as

$$\left\langle \frac{\mathrm{d}V}{\mathrm{d}\lambda} \right\rangle = -\frac{k}{2}\frac{n^2\left(1-\frac{1}{n^2}\right)\exp\left[-\frac{(1-\lambda)k}{2k_\mathrm{B}T}\left(1-\frac{1}{n^2}\right)\right] + (N^2-n^2)\left(1+\frac{1}{n^2}\right)\exp\left[-\frac{(1-\lambda)k}{2k_\mathrm{B}T}\left(1+\frac{1}{n^2}\right)\right]}{n^2\exp\left[-\frac{(1-\lambda)k}{2k_\mathrm{B}T}\left(1-\frac{1}{n^2}\right)\right] + (N^2-n^2)\exp\left[-\frac{(1-\lambda)k}{2k_\mathrm{B}T}\left(1+\frac{1}{n^2}\right)\right]} \tag{2.21}$$

Fig. 2.13 shows the behaviour of the above derived model Eq. 2.21 for decreasing the external field strength. As in the simulated systems the model system picks up translational degrees of freedom in a week external field which leads to the diverging behaviour.

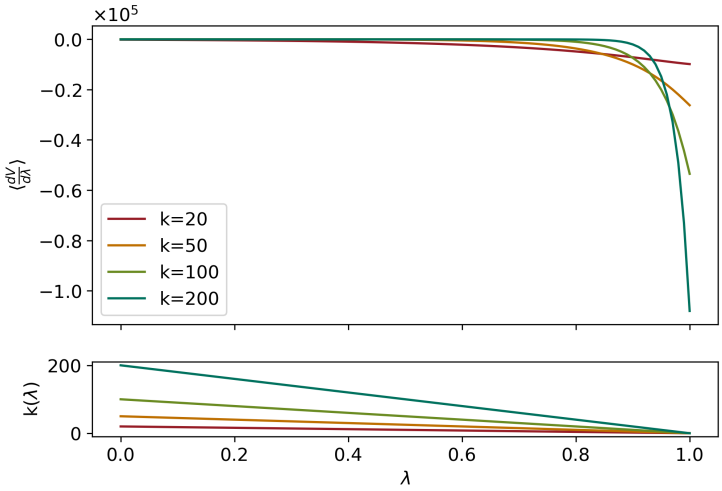

Figure 2.13: Behaviour of the particle in a discretized box when linearly decreasing the strength of the external field. Note the strong divergence of $\frac{dV}{d\lambda}$ when λ approaches 1. The observed behavior is in well agreement with the divergence observed in surfactant assemblies subject to a vanishing high dimensional umbrella field. It also illustrates that usage of a weaker force constant indeed reduces divergence.

Chapter 3

“Where are those lipid nano rings?”

Laura Josefine Endter, Herre Jelger Risselada

Published in *Journal of Colloid and Interface Science*, April 2021, volumne 587, pp. 789–796, DOI: 10.1016/j.jcis.2020.11.038.

Abstract

Highly curved toroidal micelles with diameters as small as 100 nm have been successfully constructed by self-assembly of amphiphilic block copolymers. These structures may have an interesting potential for gene or drug delivery. Experimental observations suggest that toroidal micelles likely originate from spherical or disc-like micelles which are tricked into forming toroidal micelles upon external stimuli (‘smart’ materials). Since self-assembly of polymeric and lipid surfactants is guided by the same physical principles, we hypothesize that ‘smart’ lipid surfactants can be equivalently tricked into forming highly curved toroidal micelles that are tenfold smaller ($\simeq$10 nm diameter). Paradoxically, these ‘nano rings’ have never been observed. Using coarse-grained molecular dynamics (MD) simulations in conjunction with a state-of-the-art free energy calculation method (a string method), we illustrate how a thermo-responsive lipid surfactant is able to form toroidal micelles. These micelles originate from disc-like micelles that are spontaneously perforated upon heat shocking, thereby supporting a longstanding hypothesis on the possible origin of polymeric toroidal micelle phases observed in experiments. We illustrate that kinetically stable ‘nano rings’ are substantially shorter lived than their tenfold larger polymeric analogs. The estimated life-time (milliseconds) is in fact similar to the characteristic breaking time of the corresponding worm-like micelle. Finally, we resolve the characteristic finger print which ‘nano

rings’ leave in time-resolved X-ray spectra and illustrate how the uptake of small DNA fragments may enhance their stability. Despite a shared kinetics of self-assembly, length scale dependent differences in the lifetime of surfactant phases can occur when phases are kinetically rather than thermodynamically stable. This results in the apparent absence or presence of toroidal micelle phases on different length scales. Our theoretical work precisely illustrates that the universality of surfactants nevertheless remains conserved even at different length scales.

Contents

3.1 Introduction

Directed self-assembly of surfactants plays an important role in the development of novel nanostructures utilized in, for example, gene and drug delivery [1–6]. In particular, toroidal nanostructures are of growing importance due to their unique geometry and potential utility in material fabrication. In recent years a variety of amphiphilic block copolymers have been shown capable to self-assemble into toroidal micelles (e.g., [7–14]). The diameter of the smallest toroidal micelles formed by amphiphilic polymers is about 100 nm [9].

The thermodynamic stability of toroidal micelles has been extensively studied using continuum elastic models (e.g., citation [15]) or self-consistent field theory (e.g., citation [16]). The excess free energy of a toroidal micelle is predominantly determined by its bending free energy. Modeling the torus by a circle [17], the bending free energy is given by, $F_b = \frac{\kappa\pi}{R}$, with R being the radius of the torus and κ the elastic bending modulus (See SI for further details). The formation of toroidal micelles from cylinder-forming amphiphilic molecules in solution was initially thought to occur through fusion of the micelle’s free end caps in an end-to-end fashion [18–20]. For a worm-like or rod-like micelle with contour length L, toroidal micelle formation is thermodynamically favorable

when the free energy of its two free end caps, $2F_{\mathrm{cap}}$, becomes larger than the bending free energy of the corresponding toroidal micelle, thus $2F_{\mathrm{cap}} > \frac{2\kappa\pi^2}{L}$. For micelles undergoing 'chain growth polymerization' toroidal micelle formation will eventually become thermodynamically favorable, because the bending energy stored in the torus vanishes with increasing contour length ($\propto 1/L$). However, ring formation via fusion of the two free ends is opposed by an entropic free energy cost that according to random walk statistics increases with the logarithm of the contour length, $\propto \ln L$ (see *SI* for a detailed explanation) The total free energy barrier against ring formation, F^*_{ring}, is given by, $F^*_{\mathrm{ring}} = \frac{2\kappa\pi^2}{L} + c(T)\ln L + F_0$, with $c(T)$ and F_0 being constant terms. Figure 3.1a sketches the kinetic free energy barrier against ring formation as a function of L. The plot illustrates the existence of an optimum fibril length at which formation of a toroidal micelle is most likely. However, a growing and sufficiently stiff worm-like or rod-like micelle will overshoot such a regime. Therefore, formation of a ring, despite being thermodynamically favorable, is generally a rare event, albeit less rare in floppy worm-like micelles with attractive free ends [21]. In support of such a notion, experimental observations have hypothesized that highly curved toroids in ABC triblock copolymers are constructed either through elimination of high-energy spherical micelles and/or cylindrical micelle end caps, or through perforation of disc-like micelles [8]. Extensive mesoscopic field-based simulations of single-component amphiphilic diblock copolymer systems prompted that toroidal micelles are formed from growing spherical micelles that suddenly transit into toroidal micelles [22]. A similar transition has been observed in coarse-grained dissipative particle dynamics simulations of triblock copolymers [23]. In these pathways, the micelles do not coalesce, but rather grow radially by attracting copolymers from the solution. Once a critical micelle size is exceeded, copolymers start to flip-flop such that the micelle's core becomes hydrophilic and transits into a toroidal micelle.

Experimental fabrication of highly curved toroidal micelles is commonly based on exploiting the stimuli-responsiveness of polymeric surfactants [8–10]. Stimuli-responsive or 'smart' materials are capable of altering their physical properties upon exposure to external stimuli. Formation of toroidal micelles is actively induced by gradually changing solvent conditions (e.g., the ratio between ethanol and THF) [8, 9]. This alters the solubility of the blocks and consequently impairs the thermodynamic stability of a pre-existing spherical or disc-like micelle structure thereby stimulating the subsequent kinetic transition into a toroidal micelle [8, 9]. It is still an open question whether also lipids or other small sized amphiphiles can form toroidal micelles via stimuli-directed self-aggregation. Although lipid and polymeric surfactants form similar lyotropic phases [4, 5], highly curved lipid toroidal micelle phases have thus far not been

experimentally observed. Given the characteristic hydrophobic thickness of lipid self-assemblies [5], being about 4 nm, the lower size limit of a highly curved toroidal micelle would be in the range of about 10 nm – a size of interest for potential applications in the biomedical field. Lipid ‘nano rings’ could, for example, be envisioned as biocompatible transporters or vehicles of short DNA and RNA fragments. However, it is remains unclear whether highly curved lipid toroidal micelle phases are actually kinetically accessible.

Molecular simulations provide a growing and powerful tool to explore the complex landscape of surfactant self-assembly [24]. Here, we use coarse-grained molecular dynamics (MD) simulations in conjunction with a state-of-the-art free energy calculation method (a string method) to shed some light into the complex kinetics and free energy landscape of stimuli-directed self-aggregation. We illustrate the example of a thermo-responsive ‘smart’ lipid surfactant that forms hexagonal shaped disc-like micelle structures below the chain melting temperature (T_m), which are tricked into forming 10 nm-sized toroidal micelles (‘nano rings’) rather than worm-like-micelles upon heat shocking (>> T_m). Finally, we illustrate that kinetically stable ‘nano rings’ are substantially shorter lived than their tenfold larger polymeric analogs.

3.2 Methods

Molecular dynamics (MD) simulations were performed performed with the Gromacs simulation package [25] version 2019, unless stated otherwise, using the Martini coarse-grained (CG) model for bio-molecular simulations version 2.2. The Martini model is parametrized on representing thermodynamic properties such as partitioning free energies of alkanes in water [26]. The modeled lipid surfactant – a single chain bolaamphiphile [27–29] – mimicks a saturated hydrophobic chain consisting of 32 CH_2 units (B-block) connected to two hydrophilic zwitterionic phosphocholine (PC) headgroups on both ends (A-block) [30]. Its symmetric A–B–A architecture is in fact equivalent to that of a Pluronic – a widely used family of thermo-responsive symmetric triblock copolymers manufactured by BASF [31–33]. A detailed description of all simulation techniques, including force-field parameters, used in this study can be found in the extended method section within the *SI*.

Minimum free energy pathways were resolved using a density-field based string method implemented in Gromacs version 4.6.4 (see *SI* and citation [34] for further details on this method). Reported simulation times have been corrected for the about four times faster diffusion of the coarse-grained model in comparison to atomistic simulations by multiplication by a constant factor of four [26]. The

simulation system was coupled to a constant temperature bath using the 'V-rescale' algorithm with a relaxation time of 1.0 ps. The time step used in the simulation was 20 fs. The dielectric constant in the simulations was $\epsilon_r = 15$. The neighbour-list was updated every 10 simulation steps. The pressure was isotropically coupled to 1 bar (Berendsen pressure coupling) with a relaxation time of 1.0 ps. A shifted cutoff of 1.2 nm was used for both Coulomb and Lennard-Jones (LJ) interactions. Interactions were gradually scaled to zero beyond 0 nm (Coulomb) and 1.0 nm (LJ) respectively.

The replica exchange simulations were performed using GROMACS version 4.5.7. The replica exchange frequency was 2 ps. In the solvent free replica exchange simulations a Langevin thermostat was used with a friction coefficient of 0.25 ps^{-1}. All solvent free simulations were performed in the *NVT* ensemble. Further details on the simulation setups and settings can be found in the *SI*.

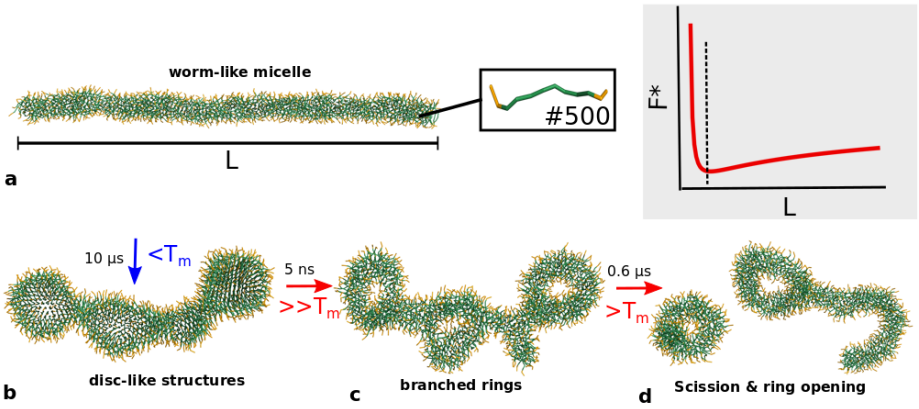

Figure 3.1: Temperature induced formation of lipid toroidal micelles. (a) A worm-like micelle faces a kinetic barrier against ring formation via self-folding and fusion of the two free end caps ($F*$) that increases with growing length L. (b) Cooling of a fluid worm-like micelle below T_m (273 K) results in the formation of a fibril consisting of disc-like structures. (c,d) A short subsequent heat shock (400 K for 5 ns) induces a sudden disc to torus transition. The formed branched toroidal structure is subsequently simulated at 360 K for 600 ns of simulated time. The unstable junctions between the toroidal micelles result in scission and 'ring opening'. The lipid surfactant in this example features two hydrophilic phosphatidylcholine headgroups (colored orange) connected to the ends of a hydrophobic chain (colored green) with a chain melting temperature, $T_m \simeq 295$ K.

3.3 Results

3.3.1 Thermo-responsive formation of isolated toroidal micelles

In a first step, we study the effect of cooling a pre-constructed worm-like micelle consisting of 500 surfactant molecules below the phase transition temperature T_m. The MARTINI model is able to qualitatively describe the fluid-gel phase transition in lipid membranes [35, 36]. Figure 3.1b illustrates that transition toward the gel phase enforces the formation of disc-like structures, which are especially pronounced at the two free ends of the worm-like micelle. We will study these structures in closer detail in a later section. Motivated by an earlier hypothesis on the origin of toroidal micelles [8], we investigate whether these disc-like structures have a propensity to transit into toroidal micelles upon an external stimulus. To this aim, we apply a short 5 ns heat shock ($>> T_m$). Indeed, heat shocking enforces a rapid transition into branched toroidal micelles (Fig. 3.1b). However, these branched toroidal micelles subsequently split off into forming separate, isolated ‘rings’ after simulation at a lower temperature (360 K). Interestingly, these observations indicate that a lipid connection between the formed ‘rings’ – a four-branch or four-junction – is evidently not thermodynamically stable (Fig. 3.1d). This behavior stands quite in contrast with the behavior of polymeric surfactants observed in experiments [8, 37] and mesoscopic simulations [38, 39] as well as the behavior observed for ionic surfactants in molecular simulations [21]. Furthermore, we observe that a formed four-junction can alternatively escape into a three-junction via ‘opening’ of one ring [40], Fig. 3.1d. We extensively study these scission mechanisms and their relative probabilities of occurrence in close detail in Fig. 3.5.

In a following step, we study the disc-to-torus transition in close detail by performing extensive temperature replica exchange (T-REM) simulations of a smaller aggregate (144 molecules) over a temperature ladder ranging from 280 K to 450 K. The size of this aggregate corresponds to the size of the isolated toroidal micelles formed in Fig. 3.1. Replica exchange simulations allow for an extensive sampling of structure space. We conduct these simulations both in implicit and explicit solvent conditions [26, 41]. The obtained temperature versus enthalpy curve suggests a phase transition temperature T_m of about 330 K for the implicit solvent model and 295 K for the explicit solvent model (see Fig. 3.6 and 3.7). Indeed, disc-like micelles are formed below T_m, see Fig. 3.2a. The central region of such a disc-like micelle is comprised of hexagonal close-packed lipid tails whereas its edge consists of a belt of intertwined surfactants thereby effectively shielding its hydrophobic edge (Fig. 3.2a). In fact, this

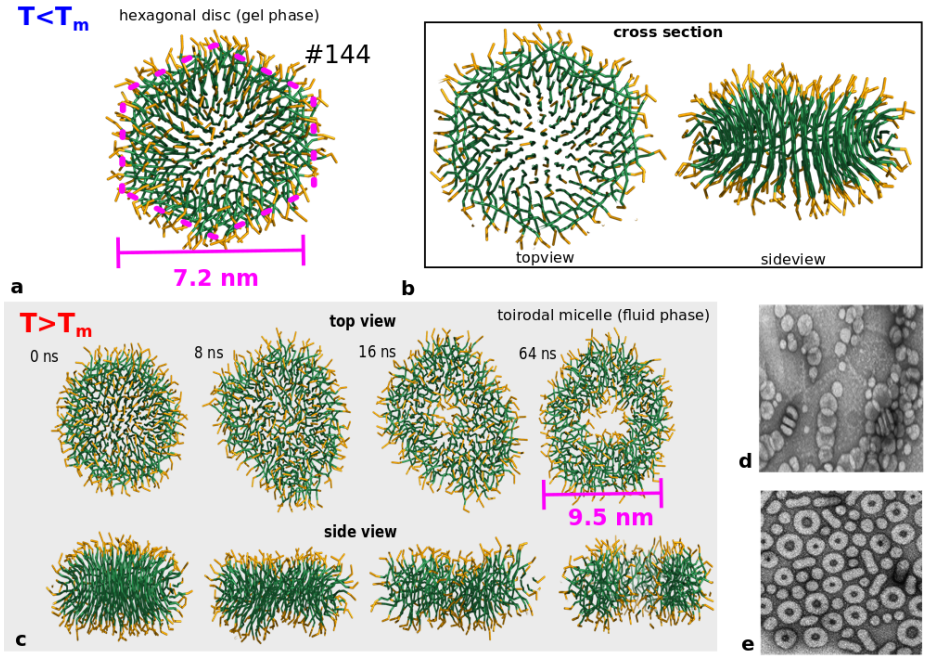

Figure 3.2: Disc-like and toroidal micelles. (a) Example of a hexagonal disc formed within the molecular dynamics simulations below T_m. (b) The edge of the disc consists of a belt of intertwined surfactants (top view). Note that the surfactants adopt a bent conformation close to the disc's edge (side view). (c) Heating a disc in the gel phase up to 360 K induces a rapid transition toward a toroidal micelle. (d,e) Transmission electron microscopy (TEM) imaging of discs (d) and toroidal micelles (e) formed in ABC tri-block copolymer solutions (Adapted from Cui et al. [8]).

observed structure somewhat resembles the proposed structure of a "hockey puck" micelle [42]. A closer look at the disc's overall structure reveals that such a disc is not circular but rather hexagonally shaped, see Fig. 3.2a. This can be explained by realization of a low energy configuration, i.e. a hexagonal packing, upon gelation. The cross-sectional side view of the disc reveals that the surfactants adopt a strongly bent conformation near the edge of the disc, see Fig. 3.2b. Since such a bent configuration reduces the unfavorable hydrophobic surface of the disc's edge, we hypothesize that a remaining degree of chain flexibility below T_m may be essential for disc formation. Indeed, increasing the chain stiffness of the surfactant's hydrophobic mid part (shown in green color), i.e. modeling this part as a stiff rod, effectively impairs disc formation in our simulations and rather results into an alternative helical fibril structure, in agreement with previous

grid-based Monte Carlo simulations [43, 44] (see Fig. 3.8). Finally, it is important to emphasize that the surfactant's special architecture, i.e. the bolaform, is crucial for disc stability. For sake of illustration, we performed simulations of a stable pre-formed disc at 275 K where we 'sliced' the bola surfactants in half through the center of their hydrophobic tail region, thereby yielding two regular lipid surfactants (see Fig. 3.9). Consequently, the disc rapidly loses its structural integrity and morphs into a regular worm-like micelle despite conservation of the overall hydrophobic and hydrophilic volume fraction. This clearly indicates that 'bolafication' is essential for the disc's stability. To this end, we emphasize that rationalisation of the disc's free energy and concomitant stability by elastic models (e.g. [45]) is not straightforward due to the crystalline nature of the disc in the gel phase.

Above T_{m}, the structural space is dominated by toroidal micelles. Exploring the formation of toroidal micelles in detail reveals that toroidal micelles indeed result from spontaneous 'perforation' of disc-like micelles above T_{m}, see Fig. 3.2c. Therefore, our simulations support the hypothesis that toroidal micelles in ABC triblock copolymer systems directly originate from the perforation of preceding disc-like micelles upon an external stimulus (e.g., change in solvent conditions)[8], see Fig. 3.2d,e. Our simulations suggest the following mechanism: Upon melting the disc loses structural integrity. Elongation of the disc into a worm-like micelle would increase the interfacial length of the disc's unfavorable edge. Therefore, the circular shape of the disc remains rather conserved upon melting. Since the disc's edge is relatively hydrophobic, it tends to shield itself from the water phase by 'escaping' into a toroidal micelle. Worm-like micelles are rarely observed in the high temperature regime. These worm-like micelles do not result from 'ring opening' but rather from the formation of propeller-shaped micelles consisting of two smaller discs slightly above T_{m} (see Fig. 3.6). These discs are seemingly too small to allow a perforation mechanism into a toroidal micelle. Thus, melting of a disc-like micelle proceeds via different competitive kinetic pathways. Toroidal micelles are formed if the disc-to-torus transition proceeds at a faster rate – a kinetic trap. Here, a well-defined overall circular disc shape likely enforces formation of a toroidal micelle. Therefore, the more circular disc-like structures formed at the ends of the frozen worm-like micelle are expected to have an increased propensity to transit into toroidal micelles, see Fig. 3.1b.

3.3.2 Kinetic stability of the formed toroidal micelle

Opening of the torus is characterized by a scission event and is associated with the formation of two free hemispherical end caps. To this end, we calculated the free energy barrier against scission using a state-of-the-art density-field based string

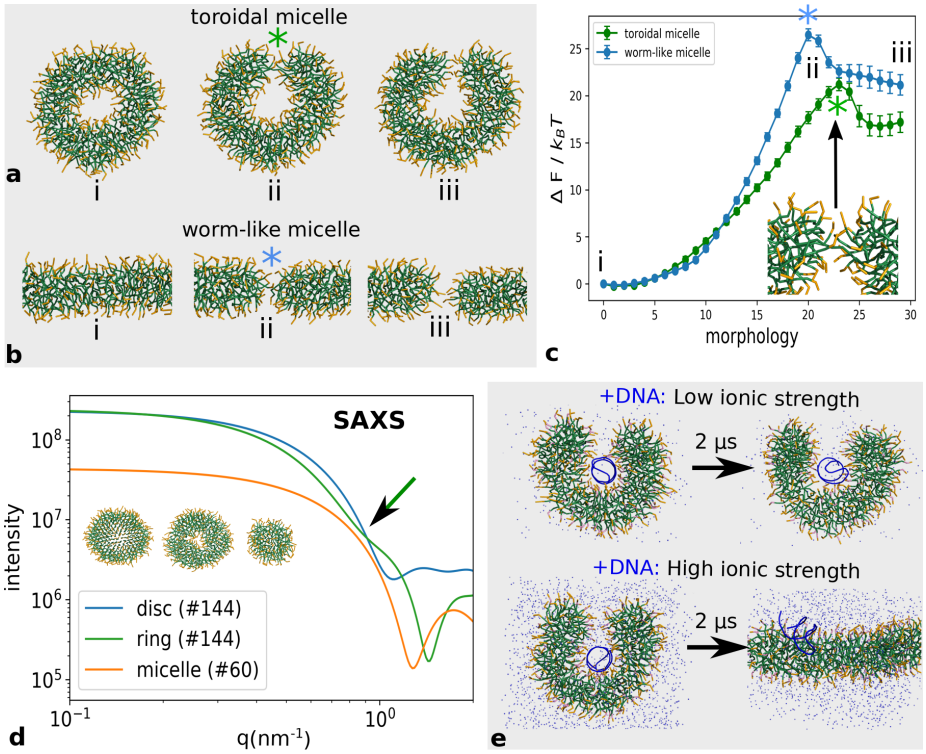

Figure 3.3: Free energy barrier against scission. (a,b) Resolved reaction pathway of ring opening (a) and scission of a worm-like micelle (b): (i) The reactant state, (ii) the intermediate corresponding to the resolved free energy barrier, (iii) the product state. (c) Free energy along the resolved scission pathway. (d) X-ray spectrum resolved [46, 47] for a disc-like micelle in the gel phase ($< T_m$), a toroidal micelle, and a micelle consisting of 60 surfactants only. The toroidal micelle is characterized by a pronounced 'buckle' at around 1 nm^{-1} (green arrow). (e) Uptake of a 12-base pair polyelectrolyte (a DNA fragment) by an open micelle (#144) comprised of 50 % cationic and 50 % zwitterionic lipid surfactants at low ionic strength (0.1 M NaCl) and high ionic strength (1 M NaCl).

method [34]. This method resolves a thermodynamically reversible reaction pathway of minimal free energy, i.e. the most likely pathway, to transit from a reactant into the product state, in our example being a (i) toroidal micelle, and (ii) an open toroidal micelle respectively (see *SI* for further details).

The resolved pathway of minimal free energy is illustrated in Fig. 3.3. Notably, the observed scission mechanism is similar – but in a reverse direction – to the observed mechanism of forming the first fusion intermediate in biological membrane fusion [34]. The structure associated with the free energy barrier

features a single lipid which connects the two formed free ends. Fig. 3.3 illustrates a scission barrier of 21 $k_{\mathrm{B}}T$ for a toroidal micelle (144 molecules). The rate of scission k is given by, $k = Ae^{\frac{\Delta F^*}{k_{\mathrm{B}}T}}$, with A being the kinetic prefactor. Therefore, the average life-time τ of a toroidal micelle is $\tau = 1/k$. The scission and fusion rates of hemifusion intermediates in lipid membranes, which are closely related to the scission and fusion of micelles, have been determined from coarse-grained simulations using Markov state modeling (see *SI* in Ref. [48]). From this study we can obtain an estimation of the kinetic prefactor A, being about $10^{-10}s^{-1}$. This estimate includes a factor of $1/4$ to correct for the four times faster diffusion of the used coarse-grained model [26]. In such case, within the accuracy of coarse-grained models, the corresponding average lifetime of a toroidal micelle would be 0.13 s. Our main finding, however, is that the scission barrier of the highly curved toroidal micelle and worm-like micelle remain rather similar (21 versus 26 $k_{\mathrm{B}}T$). This implies that ‘ring opening’ and subsequent fractionation of the corresponding worm-like micelle are expected to occur on a rather similar time-scale. For worm-like micelles formed by small (ionic) surfactants, characteristic breaking times are of the order of milliseconds as being determined by rheological experiments [49], but may extend up to seconds or minutes for lecithin worm-like micelles at equilibrium [50]. Since time-resolved X-ray scattering experiments enable a time resolution of only a few milliseconds [51] detection of toroidal micelles with these techniques must be possible even with the toroidal micelles being highly transient in nature. In particular, since toroidal micelles leave a pronounced fingerprint within X-ray and SANS spectra (see Fig. 3.3d and Fig. 3.10).

3.4 Discussion

Previous SANS experiments suggested that zwitterionic lipid bolaamphiphiles are restricted to form small non-spherical micelles above T_{m} in solution, while forming worm-like fibrils of microscopic sizes below T_{m} [52]. However, it is important to emphasize that the estimated free energy of the two end caps, being $\simeq 20\, k_{\mathrm{B}}T$, is subject to the condition that the two end caps are kept in a close proximity to each other thereby making the reverse fusion reaction likely [34]. In contrast, the size distribution of worm-like micelles in solution is the outcome of a balance between the effective fusion and scission rate *free in solution* [21, 53–59]. Free in solution, zwitterionic micelles are additionally subject to strong hydration repulsion which opposes close proximity and thereby hinders rapid coalescence of micelles via consecutive fusion events. Hence, the end cap free energy and concomitant scission barrier derived in molecular simulations via free energy calculations (e.g., citations [60, 61]) rather reflects an *intrinsic* free energy which may not trivially translate into the expected size distribution free in

solution.

Fluid worm-like micelles are often formed by ionic surfactants under high ionic strength [49, 51]. Under this condition micelles become attractive [51]. Consequently, the rate of fusion becomes substantially larger than the rate of scission. This enables growth of worm-like micelles up to a size of micrometers. For zwitterionic surfactants at a low concentration, the characteristic time of micelle fusion (the inverse fusion rate) may in fact be smaller than the characteristic breaking time (the inverse scission rate) of a worm-like micelle, despite a positive intrinsic free energy of its free end caps. Thus, zwitterionic surfactants may require a much larger hydrophobic tail to form fluid worm-like micelles than ionic surfactants at high ionic strength because the concomitant decrease in fusion rate must be compensated by a larger breaking time [62]. In contrast, below the chain melting temperature T_m, the characteristic breaking time becomes extremely large (up to days [62]) explaining the stability of lipid worm-like micelles or fibrils in the gel phase [29, 62]. It is noteworthy that a large kinetic free energy barrier against fusion is also a key reason for biological membrane fusion requiring the presence of fusion proteins to actively bring the membranes in close proximity, despite the fact that fusion of vesicles is thermodynamically highly favorable [63]. The size distribution that worm-like micelles adopt in solution is determined by both the excess free energy of the end caps, which is largely dictated by the effective packing shape of constituent surfactants [64], and the effective free energy barrier against micelle coalescence, which is dictated by hydration repulsion [51]. Finally, the kinetics and rate of fusion will be significantly faster if fusion is facilitated by 'branching' and subsequent sliding of worm-like micelles rather than solely end-to-end fusion [50].

3.4.1 Size matters

It is important to emphasize that the overall shape of the open torus at the scission barrier is very similar to that of the closed torus (see Fig. 3.3a). This suggests that the scission barrier mainly depends on the elastic energy associated with the formation of the two hemispherical free end caps, since the excess bending free energy of the torus itself is largely conserved. This directly explains why both the barrier against ring opening and the scission barrier of the corresponding worm-like micelle are of similar magnitude (see Fig. 3.3c). In a highly curved polymeric toroidal micelle, the diameter of both the torus and its constituent tube will be about tenfold larger [9]. Consequently, the constituent tube of the torus increases in stiffness. This increases the concomitant elastic energy associated with forming the two hemispherical free end caps when undergoing scission. We argue that the scission barrier likely scales by a factor of 10^3 with increasing

length-scale (see SI for a detailed explanation). Polymeric toroidal micelles are thus highly metastable due to their tenfold larger scale (see *SI* for further details).

Lipid liposomes or vesicles, in contrast to lipid toroidal micelles, will self-heal after spontaneous poration. The closing of the pore is enforced by a force at the interface of a formed pore (a line tension). Thus, liposomal formulations can have a shelf life of months or perhaps even years despite the fact that spontaneous membrane pore formation faces a free energy barrier of *only* several tens of $k_{\mathrm{B}}T$ [65]. Even if a toroidal micelle is thermodynamically stable, i.e. the free energy of the two end caps is larger than the bending energy of the torus, ring opening does not yield a restoring force that would promote closing of the torus. Self-healing would thus require the introduction of an additional driving force that opposes unbending of the open torus.

Interestingly, our simulations suggest that incorporation of a 12-base pair polyelectrolyte – a DNA fragment – within the central cavity of an open toroidal micelle comprised of 50 % cationic and 50 % zwitterionic lipid surfactants counteracts the release of bending energy at low ionic strength (0.1 M NaCl), see Fig. 3.3e. The uptake and incorporation of such a DNA fragment is driven by a gain in the electric potential energy when residing within the central cavity of the torus (see Fig. 3.11). In contrast, high ionic strength (1 M NaCl) enables complete opening of the toroidal micelle because of electrostatic screening and concomitant stiffening of the micelle [66]. This observation is analogous to DNA's well-known ability to stabilize inverted hexagonal phases in stacked positively net charged membrane systems [67]. In contrast, at high ionic strength, the electrostatic screening is too strong and the torus completely opens (see Fig. 3.3e). Notably, the open ring is metastable even if its bending free energy is compensated (see Fig. 3.3b) since closing of the ring faces a small free energy barrier against the combination of the two end caps (see Fig. 3.3a). However, DNA-mediated stabilization of ‘nano rings’ requires that: (i) The toroidal micelle can exist below the denaturation temperature of DNA, (ii) the formed DNA-micelle complex must be kinetically or thermodynamically restricted from forming alternative phases such as, for example, hexagonally stacked rods or micelles. It is uncertain whether such a phase regime is experimentally accessible.

3.5 Conclusions

We illustrated how a thermo-responsive lipid surfactant can be kinetically tricked into forming highly curved toroidal structures. Our free energy calculations illustrate that the scission barrier of toroidal micelles, despite being under a high curvature stress, is in fact rather similar to that of worm-like micelles.

Consequently, the lifetime of a highly curved toroidal micelle is similar to the breaking time of its corresponding micelle at equilibrium. Our work provides a unique molecular glance into the complex kinetics of stimuli-responsive self-aggregation on a nano scale. Despite seemingly similar kinetics of structure formation on different length scales, scale dependent differences in the life-time of formed phases can arise when the phases are kinetically rather than thermodynamically stable. Consequently, lipid 'nano rings' have a lifetime of likely milliseconds to seconds, quite in contrast to the highly metastable toroidal micelles formed by block copolymers. This explains the paradoxical absence of toroidal micelle phases at a tenfold smaller length scale.

We now consider it plausible that lipid 'nano rings' have already been fabricated within experiments but have thus far escaped experimental detection. We therefore advocate experimental revisiting of previously studied thermo-responsive lipid bola amphiphile systems (e.g, citations [30, 52]) with state-of-the-art time-resolved X-ray scattering techniques (e.g, citation [51]). Of related interest is the observed thermodynamic preference of lipid bola amphiphiles to form disc-like structures below T_{m}. The presence of disc-like structures may very well explain the regular thickness undulations observed in AFM experiments in fibrils formed by lipid bola amphiphiles below T_{m} [43]. Isolated lipid discs could alternatively precipitate from solution and form fibrils via repetitive stacking of discs analogous to their observed behavior in block copolymer mixtures [8]. Repetitive stacking of slightly tilted discs may explain the observation of fibrils with a somewhat helical appearance as has been observed in transmission electron microscopy of hydrogels formed by lipid bola amphiphiles [30, 68]. Fitting high-resolution SANS and SAXS sprectra of these fibril structures with alternative models based on disc structures in either a 'chained' (see Fig. 3.1A) or stacked conformation may yield novel insights into the packing and self-organization of lipid Pluronic analogs below T_{m}.

Finally, the stability and lifetime of 'nano rings' could be increased by introducing a restoring force which opposes unbending of the torus. Incorporation of a short double-stranded DNA fragment or another poly-electrolyte within the torus can compensate the unfavorable bending energy stored within a positively net charged toroidal micelle at low ionic strength. Because of their versatile self-organization, bolaamphiphiles have already illustrated a great potential in the field of drug delivery [28]. Lipid 'Nano rings' stabilized by DNA fragments may have interesting applications in, for example, gene delivery technologies [5, 69]. Their small size ($\simeq 10\,\mathrm{nm}$) as well as their responsive nature upon external stimuli such as, for example, temperature and ionic strength may be advantageous for the transfection of small DNA fragments in cells.

Acknowledgements. The authors would like to thank Alfred Blume, Simon Drescher, Bernd Abel and Marcus Müller for fruitfull discussion. HJR acknowledges the Life@nano excellence initiative (state of Lower Saxony) and the NWO Vidi scheme for funding. The HLRN Berlin/Hannover & NWO SURFsara (the netherlands) are acknowledged for computational resources.

References

[1] Svenson, S. “Controlling surfactant self-assembly”. In: *Curr. Opin. Colloid & Interface Sci.* Vol. 9, no. 3-4 (Nov. 2004), pp. 201–212.

[2] Branco, M. C. and Schneider, J. P. “Self-assembling materials for therapeutic delivery”. In: *Acta Biomater.* Vol. 5, no. 3 (Mar. 2009), pp. 817–831.

[3] Blanazs, A., Armes, S. P., and Ryan, A. J. “Self-Assembled Block Copolymer Aggregates: From Micelles to Vesicles and their Biological Applications”. In: *Macromol. Rapid Commun.* Vol. 30, no. 4-5 (Feb. 2009), pp. 267–277.

[4] Garti, N., Somasundaran, P., and Mezzenga, R., eds. *Self-Assembled Supramolecular Architectures*. John Wiley & Sons, Inc., Sept. 2012.

[5] Fong, W.-K. et al. “Responsive self-assembled nanostructured lipid systems for drug delivery and diagnostics”. In: *J. Colloid Interface Sci.* Vol. 484 (Dec. 2016), pp. 320–339.

[6] Sheth, T. et al. “Multiple nanoemulsions”. In: *Nat. Rev. Mat.* Vol. 5, no. 3 (Jan. 2020), pp. 214–228.

[7] Pochan, D. J. “Toroidal Triblock Copolymer Assemblies”. In: *Science* vol. 306, no. 5693 (Oct. 2004), pp. 94–97.

[8] Cui, H. et al. “Origins of toroidal micelle formation through charged triblock copolymer self-assembly”. In: *Soft Matter* vol. 5, no. 6 (2009), pp. 1269–1278.

[9] Huang, H. et al. “Toroidal Micelles of Uniform Size from Diblock Copolymers”. In: *Angew. Chem. Int. Ed.* Vol. 48, no. 25 (June 2009), pp. 4594–4597.

[10] Liu, C. et al. “Toroidal Micelles of Polystyrene-block-Poly(acrylic acid)”. In: *Small* vol. 7, no. 19 (Aug. 2011), pp. 2721–2726.

[11] Chen, L. et al. “Toroid Formation through Self-Assembly of Graft Copolymer and Homopolymer Mixtures: Experimental Studies and Dissipative Particle Dynamics Simulations”. In: *Langmuir* vol. 29, no. 26 (June 2013), pp. 8417–8426.

[12] Ni, B. et al. “Pathway toward Large Two-Dimensional Hexagonally Patterned Colloidal Nanosheets in Solution”. In: *J. Am. Chem. Soc.* Vol. 137, no. 4 (Jan. 2015), pp. 1392–1395.

[13] Presa-Soto, D. et al. “Formation and Reversible Morphological Transition of Bicontinuous Nanospheres and Toroidal Micelles by the Self-Assembly of a Crystalline-b-Coil Diblock Copolymer”. In: *Angewandte Chem. Int. Ed.* Vol. 55, no. 34 (July 2016), pp. 10102–10107.

[14] Luo, H., Santos, J. L., and Herrera-Alonso, M. “Toroidal structures from brush amphiphiles”. In: *Chem. Commun.* Vol. 50 (5 2014), pp. 536–538.

[15] Bergström, L. M. “Thermodynamics and bending energetics of toruslike micelles”. In: *J. Colloid Interface Sci.* Vol. 327, no. 1 (Nov. 2008), pp. 191–197.

[16] Lauw, Y., Leermakers, F. A. M., and Stuart, M. A. C. “Self-Consistent-Field Prediction for the Persistence Length of Wormlike Micelles of Nonionic Surfactants”. In: *J. Phys. Chem. B* vol. 107, no. 39 (Oct. 2003), pp. 10912–10918.

[17] Asgari, M. *Elastic free-energy of wormlike micellar chains: theory and suggested experiments*. 2015. arXiv: 1502.02338 [cond-mat.soft].

[18] Mukerjee, P. “Size distribution of small and large micelles. Multiple equilibrium analysis”. In: *J. Phys. Chem.* Vol. 76, no. 4 (Feb. 1972), pp. 565–570.

[19] Israelachvilli, J. *Intermolecular and Surface Forces*. Elsevier, 2011.

[20] Porte, G. “Giant micelles in ideal solutions. Either rods or vesicles”. In: *J. Phys Chem.* Vol. 87, no. 18 (Sept. 1983), pp. 3541–3550.

[21] Dhakal, S. and Sureshkumar, R. “Topology, length scales, and energetics of surfactant micelles”. In: *J. Chem. Phys.* Vol. 143, no. 2 (July 2015), p. 024905.

[22] He, X. and Schmid, F. “Spontaneous Formation of Complex Micelles from a Homogeneous Solution”. In: *Phys. Rev. Lett.* Vol. 100 (13 Apr. 2008), p. 137802.

[23] He, P. et al. “Complex micelles from the self-assembly of coil-rod-coil amphiphilic triblock copolymers in selective solvents”. In: *Soft Matter* vol. 6, no. 7 (2010), p. 1539.

[24] Taddese, T. et al. “Recent advances in particle-based simulation of surfactants”. In: *Curr. Opin. Colloid Interface Sci.* Vol. 48 (Aug. 2020), pp. 137–148.

[25] Pronk, S. et al. “GROMACS 4.5: a high-throughput and highly parallel open source molecular simulation toolkit”. In: *Bioinformatics* vol. 29, no. 7 (Feb. 2013), pp. 845–854.

[26] Marrink, S. J. et al. “The MARTINI Force Field: Coarse Grained Model for Biomolecular Simulations”. In: *J. Phys. Chem. B* vol. 111, no. 27 (July 2007), pp. 7812–7824.

[27] Fuhrhop, J.-H. and Wang, T. “Bolaamphiphiles”. In: *Chem. Rev.* Vol. 104, no. 6 (June 2004), pp. 2901–2938.

[28] Fariya, M. et al. “Bolaamphiphiles: A Pharmaceutical Review”. eng. In: *Adv. Pharm. Bull.; eISSN 2251-7308* (2014).

[29] Blume, A. et al. “Self-assembly of different single-chain bolaphospholipids and their miscibility with phospholipids or classical amphiphiles”. In: *Adv. Colloid Interface Sci.* Vol. 208 (June 2014), pp. 264–278.

[30] Köhler, K. et al. “Self-Assembly in a Bipolar Phosphocholine–Water System: The Formation of Nanofibers and Hydrogels”. In: *Angewandte Chemie International Edition* vol. 43, no. 2 (Jan. 2004), pp. 245–247.

[31] Mortensen, K. and Pedersen, J. S. “Structural study on the micelle formation of poly(ethylene oxide)-poly(propylene oxide)-poly(ethylene oxide) triblock copolymer in aqueous solution”. In: *Macromolecules* vol. 26, no. 4 (July 1993), pp. 805–812.

[32] Mortensen, K. “Structural studies of aqueous solutions of PEO-PPO-EO triblock copolymers, their micellar aggregates and mesophases; a small-angle neutron scattering study”. In: *J. Phys.: Condens. Matter* vol. 8, no. 25 (July 1996), A103–A124.

[33] Tian, Q. et al. “Stimuli-responsive polymer wormlike micelles”. In: *Prog. Polym. Sci* vol. 89 (Feb. 2019), pp. 108–132.

[34] Smirnova, Y. G., Risselada, H. J., and Müller, M. “Thermodynamically reversible paths of the first fusion intermediate reveal an important role for membrane anchors of fusion proteins”. In: *Proc. Natl. Acad. Sci. USA* vol. 116, no. 7 (Jan. 2019), pp. 2571–2576.

[35] Marrink, S. J., Risselada, J., and Mark, A. E. “Simulation of gel phase formation and melting in lipid bilayers using a coarse grained model”. In: *Chem. Phys. Lipids* vol. 135, no. 2 (June 2005), pp. 223–244.

[36] Risselada, H. J. and Marrink, S. J. “The freezing process of small lipid vesicles at molecular resolution”. In: *Soft Matter* vol. 5, no. 22 (2009), p. 4531.

[37] Förster, S. et al. “Fusion of Charged Block Copolymer Micelles into Toroid Networks”. In: *J. Phys. Chem. B* vol. 103, no. 32 (Aug. 1999), pp. 6657–6668.

[38] Fraaije, J. G. E. M. and Sevink, G. J. A. “Model for Pattern Formation in Polymer Surfactant Nanodroplets”. In: *Macromolecules* vol. 36, no. 21 (Oct. 2003), pp. 7891–7893.

[39] Sevink, G. J. A. and Zvelindovsky, A. V. “Self-Assembly of Complex Vesicles”. In: *Macromolecules* vol. 38, no. 17 (Aug. 2005), pp. 7502–7513.

[40] May, S., Bohbot, Y., and Ben-Shaul, A. “Molecular Theory of Bending Elasticity and Branching of Cylindrical Micelles”. In: *J. Phys. Chem. B* vol. 101, no. 43 (Oct. 1997), pp. 8648–8657.

[41] Arnarez, C. et al. “Dry Martini, a Coarse-Grained Force Field for Lipid Membrane Simulations with Implicit Solvent”. In: *J. Chem. Theory Comput.* Vol. 11, no. 1 (Dec. 2014), pp. 260–275.

[42] Williams, D. R. M. and Fredrickson, G. H. “Cylindrical micelles in rigid-flexible diblock copolymers”. In: *Macromolecules* vol. 25, no. 13 (June 1992), pp. 3561–3568.

[43] Meister, A. et al. “Helical Nanofibers of Self-Assembled Bipolar Phospholipids as Template for Gold Nanoparticles”. In: *J. Phys. Chem. B* vol. 112, no. 15 (Apr. 2008), pp. 4506–4511.

[44] Wahab, M. et al. “Monte Carlo Study of the Self-Assembly of Achiral Bolaform Amphiphiles into Helical Nanofibers”. In: *Langmuir* vol. 26, no. 5 (Mar. 2010), pp. 2979–2982.

[45] Bergström, L. M. “Bending Energetics of Tablet-Shaped Micelles: A Novel Approach to Rationalize Micellar Systems”. In: *ChemPhysChem* vol. 8, no. 3 (Feb. 2007), pp. 462–472.

[46] Svergun, D., Barberato, C., and Koch, M. H. J. “CRYSOL– a Program to Evaluate X-ray Solution Scattering of Biological Macromolecules from Atomic Coordinates”. In: *J. Appl. Cryst.* Vol. 28, no. 6 (Dec. 1995), pp. 768–773.

[47] Svergun, D. I. et al. “Protein hydration in solution: Experimental observation by x-ray and neutron scattering”. In: *Proc. Natl. Acad. Sci. USA* vol. 95, no. 5 (Mar. 1998), pp. 2267–2272.

[48] Kasson, P. M. et al. “Ensemble molecular dynamics yields submillisecond kinetics and intermediates of membrane fusion”. In: *Proc. Natl. Acad. Sci. U.S.A* vol. 103, no. 32 (July 2006), pp. 11916–11921.

[49] Dreiss, C. A. “Wormlike micelles: where do we stand? Recent developments, linear rheology and scattering techniques”. In: *Soft Matter* vol. 3, no. 8 (2007), p. 956.

[50] Olsson, U. et al. “Slow dynamics of wormlike micelles”. In: *Soft Matter* vol. 6, no. 8 (2010), p. 1769.

[51] Jensen, G. V. et al. “Monitoring the Transition from Spherical to Polymer-like Surfactant Micelles Using Small-Angle X-Ray Scattering”. In: *Angew. Chem. Int. Ed.* Vol. 53, no. 43 (Sept. 2014), pp. 11524–11528.

[52] Meister, A. et al. “Structure-Property Relationship in Stimulus-Responsive Bolaamphiphile Hydrogels”. In: *Langmuir* vol. 23, no. 14 (July 2007), pp. 7715–7723.

[53] MacKintosh, F. C, Safran, S. A, and Pincus, P. A. “Self-Assembly of Linear Aggregates: the Effect of Electrostatics on Growth”. In: *Europhys. Lett. (EPL)* vol. 12, no. 8 (Aug. 1990), pp. 697–702.

[54] Duyndam, A. and Odijk, T. “Viscosity of Wormlike Micelles: Determination of the End Cap Energy and Persistence Length”. In: *Langmuir* vol. 12, no. 20 (Jan. 1996), pp. 4718–4722.

[55] Berret, J.-F. “Rheology of Wormlike Micelles: Equilibrium Properties and Shear Banding Transitions”. In: *Molecular Gels*. Springer-Verlag, 2006, pp. 667–720.

[56] May, S. and Ben-Shaul, A. “Molecular Theory of the Sphere-to-Rod Transition and the Second CMC in Aqueous Micellar Solutions”. In: *J. Phys. Chem. B* vol. 105, no. 3 (Jan. 2001), pp. 630–640.

[57] Couillet, I. et al. “Growth and Scission Energy of Wormlike Micelles Formed by A Cationic Surfactant with Long Unsaturated Tails”. In: *Langmuir* vol. 20, no. 22 (Oct. 2004), pp. 9541–9550.

[58] Helgeson, M. E. et al. “A systematic study of equilibrium structure, thermodynamics, and rheology of aqueous CTAB/NaNO3 wormlike micelles”. In: *J. Colloid Interface Sci* vol. 349, no. 1 (Sept. 2010), pp. 1–12.

[59] Danov, K. D. et al. “Growth of wormlike micelles in nonionic surfactant solutions: Quantitative theory vs. experiment”. In: *Adv. Colloid Interface Sci* vol. 256 (June 2018), pp. 1–22.

[60] Vogtt, K. et al. “Free Energy of Scission for Sodium Laureth-1-Sulfate Wormlike Micelles”. In: *Langmuir* vol. 33, no. 8 (Feb. 2017), pp. 1872–1880.

[61] Wand, C. R. et al. “The Relationship between Wormlike Micelle Scission Free Energy and Micellar Composition: The Case of Sodium Lauryl Ether Sulfate and Cocamidopropyl Betaine”. In: *Langmuir* (Oct. 2020).

[62] Kumar, R. et al. “Wormlike Micelles of a C22-Tailed Zwitterionic Betaine Surfactant: From Viscoelastic Solutions to Elastic Gels”. In: *Langmuir* vol. 23, no. 26 (Dec. 2007), pp. 12849–12856.

[63] François-Martin, C., Rothman, J. E., and Pincet, F. “Low energy cost for optimal speed and control of membrane fusion”. In: *Proc. Natl Acad. Sci. U.S.A* vol. 114, no. 6 (Jan. 2017), pp. 1238–1241.

[64] Israelachvili, J. N., Mitchell, D. J., and Ninham, B. W. “Theory of self-assembly of hydrocarbon amphiphiles into micelles and bilayers”. In: *J. Chem. Soc., Faraday Trans. 2* vol. 72 (1976), p. 1525.

[65] Ting, C. L. et al. “Metastable Prepores in Tension-Free Lipid Bilayers”. In: *Phys. Rev. Lett.* Vol. 120 (12 Mar. 2018), p. 128103.

[66] Mandal, T. and Larson, R. G. “Stretch and Breakage of Wormlike Micelles under Uniaxial Strain: A Simulation Study and Comparison with Experimental Results”. In: *Langmuir* vol. 34, no. 42 (Sept. 2018), pp. 12600–12608.

[67] Koltover, I. “An Inverted Hexagonal Phase of Cationic Liposome-DNA Complexes Related to DNA Release and Delivery”. In: *Science* vol. 281, no. 5373 (July 1998), pp. 78–81.

[68] Köhler, K. et al. “Temperature-Dependent Behavior of a Symmetric Long-Chain Bolaamphiphile with Phosphocholine Headgroups in Water: From Hydrogel to Nanoparticles”. In: *J. Am. Chem. Soc.* Vol. 126, no. 51 (Dec. 2004), pp. 16804–16813.

[69] Balazs, D. A. and Godbey, W. “Liposomes for Use in Gene Delivery”. In: *J. Drug Deliv.* Vol. 2011 (2011), pp. 1–12.

[70] Corsi, J. et al. “DNA Lipoplexes: Formation of the Inverse Hexagonal Phase Observed by Coarse-Grained Molecular Dynamics Simulation”. In: *Langmuir* vol. 26, no. 14 (July 2010), pp. 12119–12125.

[71] Wassenaar, T. A. et al. “Going Backward: A Flexible Geometric Approach to Reverse Transformation from Coarse Grained to Atomistic Models”. In: *J. Chem. Theory Comput.* Vol. 10, no. 2 (Jan. 2014), pp. 676–690.

[72] Weinan, E, Ren, W., and Vanden-Eijnden, E. “Simplified and improved string method for computing the minimum energy paths in barrier-crossing events”. In: *J. Chem. Phys.* Vol. 126, no. 16 (2007), p. 164103.

[73] Smirnova, Y. G., Risselada, H. J., and Müller, M. “Thermodynamically reversible paths of the first fusion intermediate reveal an important role for membrane anchors of fusion proteins”. In: *Proc. Natl. Acad. Sci. U.S.A* vol. 116, no. 7 (2019), pp. 2571–2576.

[74] Müller, M. et al. “Transition Path from Two Apposed Membranes to a Stalk Obtained by a Combination of Particle Simulations and String Method”. In: *Phys. Rev. Lett.* Vol. 108 (22 May 2012), p. 228103.

[75] Smirnova, Y. and Müller, M. “Calculation of membrane bending rigidity using field-theoretic umbrella sampling”. In: *J. Chem. Phys.* Vol. 143, no. 24 (2015), p. 243155.

[76] Gennes, P.-G. de. *Scaling Concepts in Polymer Physics*. New York: Cornell University, 1979.

[77] Rubinstein, M. and Colby, R. H. *Polymer Physics*. OUP Oxford (New York, London), 2003.

[78] Khokhlov, A. R., Grosberg, A. Y., and Pande, V. S. *Statistical Physics of Macromolecules*. AIP-Press, 1994.

[79] Helfrich, W. “Elastic Properties of Lipid Bilayers: Theory and Possible Experiments”. In: *Zeitschrift für Naturforschung C* vol. 28, no. 11-12 (Dec. 1973), pp. 693–703.

Appendix 3.A Supporting Information

3.A.1 System setup

Simulation settings. Molecular dynamics simulations were performed with the GROMACS simulation package [25] version 2019, unless stated otherwise. We used the MARTINI coarse-grained model [26] version 2.2 to simulate the lipids, nucleic acids and solvent. Timescales noted within this work are corrected for the four times faster diffusion of the coarse-grained model in comparison to atomistic simulations (multiplication by a factor of four) [26]. In all simulations, the system was coupled to a constant temperature bath using the 'V-rescale' algorithm with a relaxation time of 1.0 ps. For the solvent free replica exchange simulations a Langevin thermostat was used with a friction coefficient of 0.25 ps^{-1}. The time step used in the simulation was 20 fs. The dielectric constant in the simulations was $\epsilon_r = 15$. The neighbour-list was updated every 10 simulation steps. The pressure was isotropically coupled to 1 bar (Berendsen pressure coupling) with a relaxation time of 1.0 ps. A shifted cutoff of 1.2 nm was used for both Coulomb- and Lennard-Jones (LJ) interactions. Interactions were gradually scaled to zero beyond 1.0 nm (coulomb) and 1.0 nm (LJ) respectively.

Surfactant model. The molecular structure of a PC-C32-PC single chain bola surfactant is illustrated in Fig. 3.4. The head groups of the thermo-responsive lipid surfactant – a single chain bola lipid – were modeled by a negatively charged "Q0" 6-12 Lennard-Jones (LJ) interaction type (PO_4 group) and positively charged "Qa" 6-12 LL interaction type (NC_3 group). The 8 tails beads were modeled by "C1" 6-12 LJ interaction types. All interaction types are corresponding to the standard LJ definition within the Martini model. Bonded parameters correspond to the standard martini force-field of a DPPC lipid. The equilibrium bond angle between the phosphate and first carbon bead was set to 120 degrees.

Replica Exchange Molecular Dynamics simulations (REMD). In the solvent free simulations (Dry Martini model) replica exchange simulations were performed using Gromacs version 4.5.7. The exchange frequency was every 100 simulation steps (2 ps). In all solvent free simulations, a Langevin integrator with an inverse friction coefficient of 4 ps^{-1} was used to couple the system to a heath bath. The following temperature ladder was used:279.8 284.8 289.9 295.0 300.2 305.5 310.8 316.2 321.6 327.2 332.2 335.6 338.0 339.9 342.8 344.6 350.1 356.0 362.0 368.0 374.2 380.4 386.7 393.1 399.6 406.1 412.8 419.5 426.3 433.2 440.2 450.0 K. It is important that the 'replica density' is sufficient near the phase transition temperature such that exchanges between temperature below and above T_m can occur. The here suggested temperature ladder yields a finite acceptance ratio over all replicas. The obtained average transition probabilities are: .31 .30 .29 .31 .31

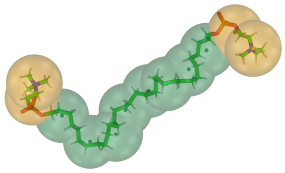

Figure 3.4: CG model of the PC-C32-PC single chain bola surfactant used in this work.

.31 .30 .29 .32 .39 .56 .69 .76 .64 .77 .39 .36 .37 .37 .38 .38 .38 .37 .37 .38 .38 .40 .39 .40 .39 .25.

Surfactants were randomly distributed over the 20 nm^3 simulation box at the start of each replica simulation to yield an unbiased starting structure. Coalescence of surfactants into micelle structures spontaneously occurs in the course of the simulations. The box dimension was 20x20x20 nm^3. Because micelle structures are attractive within the solvent free model (hydration repulsions are absent) larger box dimensions were chosen to prevent self-interactions over the periodic boundaries. It is noteworthy that these larger box dimensions do not comprise the computational efficiency, quite in contrast to the simulations performed in explicit solvent.

Each replica was equilibrated (thermalized) for 1.6 ns. The total simulation length for each replica was 1.6 μs. Simulation parameters were chosen as officially recommended for the Dry Martini model.

For the simulation in explicit solvent, we used the following temperature ladder: 270.84 271.57 272.31 273.05 273.79 274.54 275.28 276.03 276.78 277.52 278.28 279.03 279.78 280.54 281.30 282.06 282.82 283.58 284.34 285.11 285.88 286.65 287.42 288.19 288.96 289.74 290.52 291.30 292.08 292.86 293.65 294.43 295.22 296.01 296.80 297.59 298.39 299.18 299.98 300.78 301.58 302.39 303.20 304.00 304.81 305.62 306.43 307.25 308.06 308.88 309.70 310.52 311.34 312.16 312.99 313.82 314.65 315.48 316.31 317.14 317.98 318.82 319.66 320.50 321.35 322.19 323.04 323.89 324.74 325.60 326.45 327.31 328.17 329.03 329.89 330.75 331.62 332.49 333.36 334.23 335.10 335.98 336.86 337.74 338.62 339.50 340.39 341.27 342.16 343.05 343.95 344.84 345.74 346.64 347.54 348.44 349.35 350.25 351.16 352.07 352.98 353.90 354.81 355.73 356.65 357.58 358.50 359.43 360.35 361.29 362.22 363.15 364.09 365.03 365.97 366.91 367.86 368.80 369.75 370.70 K,

yielding acceptance rates of .64 .64 .63 .63 .63 .63 .63 .63 .64 .63 .64 .64 .63 .62 .63 .64 .63 .63 .63 .63 .62 .62 .63 .63 .62 .62 .62 .61 .62 .62 .62 .62 .61 .62 .62 .62 .63 .63 .62 .63 .62 .63 .64 .63 .63 .63 .64 .64 .64 .64 .64 .64 .64 .63 .64 .64 .63 .64 .64 .63 .64 .64 .64 .64 .63 .63 .64 .63 .64 .64 .63 .63 .64 .64 .64 .63 .64 .63 .64 .64 .64 .64 .65 .64 .63 .64 .64 .64 .64 .64 .64 .63 .63 .64 .63 .64 .65 .63 .64 .63 .65 .65 .64 .64 .63 .64 .64 .64 .64 .64 .64 .64 .64 .64 .64 .63 .63 .64 .64 .63. All replicas started with the disc-like micelle obtained in the solvent free simulations. In these simulations the system's potential energy and therefore the transition probability between replicas is dominated by solvent fluctuations (see Fig. 3.7). Therefore, the solvent free model gives a more reliable result of the actual structural ensemble obtained via REMD. For all replica a disc-shaped micelle formed from 144 bola lipids was used. The box dimension was 12.5x12.5x8.0 nm^3 and contained $\simeq$ 12770 solvent beads, with 1260 of which being Martini Anti-freeze water beads. Each replica was equilibrated for 1.2 ns in the *NVT* ensemble and 4 ns in the *NPT* ensemble. The total simulation length for each replica was 1.2 μs. The velocity rescale algorithm was used for temperature coupling and the Berendsen barostat for pressure coupling respectively. Coupling parameters were chosen in accordance with the recommended simulation parameters for the Martini model, which can be found on the official Martini webpage.

Worm-like micelles. The periodic worm-like micelles used for estimating the scission barrier consist of 100 surfactants and about 7010 solvent beads. The box dimension was $8.5 \times 8.5 \times 14.1$ nm^3. These periodic worm-like micelles were constructed from spontaneous aggregation by randomly placing lipids within a cylindrically confined region (a flat bottom potential) with a radius of 2.5 nm (at 360 K). The large disc-like micelle of 500 surfactants was obtained by stacking the continues worm-like micelle along the x-dimension. The slow and computationally expensive transition toward disc-like structures was obtained by simulating this worm-like micelle at 273 K for about 10 microseconds using the solvent free version of the model. The heat shock simulations were performed in explicit solvent in a system with a box dimension of $40 \times 20 \times 22$ nm^3 containing 120000 solvent beads.

DNA simulations. All DNA simulations were performed using a coarse-grained model of an 12-base pair double stranded DNA d(CCCCCTTTTTCC)2 [70]. The toroidal micelles were comprised of 72 neutral PC-C32-PC lipids and 72 cationic lipids. Cationic lipids where modeled by modeling the phosphate group as electrically neutral. The box dimension was 11x11x8.4 nm^3 and contained $\simeq$ 6500 solvent beads. In these simulations long range electrostatics were introduced using the particle-mesh Ewald summation method. Electrostatic screening by the solvent is implicit via the dielectric constant, $\epsilon_r = 15$. Counter ions were added to ensure electrostatically neutral conditions. It should be noted that electrostatics is

only semi-quantitatively described by these type of coarse-grained models.

SAXS and SANS spectra. Scattering spectra were resolved using the CRYSON and CRYSOL online servers (https://www.embl-hamburg.de/biosaxs/atsas-online/) [46, 47] using default settings. This server requires an atomistic structure file (pdb file) as an input to resolve the corresponding spectra. Atomistic structures of micelles were obtained by back mapping the obtained coarse-grained structure using the INITRAM platform in combination with the CHARMM36 force-field [71].

3.A.2 Free energy calculations

Free energies were calculated using a modified version of the improved string method [72–75]. For these calculations a customised version of GROMACS 4.6.4 was used. The string method allows for the reconstruction of a physical path, i.e. the path of the minimum free energy (MFEP), between the two end-states. This path represents the most likely reaction pathway for the transition between the reference states. This is achieved by an iterative two step procedure. First, the free energy of the morphologies along the path (string) are minimized due to the gradient of the free energy in density space, which is described by the local chemical potential

$$\mu_{\mathrm{up}}(\mathbf{r}) = \frac{\delta F_{\mathrm{up}}(m(\mathbf{r}))}{\delta m(\mathbf{r})} = k\, k_{\mathrm{B}} T [m(\mathbf{r}) - \langle \hat{m}(\mathbf{r}, \{\mathbf{r}\})\rangle] \tag{3.1}$$

where $\hat{m}(r)$ are the local densities computed from the coordinates of a reference structure and $m(r)$ are the instantaneous local densities. The factor k denotes the force constant of the harmonic umbrella potential. The chemical potential is computed by performing short restrained simulations of all configurations along the string within the applied umbrella field (V_{up}). The excess local chemical potential μ balancing the applied external field is directly derived from the difference of the reference density field and the average density distribution during the simulation. The reference densities of the successive iteration are reevaluated by

$$m(\mathbf{c})_n = m(\mathbf{c})_{n-1} - \frac{\mu(\mathbf{c})}{k_{\mathrm{B}} T}\epsilon, \tag{3.2}$$

where ϵ is a constant defining the "speed" of this evolution, $m(\mathbf{c})$ and $\mu(\mathbf{c})$ are the local density and chemical potential at a given grid point $\mathbf{c}$. This leads to a minimization of the free energy of the system, which effectively means a quenching of fluctuations around the meta-stable state.

In a second step the string is reparameterized and renormalized via fitting to cubic splines such that all morphologies are positioned equidistantly along the path (distances are normalized with respect to the overall arclength).

The free-energy differences along the MFEP can be obtained by integration over the chemical potential along the path, given by the contour parameter s.

$$\begin{aligned} \Delta F(s) &= \int_0^s \mathrm{d}s' \frac{\mathrm{d}F}{\mathrm{d}s'}, \\ \frac{\mathrm{d}F}{\mathrm{d}s} &= \int \mathrm{d}^3\mathbf{r} \frac{\delta F[m_s]}{\delta m_s} \frac{\mathrm{d}m_s}{\mathrm{d}s} \\ &= \int \mathrm{d}^3\mathbf{r} \mu_s(\mathbf{r}) \frac{\mathrm{d}m_s(\mathbf{r})}{\mathrm{d}s} \end{aligned} \tag{3.3}$$

This integration is a volumetric, multidimensional equivalent of integrating the force along the arclength to obtain the performed equilibrium work.

The scission reaction was split in 30 consecutive simulation windows based on linear interpolation of the calculated density vector of the two end states. An umbrella field strength of $k = 50\,\mathrm{kJmol^{-1}nm^3}$ was used. This value was chosen based on experience as a balance between maintaining the configuration of a specific point along the string, yet enabling free diffusion of the lipids. It is important to emphasize that this field only acts on the hydrophobic density, i.e. the carbon tails of the surfactants (C1 beads within the martini model). Scission end states were obtained by exploiting the ability of the density field method to impose manually constructed 'voids' within the hydrophobic density. The string, i.e. the local reference densities of the 30 morphologies, was iteratively evaluated and updated every 10 ns. Free energy calculations were performed within the *NVT* ensemble after a short relaxation within the *NPT* ensemble. This choice of ensemble is not expected to significantly ($< 1\,k_\mathrm{B}T$) affect the free energy difference between the end states.

3.A.3 Bending free energy of a toroidal micelle

Since a toroidal micelle has zero Gaussian curvature, it can be described by a line with one principle radius $1/R$ and a bending modulus κ. The bending free energy per unit length is given by $F = \frac{1}{2}\kappa(\frac{1}{R})^2$ [17]. Since the arclength of the torus is $2\pi R$ the total bending free energy of the torus reduces to $2\pi R \times \frac{1}{2}\kappa(\frac{1}{R})^2 \rightarrow F(R) = \frac{\kappa\pi}{R}$. $F(R)$ has no free energy minimum and favors growth toward an infinite radius. However, creation of excess arclength is penalized by a tension due to the compressibilty of the micelle. Owing to a large compressibility the concomitant

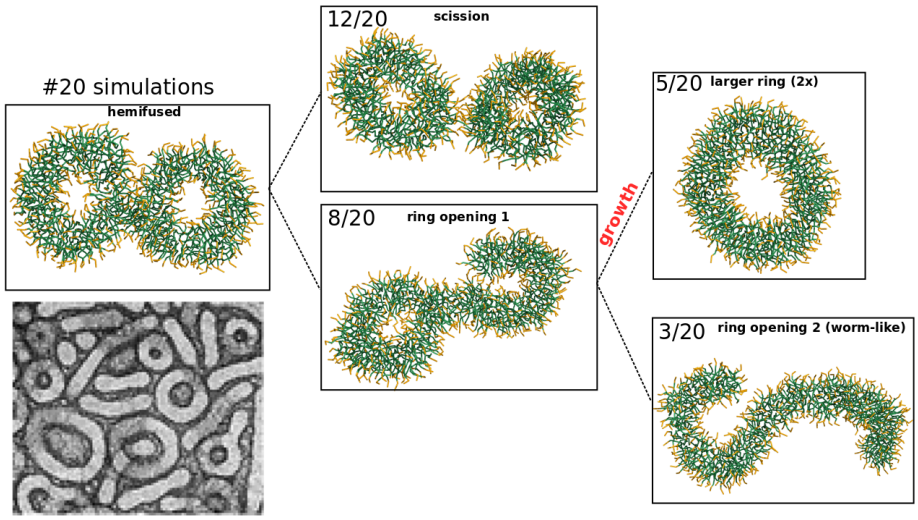

Figure 3.5: Hemifused toroidal micelles. We performed 20 independent 1 μs simulations of two hemifused toroidal micelles at 360 K. Scission into two independent micelles is the most likely pathway. Alternatively, ring opening can occur and results in a key-like structure. The remaining tail is either completely absorbed by the growing ring or a successive, second ring opening event occurs which results in a worm-like micelle. Ring opening thus mainly occurs in the presence of branched structures. The inset show an example of the corresponding structural ensemble observed in experiments [8].

strain energy is small in comparison to the bending free energy and is therefore being omitted in our rationalization of toroidal micelle formation.

3.A.4 Entropic contribution to the free energy barrier of toroidal micelle formation

We model a growing micelle via step-growth polymerization like a random walk in three dimensions. The end-to-end vector $\vec{R}$ of the worm-like micelle with contour length L is distributed according to the following probability density function $P(\vec{R}) = (\frac{3}{2\pi Ll})^{3/2} e^{-\frac{3\vec{R}^2}{2Ll}}$, with l being the statistical chain length [76–78]. The probability to form a toroidal micelle is given by $P_{\text{tor}} = \int_0^{\epsilon} 4\pi R^2 P(\vec{R}) dR$ with ϵ being a small fixed minimal distance that suffices for fusion of the two free ends. The distribution $P(\vec{R})$ widens when L increases and since ϵ is a fixed quantity P_{tor} decreases with increasing L. The normalization factor $(\frac{3}{2\pi Ll})^{3/2}$ rescales the integral when L increases. Therefore, the scaling of P_{tor} with L is of the form $P_{\text{tor}} \propto L^{-\beta}$ ($\beta > 0$). This general form is conserved even when the random walk

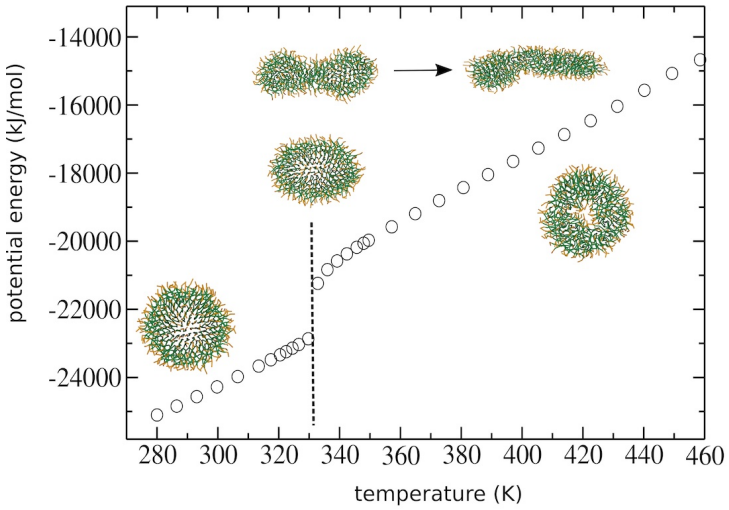

Figure 3.6: Temperature replica exchange molecular dynamics simulations of an self-aggregate consisting of 144 surfactants. The phase transition temperature T_m (about 330 K in this model) is characterized by a jump in the temperature versus potential energy relationship (vertical dashed line). The structural space is dominated by disc-like micelles $< T_m$ and toroidal micelles ($> T_m$). Slightly above 330 K deformed discs and occasional double disc structures ('propeller' like structures) are formed consisting of smaller discs. This latter structure escapes into a worm-like micelle fragment rather than a toroidal micelle likely because the small size of the disc does not enable such a transition. In this example, all simulations started from a random spatial distribution of surfactants over the simulation box (solvent free model).

deviates from ideal behavior. Since the free energy ΔF is proportional to $-lnP_{tor}$, it immediately follows that $\Delta F \propto \beta lnL$. It is important to emphasize that this weak contribution plays in fact little to no role in the formation of highly curved toroidal micelles (L is in the order of the thickness of the worm-like micelle). Formation of highly curved toroidal micelles is predominantly determined by the bending free energy.

3.A.5 Bending modulus of the worm-like micelle

Estimation of the elastic bending modulus of a worm-like micelle is inspired by the observation of a tri-junction formed after ring opening of two hemifused toroidal micelles. The attached appendix is subsequently absorbed by the toroidal micelle due to the inclination to minimize the bending free energy (see Fig. 3.12).

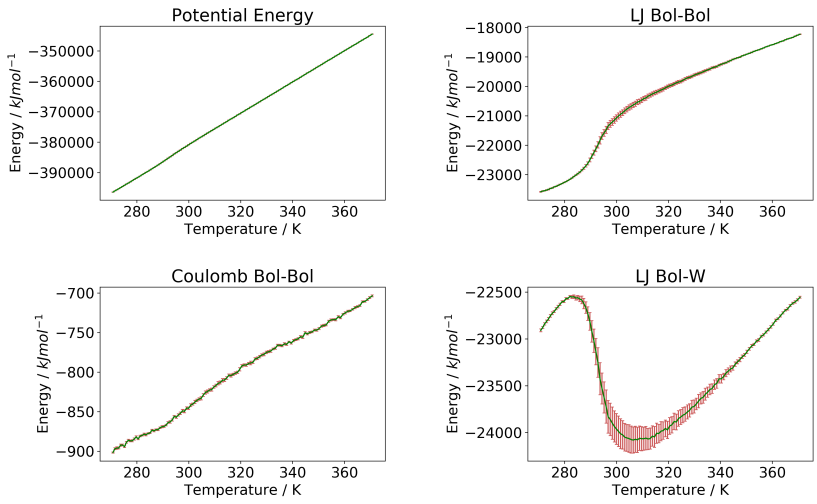

Figure 3.7: Temperature replica exchange molecular dynamics simulations of an self-aggregate consisting of 144 surfactants under explicit solvent conditions. Detailed analysis of enthalpy (potential energy). The linear behavior of the potential energy with temperature is because of the presence of solvent. The potential energy can be decomposed into Lennard-Jones (LJ) and electrostatic (Coulomb) contributions from bola lipids (Bol) and solvent (W). The trend in lipid-lipid interactions (bol-bol) suggests a chain melting temperature of about 295 K under explicit solvent conditions. The obtained structural ensemble features disc-like ($< T_{\mathrm{m}}$) and toroidal micelles ($> T_{\mathrm{m}}$).

Hence, the absorption force F_L exerted by the growing toroidal micelle directly relates to the bending modulus, κ. The bending free energy of the toroidal micelle is given by, $F = \frac{\kappa\pi}{R}$. Minimization of the bending free energy results in an excess line tension. The concomitant radial force that drives growth of the micelle's radius via absorption of the appendix is, $\frac{dF}{dR} = -\frac{\kappa\pi}{R^2}$. The relationship between the radial force and the line tension (the line tension equals the absorption force F_L) is given by the geometric conversion: $\frac{dF}{dR} = 2\pi F_L$. Substitution yields, $-\frac{\kappa\pi}{R^2} = 2\pi F_L \rightarrow \kappa = -2F_L R^2$. The absorption force F_L can be directly measured from a long simulation at a fixed length L (see Fig. 3.12). Owing to the micelle's large resistance against stretching the obtained value of κ lies close to the value of κ at tension-less conditions.

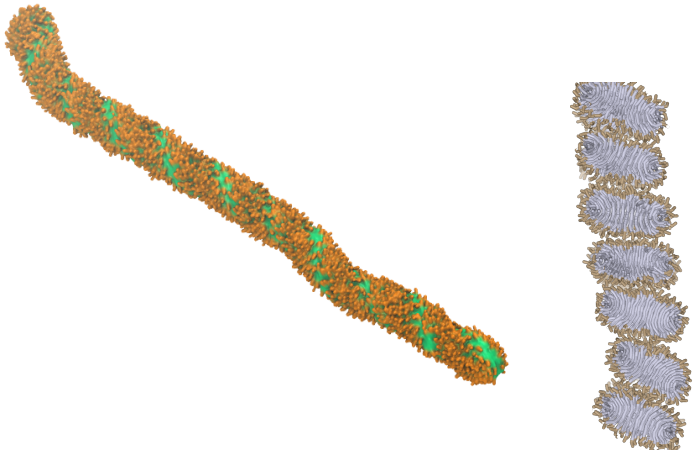

Figure 3.8: (left) Helical fibril formed by bola surfactants with an inherently stiff hydrophobic chain, i.e. the hydrophobic chain is modeled as a stiff rod (a harmonic bond angle potential with a force constant of 10000 kJ/mol). The helix features a hydrophobic pitch/grove (colored green) running over the surface of the helix. Reintroduction of realistic chain flexibility rapidly transits such a helix into a worm-like cell even below T_{m} indicating loss of thermodynamic stability. (right) Repetitive stacking of slightly tilted discs may alternatively explain the observation of fibrils with a faint helical appearance as has been observed in "uranyl stained" transmission electron microscopy of hydrogels formed by lipid bola amphiphiles [30, 68]

3.A.6 Scale dependence of the scission barrier

To explore the influence of length scale on the stability of the toroidal micelle, we express the bending free energy stored in a toroidal micelle in terms of the radius of its constituting cylinder r and the radius of the toroidal micelle R (see Fig. 3.13). Since the overall shape of the torus itself and therefore its bending free energy is largely conserved at the scission barrier, the free energy barrier against ring opening mainly stems from the excess bending free energy required to create two hemispherical free end caps with a mean curvature of $1/r$. Therefore, the goal is to derive how the free energy energy of the two end caps $2F_{\mathrm{end}}$ scales with r. To this aim, we suppose that the constituent rod is a Hookean material, homogeneous, with Young's modulus Y. The bending free energy per unit length F_r is given by $F_r = \frac{1}{2}YI(\frac{1}{R})^2$ with I being the moment of inertia of the rod's cross section. For a solid rod $I = \frac{\pi}{4}r^4$. Therefore, the bending free energy per unit length is given by $F_r = \frac{\pi}{8}Yr^4(1/R)^2$. Equivalently, F_r can be expressed in terms of the bending modulus $\kappa \rightarrow F_r = 1/2\kappa(1/R)^2$. Therefore, κ can be alternatively written in terms of Y as, $\kappa = \frac{\pi}{4}Yr^4$. This expression illustrates that $\kappa \propto r^4$. Since

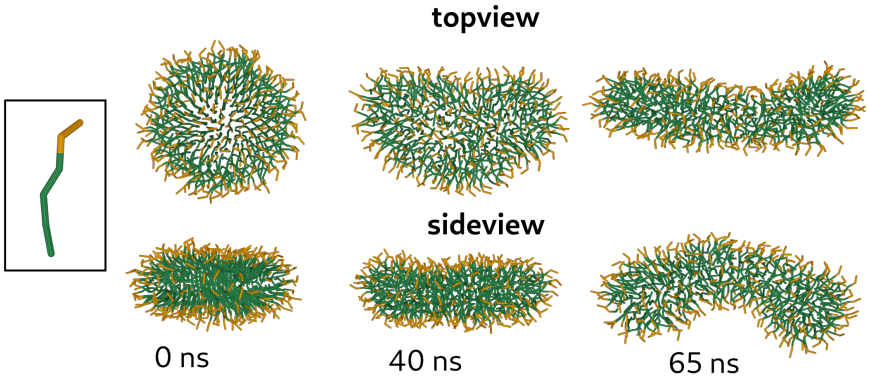

Figure 3.9: Simulations of a preformed hexagonally shaped at 275 K with the bola surfactants being ’sliced in halve’ thereby yielding a lipid surfactant with a regular architecture (shown in the inset). The disc rapidly loses it structural stability and morphs into a regular worm-like micelle despite conservation of the overall hydrophobic and hydrophilic volume fraction. These simulations illustrate the important role ’bolafication’ of surfactants plays in stabilizing the disc’s structure.

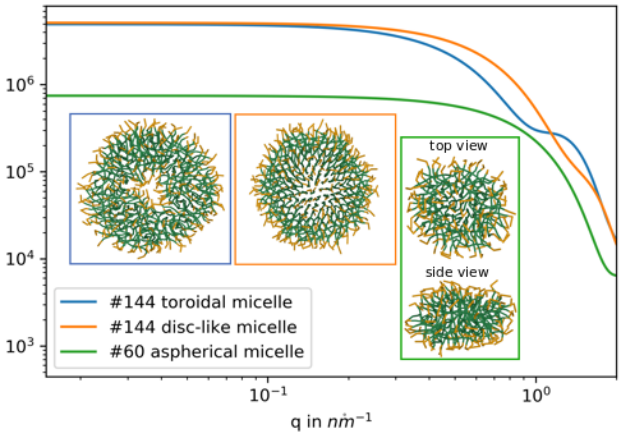

Figure 3.10: SANS spectrum resolved for a toroidal micelle, a disc-like micelle in the gel phase ($< T_m$), and a small ‘aspherical’ micelle consisting of 60 surfactants only. Molecular snapshots of the three corresponding structures are illustrated in the inset.

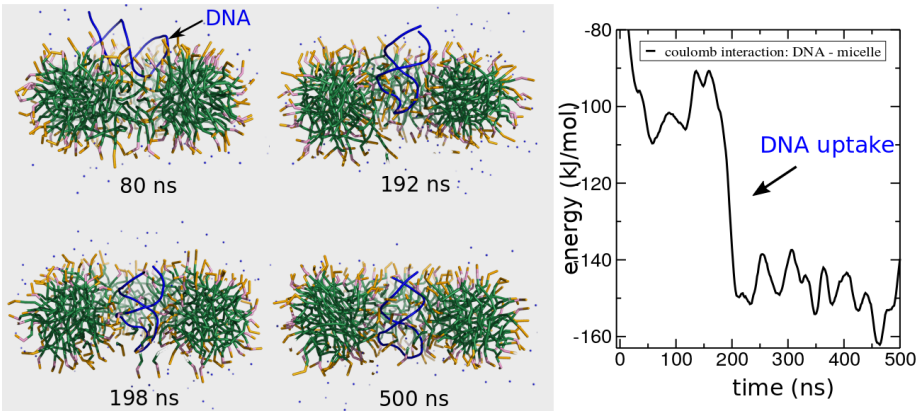

Figure 3.11: Molecular simulations illustrating the spontaneous uptake of a 12-base pair double stranded DNA fragment by a 10 nm-sized toroidal micelle (144 surfactants) comprised of 50 % cationic and 50 % zwitterionic lipid surfactants. The micelle has a positive net charge, the DNA is negatively charged. DNA uptake is driven by a gain in Coulomb energy. Counter ions (Cl^-) are depicted as blue spheres.

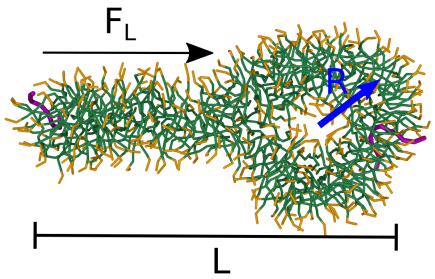

Figure 3.12: Calculation of the bending modulus. Since a toroidal micelle of radius R tends to minimize its free energy via additional radial growth, the attached appendix is being absorbed due to a force F_L. This force is measured by conserving the distance L, i.e. the distance between the center of mass of the two purple colored lipids. The total system contains 189 lipids. The radius of this (smaller) ring is about 2.5 nm as measured from the hydrophobic center of the constituting cylinder. The force F_L ,measured over 600 ns simulation, is $-7.8 \pm 1.0\ k_BT$/nm or about 38 pN (a considerable pulling force on a molecular scale). Therefore, the resulting bending modulus $\kappa = 97.5\ k_BT{\cdot}$nm or about $100\ k_BT{\cdot}$nm.

the diameter of a highly curved polymeric toroidal micelle is a tenfold larger, and given that the aspect ratio r/R is conserved, the diameter of its constituting cylinder will also be a tenfold thicker. Consequently, κ increases by a factor, $10^4 = 10000$.

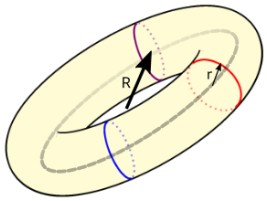

Figure 3.13: Sketch of a torus with total radius R. The radius of the constituent cylinder is r. The gauss-bonnet theorem dictates that a torus has zero Gaussian curvature. Because of symmetry the integral Gaussian curvature of each cross-section along the contour of the torus (e.g., indicated by the blue, red and purple circles) must therefore also be equal to zero. Consequently, the free energy density along the contour only depends on the mean curvature and its concomitant elastic modulus. A torus can therefore alternatively be modeled by a line (colored grey) with a single effective bending modulus [17]

Finally, we need to establish a relationship between the bending modulus κ of the constituent worm-like micelle and the elastic free energy of the two hemispherical free end caps, $2F_{\text{end}}$. The Helfrich elastic free energy [79] of a spherical lipid vesicle F_{ves} with a radius R is given by, $F_{\text{ves}} = \int_A (2\kappa_{\text{mem}} \frac{1}{R^2} + \overline{\kappa}_{\text{mem}} \frac{1}{R^2})$. Integration over the surface area $4\pi R^2$ yields a constant free energy, $F_{\text{ves}} = 8\pi\kappa_{\text{mem}} + 4\pi\overline{\kappa}_{\text{mem}}$, whose value is invariant of R and only dependents on the *independent* contributions of the mean curvature modulus κ_{mem} and the Gaussian curvature modulus $\overline{\kappa}_{\text{mem}}$ [79]. Equivalently, the free energy of the micelle's hemispherical end cap in the monolayer representation is of the form $2F_{\text{end}} = 8\pi\kappa_{\text{mono}}(r) + 4\pi\overline{\kappa}_{\text{mono}}(r)$. Thus, $2F_{\text{end}}$ is linearly proportional to the value of each elastic modulus within the monolayer representation.

In contrast to a vesicle, a toroidal micelle has zero overall Gaussian curvature because its genus is 1 (gauss-bonnet theorem) and its bending free energy is thus independent on the value of $\overline{\kappa}_{\text{mono}}$ [15]. Cross-sections of the torus are indicated by different colored circles with radius r in(see Fig. 3.13). Because of symmetry, the total integral Gaussian curvature of a torus can only vanish when the local integral Gaussian curvature of each cross-section vanishes. Consequently, the contour's free energy density can be modeled by a line (colored grey line in Fig. 3.13) subject to a single, effective modulus κ. In case of an open

torus, the Gaussian curvature only contributes to the free energy of the two hemispherical free end caps – the scission barrier – whose total free energy can be described by the above constant $2F_{\text{end}}$. The free energy density of the torus' cross-section must be equivalent in both Hamiltonian descriptions [15, 17], $\int_L \frac{1}{2}\kappa(1/R)^2 \rightarrow \int_A (\frac{1}{2}\kappa_{\text{mono}}(2H(R,r))^2 + \overline{\kappa}_{\text{mono}}K(R,r))$, with H being the local mean curvature and K the local Gaussian curvature. The first Hamiltonian does not explicitly depend on r since its contribution to the free energy density is effectively embedded within the value of κ: $\kappa \propto \kappa_{\text{mono}} r$. Hence, the dimension of κ is energy times length whereas the dimension of κ_{mono} is energy. Finally, since $2F_{\text{end}}$ is linear proportional to κ_{mono} it thus follows that $2F_{\text{end}} \propto r^3$. However, this estimation only provides a lower bound on how $2F_{\text{end}}$ scales with r since the contribution of $4\pi\overline{\kappa}_{\text{mono}}(r)$ is not known. The estimation holds as long as $4\pi\overline{\kappa}_{\text{mono}}(r)$ scales similar or less with r than $8\pi\kappa_{\text{mono}}(r)$.

Appendix 3.B DFTI Calculation

We used the DFTI method as described in Chapter 0 to calculate the free energy difference between a bolo lipid torus and a worm-like micelle (see 3.3). A quadratic coupling scheme (Sec. 2.3.2.1) in combination with the proposed minimization scheme (2.3.3) was used. Due to strong fluctuations in a very weak restraining field the evaluation of the full thermodynamic cycle is not possible. In accordance to our results obtained for the scission of the continuous WM Fig. 3.14 we were able to reproduce the results obtained via the string method (Fig. 3.3). The result of 14.20+-1.23 (k = 100: 15.43±1.63) for the morphing in the restraining external potential are in good agreement with our results from the string method (16.25±0.99). This serves as an additional prove of concept for the DFTI method.

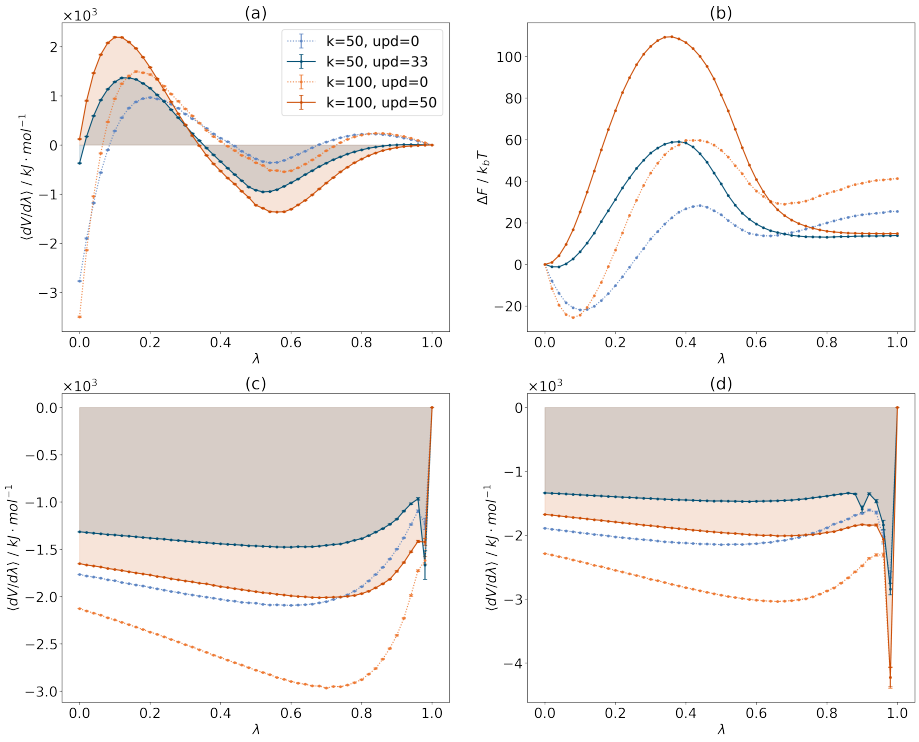

Figure 3.14: DFTI of the scission event of a toroidal bola lipid micelle using a quadratic coupling scheme without optimization and after 33/59 updates. (a) Switching of the density field from a torus to a wormlike micelle. (b) Cumulative change of free energy along reaction coordinate calculated from the chemical potential for different $k = 50, 100$. (c/d)The free energy contribution associated with switching off the restraining field for torus/WM. Values of the field strength k are in units of $\mathrm{kJmol^{-1}nm^3}$.

Chapter 4

Lipid Droplet Modelling

4.1 Introduction

Lipid droplets, also called lipid bodies, fat bodies, adiposomes or oil bodies in plants, are the organelles that serve as energy storage in cells. These $1 - 100\,\mu m$ sized objects are found in most eukaryotic cells and have become a very active field of research with ever growing interest in the last decade [38, 39]. LDs are set apart from other organelles found in the cell by their unique architecture: An accumulation of predominantly neutral lipids and sterol esters shielded from the cytosol by a phospholipid monolayer [40].

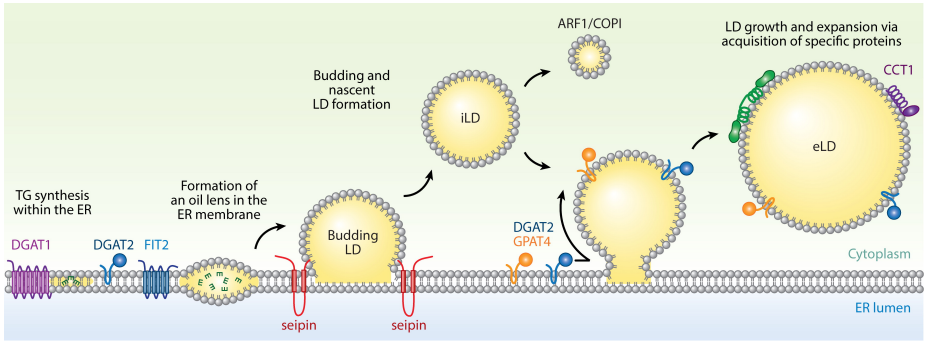

Walther TC, et al. 2017.
Annu. Rev. Cell Dev. Biol. 33:491–510

Figure 4.1: Lipid droplet biogenesis model: The droplets are formed by accumulation of neutral lipids, synthesized by DGAT1 and DGAT2, in the bilayer of the endoplasmic reticulum. After reaching a certain size the oil lenses bud towards the cytoplasm. Most lipid droplets remain connected to the ER, acquiring specific proteins through lipid bridges, while some may disconnect. (Republished with permission of ANNUAL REVIEWS, INC., from Ref. [41]; permission conveyed through Copyright Clearance Center Inc.).

Figure 4.1 shows the lipid droplet biogenesis as proposed by Walther et al. [41]. The neutral lipids forming the droplets are mostly triaclyglycerols (TAG) formed by esterification of fatty acids in the endoplasmic reticulum (ER). The droplets

are at the core of lipid metabolism, growing in nutrition excess and releasing the neutral lipids for energy production when needed. At a critical nucleation concentration (CNC) of 3-10 mol% these lipids phase separate to form TAG lenses between the two leaflets of the ER membrane [42–44]. Formed lenses eventually coalesce or grow to form nascent droplets that unidirectionally emerge from the ER bilayer towards the cytosol [45, 46]. This budded state of TAG lenses with sizes <200 µm is labeled nascent lipids droplets (nLDs). The size of the droplets at which this process occurs and the mechanism are not yet well understood.

Early stage droplet formation (lenses, nLDs) is elusive to all experimental techniques at hand [44]. Usage of neutral lipid fluorescence dyes fails for small assemblies of neutral lipids. Wang et al. detected early stage droplets of ~ 0.4 µm using a fluorescence labelling of the GPAT4 membrane hairpin domain (*LiveDrop* method) [47]. nLDs detected via electron microscopy tomography are in the range of 30-60 nm [48].

Also in the later stages of the droplet's life, many open questions remain, e.g. whether a formed droplet leaves the ER entirely or permanently stays connected or how the growth process of the droplets is coordinated [49, 50]. Various studies found that many factors may drive or influence the budding process, such as membrane asymmetry, surface tension, lipid composition and/or ER topology [51–53]. Lipids that promote negative spontaneous curvature, e.g. diacylglycerols (DAGs), facilitate LD embedding, whereas lipids promoting positive spontaneous curvature, e.g. lysolipids, help the budding process [54, 55]. It is debated whether an assymetry in the lipid composition between the layers [56] or the positive curvature of the tubular ER gives rise to the direction of the emergence [54].

Chorlay et al. extensively studied the effect of surface tension budding direction of LDs using on the droplet shape to describe the dewetting. Their experiments suggest that for droplets > 20 nm the effect of surface tension dominates over curvature effects and an asymmetry in the surface tensions of inner and outer monolayer determines directionality [57]. Deslandes et al. [58] found that neither intrinsic ER asymmetry, nor spontaneous curvature of the monolayers, but rather the marked difference in surface tension between bilayer ($\sim 10^{-5}$ N/m [52]) and monolayer ($\sim 10^{-3}$ N/m [59]) is critical for budding.

The rich proteom associated with the droplet monolayer and the contact site between LD and ER is investigated for its potential role in regulating the aspects of the droplet formation. Amongst other proteins, such as Rab18, FIT2, Pex30 and ACLS3, seipin was found to be one key player in the regulation of the droplet formation [45, 46, 50]. Seipin foci were found to be moving along the ER until colocalizing with the formation sites of the neutral lipid lenses [50].

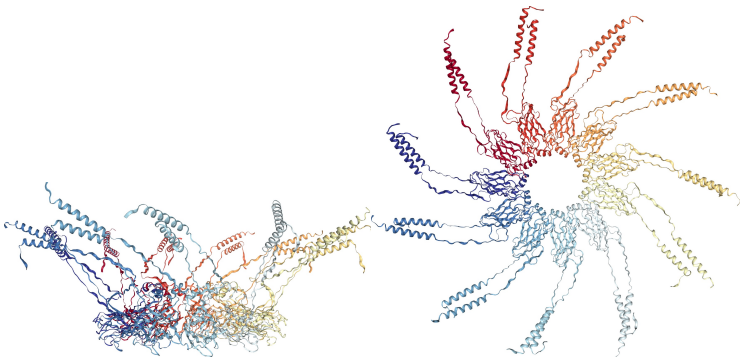

Figure 4.2: Seipin undecamer model generated on basis of Cryo-EM structure 6DS5 [66] using MODELLER. Color code is chosen by protomer. *left*: side view, *right*: top-view

A deficiency or mutations of seipin lead to abnormal droplet formation (supersized or tiny) and are linked to neuronal disorders and lipodystrophy [46, 47, 49, 60–62]. The exact role of seipin in LD formation is yet to be clarified. Hypotheses range from a role in stabilizing nascent droplets, destabilizing the ER membrane in order to allow growth of lenses [63], regulating TAG delivery to already formed droplets [64] or stabilizing the contact between ER and LD [65].

The structure of the highly conserved seipin oligomers was only recently revealed by Cryo-EM imaging [66, 67]. Human seipin was found to arrange as undecamer in a ring shape (Fig. 4.2).

Each protomer possesses two transmembrane helices linked by a luminal part localized in the ER lumen. The core of the seipin ring, surrounded by the 11 protomer β-sandwich, is formed by hydrophobic α-helices serving as membrane anchor [66]. The well conserved luminal domain has high similarity to known lipid binding proteins and was shown to be able to bind phosphatic acid (PA). This suggests a role in phospholipid (PL) or DAG synthesis by facilitating access of metabolic enzymes to their reagents [66].

Salo et al. captured the ER-LD contact site via electron microscopy. They observed well-defined neck-like structures of sizes in the range of the seipin oligomer, suggesting the hypothesis that seipin is crucial to maintain this structure [64].

However, there are many open question and factors that need consideration on the journey to understanding the mechanism of initial formation and budding process of LDs.

The aim of this project was to build a coarse-grained lipid droplet system that allows studying the budding process. The multiple factors that are potentially important for the budding process require a highly adaptable model. The choice of the MARTINI model offers the option to easily alter the system. The model was intended to be used with our free-energy methods to elucidate the energetic requirement associated with the budding process and to investigate whether seipin may facilitate the process by stabilizing the bilayer/LD contact. The budding process was to be studied with and without seipin to compare differences that may arise due to the presence of the protein. To this aim, a coarse-grained structure of the seipin dodecamer needed to be prepared from the cryo-EM structure which lacks the transmembrane domain.

4.2 Simulation Setup

Simulation and Analysis Tools All simulations were performed using the GROMACS simulation package, v2019.6 or v2020.4 [24–26]. Trajectories were analysed using the python package MDAnalysis v1.0 [68] and visualized using nglview v2.7.7. All simulation parameters follow the official recommendations for the MARTINI force field [30, 69]. Furthermore, INSANE [70] was used for generation of POPC (palmitoyl-2-oleoyl-sn-glycero-3-phosphocholine) bilayers, the Modeller package v9.21 for protein modelling and MARTINIZE v2.6 [71] for coarse-graining of atomistic structures.

Lipid Droplet Model The lipid droplet model was built by multiple short assembly steps using the DRYMARTINI model (v2.1). The simulations were performed using GROMACS v2019.6 using a leap-frog stochastic dynamics integrator (SD) at 310 K with a time step of 40 fs. The shift algorithm was used for electrostatic interactions. with a cut-off of 1.2 nm. A single cut-off of 1.4 nm was used for Van der Waals interactions. Pressure coupling was done with the Berendsen barostat with a reference pressure of 0 bar and semiisotropic coupling. The neutral lipid core containing 2000 TAG molecules (triolein, parametrization in accordance to Ref. [72]) was formed by self-assembly from a random distribution. POPC was added to the box until no additional molecules were accommodated in the self-assembled monolayer formed around the neutral lipid lens. The formed droplet was joined at varying distance with a 40x40 nm POPC membrane assembled using the INSANE tool to form a lens and a budded droplet. A flat-bottom restraining potential was used to establish a membrane protrusion connecting the initial droplet with the bilayer for the budded droplet setup. The resulting system was solvated using standard MARTINI water.

Lipid Droplet Asymmetry Reduction The simulations were performed using GROMACS v2020.4 using a time step of 30 fs and the force field parameters of the MARTINI model (v2.2). Neighbour searching was performed every 20 steps. The reaction-field algorithm was used for non-bonded interactions with a cut-off of 1.1 nm. After energy minimization the simulations were carried out in the *NPT* ensemble. A pressure of 1 bar was ensured using the Parrinello–Rahman barostat [73] Temperature was controlled at 310 K using the V-rescale thermostat [74]. The POPC asymmetry was reduced in steps of 18 POPC over a course of 78 consecutive simulations of 300 ns. After each simulation a python script (MDAnalysis) was used to identify the leaflets, randomly select POPCs for deletion and generate new input configurations and topologies.

Pulling Simulations The simulations were performed using GROMACS v2020.4. A leap-frog stochastic dynamics integrator (SD) was used at 310 K with a time step of 30 fs. The Shift algorithm was used for electrostatic interactions with a cut-off of 1.2 nm. Pressure was maintained at 0 bar with the Berendsen barostat and semiisotropic coupling. The implicit solvent DRYMARTINI model was used. Different pull coordinates were tested on a LD lens using all TAG molecules and the POPC molecules of the lower monolayer as reference groups. A 10 nm pore was introduced using a cylindrical flat bottom potential on the POPC molecules oriented along the z-axis. A pull rate of 0.00002 nm ps^{-1} and a force constant of 500 kJ mol^{-1} nm^{-2} was used.

Alchemical Transformation A solvated 10x10 nm^2 POPC bilayer was prepared using INSANE. The leap-frog stochastic dynamics integrator (SD) was used with a time step of 30 fs and the temperature set to 310 K. The Shift algorithm was used for electrostatic interactions with a cut-off of 1.2 nm and pressure was maintained at 1 bar using the Parinello-Rahman with semiisotropic coupling. A cutoff of 1.1 nm and a table-extension to 2.5 nm was used. The POPC that were decoupled were set as reference group for the decoupling. First the Coulomb interactions were decoupled in λ steps of 0.1 (10 Windows) followed by the decoupling of the VdW interactions over 30 steps (mdp-option vdw-q). Intra-molecular non-bonded interactions were decoupled as well (couple-intramol=yes). A soft-core potential was used with an sc-alpha set to 0.5 and sc-sigma to 0.47 to account for the larger MARTINI beads.

Seipin The undecamer of human seipin was modeled based on cryo-EM structure 6DS5 (RCSB-PDB) [66]. The cryo-EM structure does not resolve the transmembrane helices and a short luminal part at the N- and C-terminus of the protein. Thus, these parts were added to the structure using Modeller. The

transmembrane α-helices were modelled for aa. 27-47 and 247-270 in accordance to Wee et al. [75]. The N- and C-terminal cytosolic domains (aa. 1-19 and 274-398) were omitted from the structure. Constraints were added to orient the α-helices orthogonally to the luminal part. The atomistic structure was coarse grained using the MARTINI tool MARTINIZE.

Seipin was inserted into a 20 nm membrane disc and a salt concentration of 0.15 M using the INSANE tool [70]. After energy minimization a 150 ns simulation was performed to relax the structure. The simulation was carried out using GROMACS v2020.4 with the standard leap-frog integrator and a time step of 30 fs. Neighbour searching was performed every 20 steps. The Reaction-Field algorithm was used for non-bonded interactions with a cut-off of 1.1 nm. Temperature coupling was maintaind at 310 K with the V-rescale algorithm and pressure was coupled at 1 bar with the Parrinello-Rahman algorithm.

In order to study the interaction of seipin with TAG blisters a 45x45 nm^2 membrane containing 14.8 mol% TAG was prepared. Seipin was inserted as a cylindrical cut-out from the equilibrated structure into the TAG-containing membrane using MDAnalysis routines [68]. The resulting TAG concentration was 11.7 mol%. After energy minimization and a short equilibration, a simulation of 15 μs was performed.

4.3 Results and Discussion

Stability of the budded state The droplet shape and dewetting from the bilayer in experimental setups, such as the droplet-embedded vesicle system, is governed by surface tension [57]. The tension can be modulated by the surface coverage of the monolayers. The budded droplet state described in 4.2 was modelled such that the monolayer which accomodates the majority of the droplet contains more lipids than the other monolayer. Since the system is confined in a box with periodic boundary conditions and lipid flip-flops are unlikely to occur on the timescale of the simulations due to high energy barriers [76], there is no material exchange between the monolayers. The fat-storage-inducing transmembrane protein 2 (FIT2) is thought to regulate supply of new phospholipids to the ER, regulating surface tension and possibly facilitating adaptation of new morphologies [77].

In order to drive the droplet system from a lens to a budded droplet or vice versa, the lipid coverage and thus the asymmetry between the two membrane leaflets can be increased/decreased. In order to test the stability of the budded state and generate morphologies of intermediate states, two types of simulations allowing for the compensation of the PL asymmetry of the initial systems were

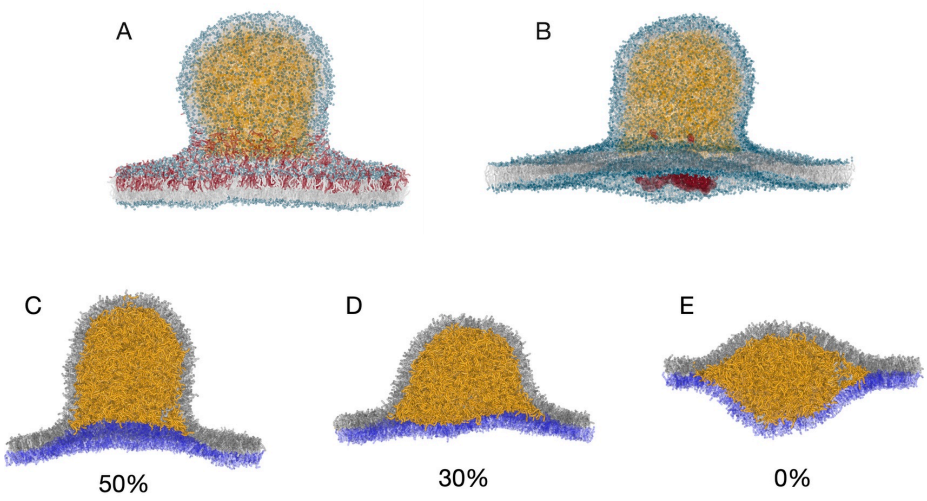

Figure 4.3: Snapshots of the LD model: A) Depiction of the deletion scheme: POPC molecules are randomly selected (red) and deleted from the configuration (number of selected POPC in the figure is not representative of the actual selection (18 POPC)). B) Putative role of seipin (red): structural stabilization of the LD/bilayer contact. C-D) Snapshots at various monolayer asymmetries (50,30 and 0%).

performed. The asymmetry can be modulated by simply successively deleting excess PLs from one monolayer. This is done in independent simulations that are automatically set up via a script that performs the manipulation of the configurations. The morphologies obtained (Fig. 4.3C-E) are in agreement with simulations performed by Chorlay et al. on a comparable LD system [51]. An alternative route is to introduce a pore into the bilayer surrounding the droplet. This setup leads to similar intermediates while keeping the number of molecules constant. This property is important considering that our free-energy methods, such as the string method or the density field thermodynamic integration (see Sec. 3.A.2 and Chap. 2) are only designed for use within the *NVT* ensemble as of the writing of this thesis. Using an 8 nm pore formed via a repulsive harmonic potential the budded droplet state collapsed into forming a lens over the course of a 2 μs simulation.

Order parameter for free energy calculations To simulate the budding process, it is necessary to find a suitable reaction coordinate that can be used to describe a reversible transformation path (see Sec. 1.2).

Our density-field-based free energy methods (see Chap. 2 and 3) could, in principle, be an elegant way to describe the transformation process. Two choices for the respective reference molecules are imaginable: a) the hydrophobic tails of the POPC molecules forming the membrane leaflets or b) the neutral lipids, since the whole process can be seen as a dewetting process. The dewetting process is linked to the dewetting angle and the corresponding shape of the neutral lipid lens [57, 58]. Alas, there are critical objections to be raised.

1) The current implementation of the string method and DFTI as used in Chap. 2 and 3 only allows for simulations at constant volume and is not suited for changes of the box vectors, which is crucial for the emergence of the droplet from the bilayer. The budding will contract the box in the membrane plane at a constant particle number. The grid used to calculate the local densities would need to be adapted to that change. A simple scaling of the grid with the box vectors is not sufficient, since it would make the comparison to the reference state or the comparison between two different states along a path impossible, causing the local chemical potential to lose its meaning. A possible solution might be to not link the construction of the density grid to the simulation box but only apply it at the "region of interest", e.g. the neutral lipid lens. Still, the implementation needs careful consideration regarding the accounting for box deformations and comparability of grid points.

2) Test simulations for a system size of $\sim 30\,\mathrm{k}$ particles (modelling vesicle fusion) showed a performance (80 ns/day), rendering a sufficient sampling for DFTI as well as the string method unfeasible. Parallelizing the calculation of the forces acting on particles due to the external potential, bears the potential of enormously speeding up the calculations both for the DFTI and the string method.

The Gromacs software package offers a variety of external potentials that can be combined and applied to restrain or pull/steer a system. The biasing potentials are applied to reference groups specified as input parameters. A particle or a group can be pulled with respect to a reference coordinate or another group of atoms. The distance between the reference groups describes the current state of the process, i.e. it represents the reaction coordinate. Several pulling schemes (Fig. 4.4) were considered in order to resolve the dilemma described above but none were found to do the trick.

In terms of the budding process this could be applied by pulling the center of mass of the neutral lipid lens away from its equilibrium position (Fig. 4.4A) or by pulling the lipid lens with respect to the lower bilayer. In the former scheme, the bilayer will be pulled together with the droplet without triggering the dewetting from the bilayer. In the latter scheme, the lower monolayer would remain in its position while the lens is pulled away.

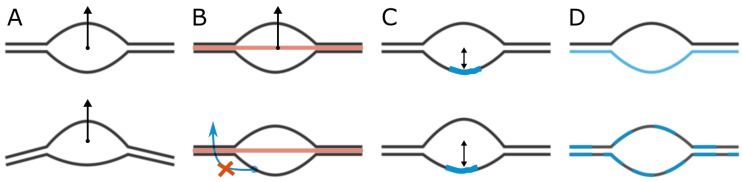

Figure 4.4: Pulling coordinates for the budding of a neutral lipid lens from a lipid bilayer with a pore for material exchange. A) direct pulling of the center of mass (COM) of the TAG lens, B) applying a flat bottom potential to the lower monolayer (lipids cannot pass beyond this threshold) C) pulling the COM of TAG with respect to a cylindrical cutout of the lower monolayer, D) diffusion of lipids from the lower monolayer to the upper monolayer corrupts unambiguous determination of COM of the reference group.

A flat bottom potential can be used to ensure that the bilayer (Fig. 4.4B) does not follow the motion of the droplet. Applying this potential to one of the monolayers will a) hinder normal undulation of the membrane and b) not allow lipids of the lower leaflet to move to the upper leaflet. Thus, the transformation is inhibited by design. Using a cylindrical patch of the lower monolayer (Fig. 4.4C) as a reference for the pulling of the neutral lipids seemed the most promising, but test simulations did not yield the transformation results sought. Yet another obstacle using lipids of the lower bilayer as reference group is the (desired) migration to the upper layer (Fig. 4.4D). Since reference groups are provided as particle labels at the beginning of the simulation and not dynamically adapted, this might lead to artifacts in the calculation of the reference positions/distances.

Additionally, an *alchemical* approach was tested using the Gromacs built-in alchemical transformations. By gradually reducing interactions between particles (Coulomb and LJ), particles can be annihilated from the simulation system. This is commonly used for the calculation of binding affinities or solvation free energies [78, 79]. We applied this scheme to a small POPC membrane patch, where we morphed 30% of the POPC molecules of one membrane layer. Though the principle does work, the simulation performance of the Gromacs 2020.4 implementation rendered this method far beyond reasonable usage of computing time. Especially, since it is to be expected, that a considerable number of sampling replicas would be necessary to ensure sufficient overlap of all windows along the transformation path.

Seipin and TAG blisters To investigate the behaviour of the coarse-grained seipin model described in 4.3, unbiased simulations of the protein in a POPC

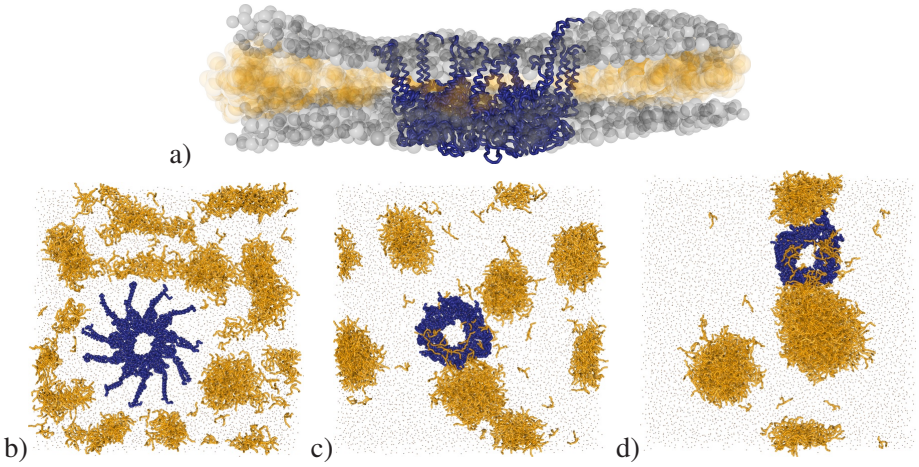

Figure 4.5: Seipin (MARTINI Model) in a POPC membrane with 11.4 mol% TAG. a: Side view of seipin in the POPC membrane with TAG blisters after 15.7 µs. b-d: Snapshots at t=0,1,15.7 µs. Gray dots indicate POPC headgroups. TAG molecules are colored orange.

membrane containing 13 mol% of TAG between the bilayer leaflets were performed. The radius of gyration of seipin is lowered over the course of the first 2 microseconds of the simulation (see Fig. 4.6a), indicating a contraction of the structure. Seipin as modelled from Cryo-EM structure RCSB-PDB 6DS5 [66] orients its transmembrane helices perpendicular to the membrane plane reducing the radius of the formed ring to about 6.2 nm. An initially random distribution of TAG molecules in the membrane quickly assembled into larger clusters of about 100 molecules. After a 15.7 µs simulation, the smaller blisters had combined into three clusters (compare Fig. 4.5). Once a cluster associated with the ring formed by the seipin transmembrane domains, it stayed in contact. This agrees with the observation by Zoni et al. [80] that diffusion of TAGs in the vicinity of seipin TM helices is slowed down. Fig. 4.6b depicts the count of TAG molecules found within a cylinder of radius r=6.4 nm or r=3.2 nm from the center of the seipin ring (~center of geometry of the protein).

After about 7 µs, the numbers seem to stabilize to 50.0±4.6 and 11.6±2.1 for the smaller radius (mean calculated for the last 17.64 µs). Interestingly, the TAG assemblies do not cluster in the center of the seipin ring as was very recently predicted by comparable molecular dynamics simulations by Prasanna et al. [81]. In their data, seipin collects randomly dispersed TAG molecules at an initial concentration of 2.5 mol% over the course of a 30 µs simulation. They also showed that a serine (Ser166) located in the inner ring of the seipin oligomer

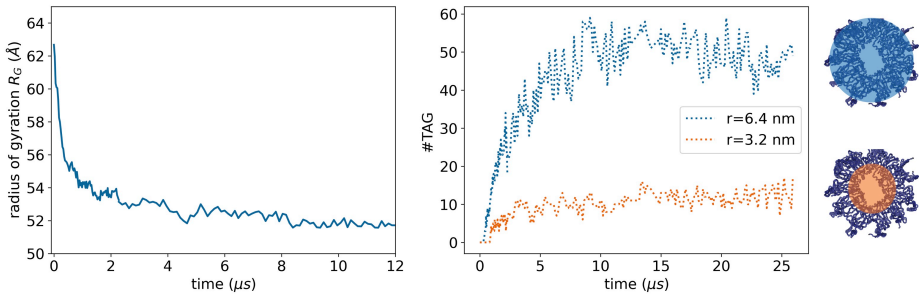

Figure 4.6: Seipin in POPC membrane with TAG. *left*: Radius of Gyration of seipin representing the alignement of the transmembrane domains in the bilayer. *right*: Number of TAG molecules associated with seipin within a cylinder of radius of 6.4 and 3.2 nm from the center of geometry of the protein.

seems to have increased affinity towards the TAG molecules. The fact that the number of TAG molecules in a small radius from the seipin center does not steadily increase (see Fig. 4.6b), indicating that there is no flux from the clusters at the outer rim of the molecule, seems to contradict these findings. The different observations might be due to the initial cluster formation of the TAG molecules. Prasanna et al. [81] used a low concentration leading to comparatively slow assembly, whereas the simulations presented here start with TAG assemblies already present and growing quickly due to high membrane TAG concentration. Furthermore, a difference in the seipin model could cause different function of the protein. The N- and C-terminal transmembrane domains of the same protomer of the seipin model used in this work are in close contact, whereas it appears that they are arranged equidistantly around the undecamer in the work of Prasanna et al. [81]. A possible influence should be addressed in additional simulations. Salo et al. [64] found that LDs with seipin associated will grow at the expense of droplets that have been depleted of seipin. Prasanna et al. [81] further postulated that seipin could be important to facilitate clustering of TAGs at starving conditions, i.e. low TAG concentration.

A shift in seipins function due to concentration changes could explain the different observations. While facilitating growth at low concentrations, seipin may control the ripening of droplets at high concentrations by linking TAG clusters. The helix ring could serve as a kind of obstacle ensuring a steady growth while preventing quick coalescence.

4.4 Summary and Outlook

Lipid droplets are a good example of the complexity of membrane biology. There are many facets to this system that need to be considered, e.g. the composition and curvature of the endoplasmic reticulum [82], the proteins found to influence LD biogenesis [77] or the physics of fluid materials like lipids itself [42]. In order to investigate the mechanisms at play, models need to be designed to separate the various aspects of a process. Decreasing the complexity helps to spot the relevant mechanisms. Though *in silico* modelling via molecular dynamics simulations is vastly limited by the computational resources and routines available, it has become an important tool to support experimental findings or to deliver new ideas for experiment design. Finding a suitable reaction coordinate to describe the budding process as a part of the lipid droplet biogenesis, proved to be difficult due to this limitation.

In order to calculate the free energy associated with a constructed path between a droplet lens and a budded droplet a sequence of structures is produced which are then sampled individually. Even though the DFTI, as well as the alchemical approach described in Sec. 4.3 could in principle be used to achieve the transformation, they can be rendered unfeasible due to simulation cost at the current state of their implementations. Using the restraining potentials provided by Gromacs seems the most promising option. Although a thorough scaling to minimize cost and testing to rule out artifacts due to poorly chosen reference groups should be considered. Unfortunately, the execution of these simulations or the implementation improvement is beyond the limit of this thesis.

The role of seipin and its companions, such as PEX30 or FIT2 [77], is still not fully understood and there are interesting aspects left to be investigated. Molecular dynamics simulations will presumably gain increasing importance in the process of elucidating protein function. Aspects of the coarse-grained seipin model could be refined to ensure that the protein function is not biased. The location of transmembrane helices, for instance, could potentially influence the interaction with the neutral lipids. It may be beneficial to employ atomistic simulations to refine the structure. Also, inter-helix interactions should be investigated to determine the alignment of the transmembrane helices and the potential shift in functionality of the seipin oligomer.

Chapter 5

Summary, Conclusion and Outlook

Membranes and their constituting lipids are an integral component of life. We are only at the beginning of understanding the complex interplay of all components. Molecular simulations can bridge a gap not covered by experimental techniques: providing a comprehensive insight into processes happening on a molecular level. With the technical advances in the last decades, the popularity of simulations as a tool to support or even predict experimental results has vastly increased, and with it the need for easily accessible methods. The coarse-grained MARTINI model [30] is one example of this trend. With its relatively simple near-atomistic building block approach, it has a comparatively low access barrier and allows for quick adaptation and extension for a variety of problems.

The density field thermodynamic integration method (DFTI, Chap. 2) that was implemented and tested in this thesis lives in that same spirit: to provide an accessible and versatile tool to estimate free-energy differences between two metastable lipid morphologies.

The combination of a thermodynamic integration (TI) scheme with a density-based biasing potential paves the way for an application to a diverse set of problems. The same holds true for the string method adaptation used in this work, which was first used in this combination by Smirnova et al. [18] to calculate the minimum free energy path (MFEP) for stalk formation between two apposing membranes and the influence of the presence of SNARE transmembrane domains. Both methods were tested on three example systems: the breaking of a worm-like micelle (Sec. 2.3.2) and a toroidal micelle (see Sec. 3.B) and the formation of a stalk (Sec. 2.3.1). In all cases DFTI and string method yielded comparable results.

The density as an order parameter is not only suitable for describing the reaction coordinate for topological transformations involving lipids, but could also potentially be used on any component in a system to describe morphologies without restricting motion of individual particles. With the possibility to tune the grid size, i.e. the resolution of the density description, it is possible to even describe delicate configurations, e.g. with regions composed of only one

molecule, as seen in the examples.

The main advantage of the DFTI is that it is comparatively quick. While the MFEP needs many (hundreds) iterations for convergence, the DFTI, in principle, only needs one run. The (basic) implementation as well as the analysis are fairly straight forward and less prone for implementation errors, since additional steps, such as the reparametrization of the path in the string method, are not needed. Yet there are weak points that could be addressed in future work.

1) The integration of the full thermodynamic cycle which would, in principle, also account for fluctuations of the starting structures, fails if the system picks up excessive translational degrees of freedom, thus resulting in a large entropic contribution, when switching off the external restraining field. In the discussed examples it can be seen that this is less pronounced in the case of the stalk formation compared to the worm-like micelle simply due to the nature of the structure and their ability to translate in the simulation box. A trajectory post-processing routine, where a fitting of the closest image to the reference field is performed, could be implemented to account for the translation.

Furthermore, the alternative path described in Sec. 2.3.3 is a simple approach to alleviate this shortcoming. In this scheme a quenching of the fluctuations, similar to the string, using the gradient of the local chemical potential, is performed prior to the TI of transformation between the local minima. Since this quenching is only performed on a single structure and does not require communication between several states, it will only require comparatively few iterations to obtain the quenched reference states. This procedure can be used to provide a quick estimate of the free energy difference for cases where the information about the minimum free energy path is not needed or to generate input references for, e.g., MFEP calculations.

2) Density as order parameter is very versatile and especially suitable to describe membrane shapes. However, as described in Sec. 4.3, the implementation, as used for this work, is not yet feasible for large systems due to simulation cost. Code optimizations and parallelization could help to unfold the full potential of DFTI as well as the string method. First steps towards the realization of this coding project were done but the implementation has yet to be executed. One possible approach here could be the usage of the Gromacs API that is available since the Gromacs 2019 release [83].

3) The current limitation to simulations in the *NVT* ensemble would require an additional free energy correction for systems undergoing transformations that are not only limited to a small region such as the breaking of the WM, but do require restructuring of the majority of the system. The budding process of a lipid droplet, as described in 4.3, is an example for which this description does not suffice. The

structural transformation of the droplet happens on a much larger scale. During the transformation from a budded droplet towards a lens the membrane would grow in the xy-plane. The grid used to calculate the local densities would need to be adapted to that change. On-the-fly adjustment of the grid is a non-trivial task. A simple scaling of the grid with the box vectors is not sufficient since the local chemical potential is only meaningful if locality itself is well defined. Furthermore, systematically studying the influence of the force constant and step size of the minimization on convergence for the DFTI minimization scheme and the string method bears the potential of optimizing the process even more.

The work reported in Chapter 3 is located at the verge of biomaterials science. The structural features of lipids are similar to block copolymers but on a smaller length scale. Intrigued by the observation of toroidal micelles formed from single-chain bola amphiphiles (PC-32-PC) in simulations, we explored the phase behaviour of these special lipids. Ring shaped aggregates are well known from block copolymers [84]. Since bola lipids possess a similar structure, i.e. two polar headgroups linked by an apolar carbon chain, we hypothesized that toroidal micelles could indeed be accessible under certain conditions. Calculation of the minimum free energy path (MFEP) via the string method for the opening of a toroidal micelle provided valuable insights to predict the stability of such a phase. We proposed a pathway of tricking the system into forming rings by heat-shocking disc shaped micelles formed below T_m. This alludes to the opportunity to use these aggregates as thermo-responsive carrier systems, for instance, in drug or gene delivery [85, 86].

Lipid droplets (LDs) are another interesting case, where free-energy calculations could enlighten the ongoing discourse about the mechanism of their emergence. Specifically, the influence of seipin on that process is debated. Comparative studies with and without the protein should help to clarify whether it could serve as structural stabilizer of the membrane/TAG lens contact or whether its role is rather a nucleation site for TAG molecules or blisters. Chapter 4 reflects the current stage of this process. Unfortunately our free-energy techniques are not (yet) suitable for this system. Also, finding another reaction coordinate proved to be difficult, rendering the planned free-energy calculations beyond the time limit of this thesis. The preliminary results already suggest that, in the built model, the budded LD state is not a meta-stable configuration but it can be used and adapted to further investigate factors, such as lipid composition or the interaction with proteins. Due to early stages of the droplet formation being elusive to experimental detection, there are only theoretical considerations like the calculations of Chorlay et al. [57] setting the lower threshold of LD budding at $\geq$20 nm. Thus, a possible size effect is not to be neglected and for future calculations, different droplet sizes should be compared. Simulations of

the built seipin model reinforce the experimentally observed association with premature TAG assemblies [50]. Further investigations concerning the seipin model should be prompted to explain the different observations in the work of Prasanna et al. [81]. The rapid development of new tools for membrane analysis is also an important factor in the process of studying complex membrane systems. Bhatia et al., for instance, recently published MemSurfer [87], which is capable of accurately calculating topological properties of membranes, even for highly curved surfaces (e.g. budded LDs).

To summarize, this work explored the usage of density field based free energy methods in its predictive power and limitations.

The more we learn the more we realize the unimaginable complexity of our physical world, including the biochemistry and biophysics of living organisms. The importance of computer simulations and numerical methods will further increase as a toolkit for analysis and predictions complementary to experimental techniques. The development of reliable and flexible free energy methods will be key for the integration into larger workflows to be efficiently used in, e.g. the development of lipidic carrier systems for drugs or the investigation of peptide membrane interactions. To advance from single show cases and establish these methods, implementations should be accessible. The density-field-based string method and the DFTI would be good additions to the Gromacs free energy kernel. With the adaptions suggested above, they could be useful to answer many questions regarding the stability of soft matter morphologies investigated using molecular dynamics.

Bibliography

[1] Goodsell, D. S. *Lipid Droplets*. RCSB Protein Data Bank. doi: 10.2210/rcsb_pdb/goodsell–gallery–017. 2019.

[2] Goodsell, D. S. *The machinery of life*. Springer Science & Business Media, 2009.

[3] Deamer, D. "The role of lipid membranes in life's origin". In: *Life* vol. 7, no. 1 (2017), p. 5.

[4] Mouritsen, O. G. and Bagatolli, L. A. *Life-as a matter of fat: lipids in a membrane biophysics perspective*. Springer, 2015.

[5] Ramadurai, S. et al. "Lateral diffusion of membrane proteins". In: *Journal of the American Chemical Society* vol. 131, no. 35 (2009), pp. 12650–12656.

[6] Mühlenbrock, P., Sari, M., and Steinem, C. "In vitro single vesicle fusion assays based on pore-spanning membranes: merits and drawbacks". In: *European Biophysics Journal* (2020), pp. 1–14.

[7] Martyna, A. et al. "Curvature sensing by a viral scission protein". In: *Biochemistry* vol. 55, no. 25 (2016), pp. 3493–3496.

[8] Janshoff, A. and Steinem, C. "Mechanics of lipid bilayers: What do we learn from pore-spanning membranes?" In: *Biochimica et Biophysica Acta (BBA)-Molecular Cell Research* vol. 1853, no. 11 (2015), pp. 2977–2983.

[9] Srivastava, A. P. et al. "High-resolution cryo-EM analysis of the yeast ATP synthase in a lipid membrane". In: *Science* vol. 360, no. 6389 (2018).

[10] Mühlenbrock, P. et al. "Fusion pore formation observed during SNARE-mediated vesicle fusion with pore-spanning membranes". In: *Biophysical Journal* vol. 119, no. 1 (2020), pp. 151–161.

[11] Nakane, T. et al. "Single-particle cryo-EM at atomic resolution". In: *Nature* vol. 587, no. 7832 (2020), pp. 152–156.

[12] Helfrich, W. "Elastic Properties of Lipid Bilayers: Theory and Possible Experiments". In: *Zeitschrift für Naturforschung C* vol. 28, no. 11-12 (Dec. 1973), pp. 693–703.

[13] Marrink, S. J. et al. “Computational and Experimental Advances in Biomembranes: Resolving Their Complexity”. In: *J. Phys. Chem. B* vol. 124, no. 45 (2020), pp. 9975–9976.

[14] Chipot, C. “Frontiers in free-energy calculations of biological systems”. In: *Wiley Interdisciplinary Reviews: Computational Molecular Science* vol. 4, no. 1 (2014), pp. 71–89.

[15] Chipot, C. and Pohorille, A. “Free energy calculations”. In: *Springer series in chemical physics* vol. 86 (2007), pp. 159–184.

[16] Bubnis, G., Risselada, H., and Grubmueller, H. “Free Energy Landscapes of Vesicle Fusion by Umbrella Sampling MD Simulations”. In: *Biophys. J.* Vol. 104, no. 2 (2013), 92a.

[17] Müller, M. et al. “Transition Path from Two Apposed Membranes to a Stalk Obtained by a Combination of Particle Simulations and String Method”. In: *Phys. Rev. Lett.* Vol. 108 (22 May 2012), p. 228103.

[18] Smirnova, Y. G., Risselada, H. J., and Müller, M. “Thermodynamically reversible paths of the first fusion intermediate reveal an important role for membrane anchors of fusion proteins”. In: *Proceedings of the National Academy of Sciences* vol. 116, no. 7 (2019), pp. 2571–2576.

[19] Smirnova, Y. G. et al. “Free-energy calculation methods for collective phenomena in membranes”. In: *J. Phys. D: Appl. Phys.* Vol. 48, no. 34 (2015), p. 343001.

[20] Weinan, E, Ren, W., and Vanden-Eijnden, E. “Simplified and improved string method for computing the minimum energy paths in barrier-crossing events”. In: *J. Chem. Phys.* Vol. 126, no. 16 (2007), p. 164103.

[21] Frenkel, D. and Smit, B. *Understanding molecular simulation: from algorithms to applications*. Vol. 1. Elsevier, 2001.

[22] Berendsen, H. *Simulating the physical world*. Cambridge University Press Cambridge, 2007.

[23] Hockney, R. W., Goel, S., and Eastwood, J. “Quiet high-resolution computer models of a plasma”. In: *Journal of Computational Physics* vol. 14, no. 2 (1974), pp. 148–158.

[24] Berendsen, H. J., Spoel, D. van der, and Drunen, R. van. “GROMACS: a message-passing parallel molecular dynamics implementation”. In: *Computer physics communications* vol. 91, no. 1-3 (1995), pp. 43–56.

[25] Bekker, H et al. “Gromacs: A parallel computer for molecular dynamics simulations”. In: *Physics computing*. Vol. 92. World Scientific Singapore. 1993, pp. 252–256.

[26] Abraham, M. J. et al. “GROMACS: High performance molecular simulations through multi-level parallelism from laptops to supercomputers”. In: *SoftwareX* vol. 1 (2015), pp. 19–25.

[27] Winger, M. et al. “On using a too large integration time step in molecular dynamics simulations of coarse-grained molecular models”. In: *Physical Chemistry Chemical Physics* vol. 11, no. 12 (2009), pp. 1934–1941.

[28] Lennard-Jones, J. E. “On the forces between atoms and ions”. In: *Proceedings of the Royal Society of London. Series A, Containing Papers of a Mathematical and Physical Character* vol. 109, no. 752 (1925), pp. 584–597.

[29] Kmiecik, S. et al. “Coarse-grained protein models and their applications”. In: *Chemical reviews* vol. 116, no. 14 (2016), pp. 7898–7936.

[30] Marrink, S. J. et al. “The MARTINI Force Field: Coarse Grained Model for Biomolecular Simulations”. In: *J. Phys. Chem. B* vol. 111, no. 27 (July 2007), pp. 7812–7824.

[31] Arnarez, C, Marrink, S., and Periole, X. “Identification of cardiolipin binding sites on cytochrome c oxidase at the entrance of proton channels”. In: *Scientific reports* vol. 3, no. 1 (2013), pp. 1–9.

[32] Shirts, M. R. and Mobley, D. L. “An introduction to best practices in free energy calculations”. In: *Biomolecular Simulations*. Springer, 2013, pp. 271–311.

[33] Wu, D. and Kofke, D. A. “Phase-space overlap measures. II. Design and implementation of staging methods for free-energy calculations”. In: *The Journal of chemical physics* vol. 123, no. 8 (2005), p. 084109.

[34] Wu, D. and Kofke, D. A. “Phase-space overlap measures. I. Fail-safe bias detection in free energies calculated by molecular simulation”. In: *The Journal of chemical physics* vol. 123, no. 5 (2005), p. 054103.

[35] Shirts, M. R., Mobley, D. L., and Chodera, J. D. “Chapter 4 Alchemical Free Energy Calculations: Ready for Prime Time?” In: ed. by Spellmeyer, D. and Wheeler, R. Vol. 3. Annual Reports in Computational Chemistry. Elsevier, 2007, pp. 41 –59.

[36] Darve, E. “Thermodynamic Integration Using Constrained and Unconstrained Dynamics”. In: *Free Energy Calculations: Theory and Applications in Chemistry and Biology*. Ed. by Chipot, C. and Pohorille, A. Berlin, Heidelberg: Springer Berlin Heidelberg, 2007, pp. 119–170.

[37] Kukol, A. *Molecular modeling of proteins*. Vol. 443. Springer, 2008.

[38] Gao, Q. and Goodman, J. “The lipid droplet—a well-connected organelle”. In: *Frontiers in Cell and Developmental Biology* vol. 3 (2015), p. 49.

[39] Farese Jr, R. V. and Walther, T. C. “Lipid droplets finally get a little RESPECT”. In: *Cell* vol. 139, no. 5 (2009), pp. 855–860.

[40] Thiam, A. R. et al. “The biophysics and cell biology of lipid droplets”. In: *Nature reviews Molecular cell biology* vol. 14, no. 12 (2013), p. 775.

[41] Walther, T. C., Chung, J., and Farese Jr, R. V. “Lipid droplet biogenesis”. In: *Annual review of cell and developmental biology* vol. 33 (2017), pp. 491–510.

[42] Zoni, V. et al. “Lipid droplet biogenesis is driven by liquid-liquid phase separation”. In: *DEVELOPMENTAL-CELL-D-20-00075* (2020).

[43] Khandelia, H. et al. “Triglyceride blisters in lipid bilayers: implications for lipid droplet biogenesis and the mobile lipid signal in cancer cell membranes”. In: *PloS one* vol. 5, no. 9 (2010), e12811.

[44] Suzuki, M. et al. “Lipid droplets: size matters”. In: *Journal of electron microscopy* vol. 60, no. suppl_1 (2011), S101–S116.

[45] Kassan, A. et al. “Acyl-CoA synthetase 3 promotes lipid droplet biogenesis in ER microdomains”. In: *Journal of Cell Biology* vol. 203, no. 6 (2013), pp. 985–1001.

[46] Nettebrock, N. T. and Bohnert, M. “Born this way–biogenesis of lipid droplets from specialized ER subdomains”. In: *Biochimica et Biophysica Acta (BBA)-Molecular and Cell Biology of Lipids* vol. 1865, no. 1 (2020), p. 158448.

[47] Wang, H. et al. “Seipin is required for converting nascent to mature lipid droplets”. In: *elife* vol. 5 (2016), e16582.

[48] Choudhary, V. et al. “A conserved family of proteins facilitates nascent lipid droplet budding from the ER”. In: *Journal of Cell Biology* vol. 211, no. 2 (2015), pp. 261–271.

[49] Schuldiner, M. and Bohnert, M. “A different kind of love–lipid droplet contact sites”. In: *Biochimica et Biophysica Acta (BBA)-Molecular and Cell Biology of Lipids* vol. 1862, no. 10 (2017), pp. 1188–1196.

[50] Salo, V. T. and Ikonen, E. “Moving out but keeping in touch: contacts between endoplasmic reticulum and lipid droplets”. In: *Current opinion in cell biology* vol. 57 (2019), pp. 64–70.

[51] Chorlay, A. et al. “Membrane asymmetry imposes directionality on lipid droplet emergence from the ER”. In: *Developmental cell* vol. 50, no. 1 (2019), pp. 25–42.

[52] M'barek, K. B. et al. "ER membrane phospholipids and surface tension control cellular lipid droplet formation". In: *Developmental cell* vol. 41, no. 6 (2017), pp. 591–604.

[53] Zoni, V. et al. "To Bud or Not to Bud: A Perspective on Molecular Simulations of Lipid Droplet Budding". In: *Frontiers in molecular biosciences* vol. 6 (2019), p. 124.

[54] Choudhary, V. et al. "Architecture of lipid droplets in endoplasmic reticulum is determined by phospholipid intrinsic curvature". In: *Current Biology* vol. 28, no. 6 (2018), pp. 915–926.

[55] Gao, M. et al. "The biogenesis of lipid droplets: lipids take center stage". In: *Progress in lipid research* vol. 75 (2019), p. 100989.

[56] Thiam, A. R. and Forêt, L. "The physics of lipid droplet nucleation, growth and budding". In: *Biochimica et Biophysica Acta (BBA)-Molecular and Cell Biology of Lipids* vol. 1861, no. 8 (2016), pp. 715–722.

[57] Chorlay, A. and Thiam, A. R. "An asymmetry in monolayer tension regulates lipid droplet budding direction". In: *Biophysical journal* vol. 114, no. 3 (2018), pp. 631–640.

[58] Deslandes, F., Thiam, A. R., and Forêt, L. "Lipid droplets can spontaneously bud off from a symmetric bilayer". In: *Biophysical journal* vol. 113, no. 1 (2017), pp. 15–18.

[59] Upadhyaya, A. and Sheetz, M. P. "Tension in tubulovesicular networks of Golgi and endoplasmic reticulum membranes". In: *Biophysical journal* vol. 86, no. 5 (2004), pp. 2923–2928.

[60] Ito, D. and Suzuki, N. "Seipinopathy: a novel endoplasmic reticulum stress-associated disease". In: *Brain* vol. 132, no. 1 (2009), pp. 8–15.

[61] Guillén-Navarro, E. et al. "A new seipin-associated neurodegenerative syndrome". In: *Journal of medical genetics* vol. 50, no. 6 (2013), pp. 401–409.

[62] Magré, J. et al. "Identification of the gene altered in Berardinelli–Seip congenital lipodystrophy on chromosome 11q13". In: *Nature genetics* vol. 28, no. 4 (2001), pp. 365–370.

[63] Henne, W. M., Reese, M. L., and Goodman, J. M. "The assembly of lipid droplets and their roles in challenged cells". In: *The EMBO journal* vol. 37, no. 12 (2018), e98947.

[64] Salo, V. T. et al. "Seipin facilitates triglyceride flow to lipid droplet and counteracts droplet ripening via endoplasmic reticulum contact". In: *Developmental cell* vol. 50, no. 4 (2019), pp. 478–493.

[65] Salo, V. T. et al. “Seipin regulates ER–lipid droplet contacts and cargo delivery”. In: *The EMBO journal* vol. 35, no. 24 (2016), pp. 2699–2716.

[66] Yan, R. et al. “Human SEIPIN binds anionic phospholipids”. In: *Developmental cell* vol. 47, no. 2 (2018), pp. 248–256.

[67] Sui, X. et al. “Cryo–electron microscopy structure of the lipid droplet–formation protein seipin”. In: *Journal of Cell Biology* vol. 217, no. 12 (2018), pp. 4080–4091.

[68] Michaud-Agrawal, N. et al. “MDAnalysis: a toolkit for the analysis of molecular dynamics simulations”. In: *Journal of computational chemistry* vol. 32, no. 10 (2011), pp. 2319–2327.

[69] Marrink, S. J., Risselada, J., and Mark, A. E. “Simulation of gel phase formation and melting in lipid bilayers using a coarse grained model”. In: *Chem. Phys. Lipids* vol. 135, no. 2 (June 2005), pp. 223–244.

[70] Wassenaar, T. A. et al. “Computational lipidomics with insane: a versatile tool for generating custom membranes for molecular simulations”. In: *Journal of chemical theory and computation* vol. 11, no. 5 (2015), pp. 2144–2155.

[71] Jong, D. H. de et al. “Improved parameters for the martini coarse-grained protein force field”. In: *Journal of chemical theory and computation* vol. 9, no. 1 (2013), pp. 687–697.

[72] Vuorela, T. et al. “Role of lipids in spheroidal high density lipoproteins”. In: *PLoS Comput Biol* vol. 6, no. 10 (2010), e1000964.

[73] Parrinello, M. and Rahman, A. “Polymorphic transitions in single crystals: A new molecular dynamics method”. In: *Journal of Applied physics* vol. 52, no. 12 (1981), pp. 7182–7190.

[74] Bussi, G., Donadio, D., and Parrinello, M. “Canonical sampling through velocity rescaling”. In: *J. Chem. Phys.* Vol. 126, no. 1 (2007), p. 014101.

[75] Wee, K. et al. “Towards a mechanistic understanding of lipodystrophy and seipin functions”. In: *Bioscience reports* vol. 34, no. 5 (2014).

[76] Bennett, W. D. and Tieleman, D. P. “Water defect and pore formation in atomistic and coarse-grained lipid membranes: pushing the limits of coarse graining”. In: *Journal of chemical theory and computation* vol. 7, no. 9 (2011), pp. 2981–2988.

[77] Bohnert, M. “New friends for seipin—Implications of seipin partner proteins in the life cycle of lipid droplets”. In: *Seminars in cell & developmental biology*. Elsevier. 2020.

[78] Abel, R. et al. “Advancing drug discovery through enhanced free energy calculations”. In: *Accounts of chemical research* vol. 50, no. 7 (2017), pp. 1625–1632.

[79] Cournia, Z., Allen, B., and Sherman, W. “Relative binding free energy calculations in drug discovery: recent advances and practical considerations”. In: *Journal of chemical information and modeling* vol. 57, no. 12 (2017), pp. 2911–2937.

[80] Zoni, V. et al. “Lipid Droplet Biogenesis Is a Liquid Phase Separation Spatially Regulated by Seipin and Membrane Curvature.” bioRxiv: 777466”. In: (2019).

[81] Prasanna, X. et al. “Seipin traps triacylglycerols to facilitate their nanoscale clustering in the endoplasmic reticulum membrane”. In: *PLoS biology* vol. 19, no. 1 (2021), e3000998.

[82] Santinho, A. et al. “Membrane curvature catalyzes lipid droplet assembly”. In: *Current Biology* vol. 30, no. 13 (2020), pp. 2481–2494.

[83] Irrgang, M. E., Hays, J. M., and Kasson, P. M. “gmxapi: a high-level interface for advanced control and extension of molecular dynamics simulations”. In: *Bioinformatics* vol. 34, no. 22 (2018), pp. 3945–3947.

[84] Cui, H. et al. “Origins of toroidal micelle formation through charged triblock copolymer self-assembly”. In: *Soft Matter* vol. 5, no. 6 (2009), pp. 1269–1278.

[85] Fong, W.-K. et al. “Responsive self-assembled nanostructured lipid systems for drug delivery and diagnostics”. In: *J. Colloid Interface Sci.* Vol. 484 (Dec. 2016), pp. 320–339.

[86] Fariya, M. et al. “Bolaamphiphiles: A Pharmaceutical Review”. eng. In: *Adv. Pharm. Bull.; eISSN 2251-7308* (2014).

[87] Bhatia, H. et al. “MemSurfer: a tool for robust computation and characterization of curved membranes”. In: *Journal of chemical theory and computation* vol. 15, no. 11 (2019), pp. 6411–6421.

Acknowledgement

When I decided to ask for an internship with my supervisor Jelger Risselada after hearing about MD for the first time in his lecture during my master studies, I would have never envisioned to move to Göttingen and pursue a PhD in this field. Jelger, thank you with all of my heart for this opportunity. I appreciate that you have always given me a lot of freedom to grow on the challenges I encountered in the past years but also found kind words to encourage me whenever I struggled. I wish you and Yuliya all the best for your future in Dortmund and hope you find an inspiring environment for your research.

With deep respect, I want to thank Marcus Müller for welcoming us into this group, all the fruitful discussions and helpful comments. Further, I am very grateful to Yuliya Smirnova, Veronica Chappa, Luca Monticelli, Salvatore Manmana and my thesis committee, Claudia Steinem and Stefan Klumpp, for their scientific guidance and patience.

Many thanks to Katrin Glormann, Gabriele Schubert, Frauke Bergmann, Antje Erdmann and Tabea Oswald for all the support in handling bureaucratic hurdles and Jürgen Holm for the immediate help with any IT-related question.

To Jan Stolpp, Juan Orozco Rey, Ludwig Schneider, Colin Koch, Florian Sohn, Nils Abeling, Constantin Meyer, Michael ten Brink, Simon Luca Villani and Kristof Harms for all the hours we spent with hilarious, crazy and/or philosophical discussions. They definitely had a big impact on me.

Special thanks to Juhaina Bandak, Markus Träupmann and Kai Stroh for proofreading. Kai, without our almost daily online sessions, the last year would have been unbearable. Your presence and support meant a great deal to me. Please do not hesitate to contact me, if you ever need backing while completing your work or if you simply need someone to listen. I would be happy to return the favour.

Finally, I want to express my gratitude to my family and Susann Winsel for making me who I am, supporting me all these years and believing in me.

♥